Novel integrated computational approach for designing Fe-Ni-based alloys

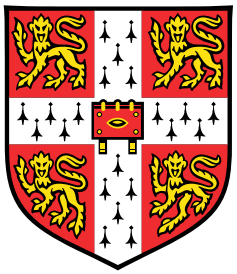

Masayoshi Sawada

Department of Materials Science and Metallurgy
University of Cambridge

This dissertation is submitted for the degree of
Doctor of Philosophy

Churchill College October 2018

Declaration

This dissertation is the result of my own work and includes nothing which is the outcome of work done in collaboration except as declared in the Preface and specified in the text. It is not substantially the same as any that I have submitted, or, is being concurrently submitted for a degree or diploma or other qualification at the University of Cambridge or any other University or similar institution except as declared in the Preface and specified in the text. I further state that no substantial part of my dissertation has already been submitted, or, is being concurrently submitted for any such degree, diploma or other qualification at the University of Cambridge or any other University or similar institution except as declared in the Preface and specified in the text. It does not exceed the prescribed word limit for the relevant Degree Committee.

Masayoshi Sawada
October 2018

Abstract

Title: Novel integrated computational approach for designing Fe-Ni-based alloys

A novel computational approach for designing high temperature alloys is proposed; the approach incorporates properties prediction and optimisation. As for properties prediction, microstructural parameters, such as the volume fraction and precipitate size after heat treatment (replicating the service conditions of automobile sealing parts) were thermokinetically calculated by adopting phase transformation software. The associated yield stress was then predicted using classical strengthening theories: solid solution, grain boundary and precipitation strengthenings. These calculations were integrated with a genetic algorithm (GA) for searching the optimal chemical compositions considering not only the strength after a long time heat treatment but also cost and producibility constraints. The calculation parameters for the GA, such as population size and mutation ratio, were also considered.

The alloy designed by the computer-aided approach described above was produced and validated. The designed alloy (Fe-opt) whose composition is Fe-33Ni-15.5Cr-1.6Al-0.3Nb-2.8Ti-3.7W-0.9Co-0.01C are proved to have the high strength after a long time high temperature exposure due to finely dispersed precipitates, γ', although the strength is not as high as expected from the calculation. The microstructure analysis suggests that W in the designed alloy has a negative influence on the mechanical properties of the alloy by forming coarse Laves phases on the grain boundaries. Therefore, the alloy sheet, with the same composition of Fe-opt but without W (Fe-opt2) was prepared and examined. Fe-opt2 has higher strength than Fe-opt and than more expensive Ni-based superalloys, such as Alloy 718Plus.

The integrated approach conducted in this study has successfully provided an efficient and effective alloy design methodology. This approach can be widely adopted for use in many fields beyond high-temperature alloys by adopting suitable thermokinetic databases and strengthening modelling approaches.

Masayoshi Sawada

Acknowledgements

The research described in this thesis was performed at the Department of Materials Science and Metallurgy, University of Cambridge, and Nippon Steel & Sumitomo Metal Corporation from September 2014 to August 2018. I am deeply grateful to my academic supervisor, Professor Pedro Rivera-Diaz-Del-Castillo, for accepting me as a PhD student at University of Cambridge and giving me helpful support, advice and guidance for my PhD work. I would like to express my appreciation also to my advisor, Dr Enrique Galindo Nava for his great advice. My sincere appreciation also goes to the members of Professor Rivera's group and Dr Steve Ooi for the fruitful discussion, advice and friendship. The financial support provided by Nippon Steel & Sumitomo Metal Corporation is greatly acknowledged. I gratefully appreciate Dr Manabu Takahashi and Dr Shinichi Teraoka at Nippon Steel & Sumitomo Metal Corporation too for giving me the opportunity to study at the University of Cambridge and their continuous encouragement during my PhD work. Last but not least, I would like to thank my family members, Akiko, Ikushi, Rei, Yo and Tetsuya for their great support.

Table of contents

List of figures

List of tables

List of Symbols

a	cell parameter
a_1, a_2, a_3	coefficient for APB energy assumption
a_{ia}	interatomic distance
A	area
b	magnitude of Burgers vector
c_i	concentration of element i in alloy
c_{i0}	nominal content of element i
$c_{\mathrm{ss},i}$	concentration of element i in solid solution
$c_{\gamma',i}$	concentration of element i in γ'
$c_{\mathrm{i}\alpha}$	concentration of element i in the matrix
$c_{\mathrm{i}\beta}$	concentration of element i in the precipitate
C_0	total number of atoms per unit volume
C^*	number density of atomic cluster with the radius r^*
d	diameter of precipitate
$D_{i\alpha}$	tracer diffusivity of element i in the matrix.
D_{gr}	mean grain diameter
E_{apb}	anti-phase boundary energy
$E_{\mathrm{apb},0}$	anti-phase boundary energy for pure Ni_3Al
f	size distribution of precipitates
$f_{\mathrm{mat}}, f_{\mathrm{pr}}$	fraction of the matrix, precipitates
$f_{\gamma'}, f_{\gamma''}, f_\mu, f_\sigma, f_\eta, f_\delta$	fraction of $\gamma', \gamma'', \mu, \sigma, \eta, \delta$
F	precipitate resistance force
F_{rep}	elastic repulsive force between coupled dislocations
F_{shape}	shape factor of disc-shaped precipitate
G	Gibbs free energy
G_{def}	free energy by defects in alloy per unit volume
G_{st}	misfit strain energy per unit volume

G_v	Gibbs free energy per unit volume
h	height of disc-shaped precipitate
I_cost	cost index estimated by elemental cost
j	nucleation rate with time dependence
J	nucleation rate in the entire system
J_s	steady-state nucleation rate
$J_{i\alpha}$	flux of element i into the matrix from the precipitate
$J_{i\beta}$	flux of element i into the precipitate from the matrix
k_dis	coefficient for dislocation strengthening
k_fl	coefficient for solid solution strengthening proposed by Fleischer
k_gb	coefficient for grain boundary strengthening (Hall-Petch coefficient)
k_lb	coefficient for solid solution strengthening proposed by Labusch
k_lsw	coefficient for precipitation coarsening
$k_{\mathrm{ss},i}$	coefficient for solid solution strengthening by element i
$\mathrm{k_B}$	Boltzmann constant
l	length of disc-shaped precipitate
l_i	segment length of the leading ($i = 1$) and trailing ($i = 2$) dislocations cutting the precipitate
L	square lattice spacing (mean particle distance on a plane)
L_diff	length of diffusion zone
M	Taylor factor
N_LS	total number of precipitates in the system (LS model)
p_i	price of element i
Q_in, Q_out	heat input and output
r	radius of precipitate
r_0	radius of precipitate at time $t = 0$
$\bar{r}$	mean radius of the precipitate
r^*	critical radius for precipitate nucleation
S	entropy
$\dot{S}$	entropy production during phase transformation
t	time
T	temperature
T_dis	line tension of the dislocation
T_in, T_out	entering and exhausting temperature
v	velocity of the interface front

V	volume
V_α	molar volume
V_β	volume of the precipitate
V_{ex}	the extended volume of precipitates in JMAK model
W_{out}	applied work
x_i	concentration of solute element i in γ'
Z	Zeldovich factor
β^*	the atomic attachment rate
γ_{int}	interfacial energy between a matrix and nucleus
δ_i	cell parameter change by element i
ΔG	free energy change of a system
ΔG^*	critical energy for precipitate nucleation
ΔG_{def}	free energy reduction by defects
$\Delta\varepsilon$	lattice mismatch between the matrix and precipitate
η_{eff}	thermal efficiency in the system
η_i	shear modulus change by element i
λ	distance between particles along a dislocation
λ_1	effective distance between particles
λ_s	Friedel spacing (mean particle distance on a straight dislocation)
μ	shear modulus
μ_i	shear modulus of element i
ξ	progress of overall phase transformation
ρ	dislocation density
σ_0	friction stress
σ_{dis}	dislocation strengthening
σ_{dp}	precipitation strengthening by γ''
$\sigma_{fl,i}$	solid solution strengthening based on Fleishcer's model
σ_{gb}	grain boundary strengthening
σ_{gp}	precipitation strengthening by γ'
$\sigma_{lb,i}$	solid solution strengthening based on Labusch's model
σ_{pr}	precipitation strengthening in total
σ_{ss}	solid solution strengthening
σ_{ys}	yield stress
τ_{ex}	external applied shear stress

τ_{apb}	critical resolved shear stress by anti-phase boundary effect
τ_{coh}	critical resolved shear stress by coherency effect
τ_{inc}	precipitate incubation time
τ_{oro}	critical resolved shear stress by Orowan effect
Ψ	dislocation bowing angle

Chapter 1

Introduction

1.1 Objective of the work

Environmental protection by reducing CO_2 emission has been recognised as one of the most important global issues particularly since the Kyoto protocol, which is an international agreement committing the participants to reducing greenhouse gas emissions. Although, there are many approaches to solve this problem, improving fuel efficiency in transport systems is a simple but very effective way to decrease the production of CO_2.
Based on thermodynamic theory, the thermal efficiency η_{eff} of the system is defined as

$$\eta_{\text{eff}} \equiv \frac{W_{\text{out}}}{Q_{\text{in}}} = 1 - \frac{Q_{\text{out}}}{Q_{\text{in}}} = 1 - \frac{T_{\text{out}}}{T_{\text{in}}}, \tag{1.1}$$

where η_{eff} is the thermal efficiency, W_{out} is the applied work, Q_{in} and Q_{out} are the input and waste heat and T_{in} and T_{out} are the entering and exhausting temperature, respectively [1]. This equation shows that the efficiency depends on the ratio of the entering and the exhausting temperature in the system under consideration. Here, T_{in} and T_{out} can be exemplified by the temperature at which gas burns in a combustion engine and the temperature of the environment in which the engine is located, respectively. This simple equation indicates that increasing the reaction temperature is a direct and effective way to improve energy efficiency in many types of equipment, such as combustion engines in vehicles, gas turbines and reactors in power plants.
Upon increasing the system temperature, degradation of the materials used in the system becomes a major restraint. Particularly at high operation temperatures, such as those present in boilers for power plants, cars, aeroplane engines and reactors used in heavy industries, the deterioration of the material (usually metals and alloys) is a big issue and the demand

for alloys with improved properties has escalated along with the increase in the operation temperature for such equipment.

Among the many kinds of high-temperature alloys, superalloys are of great importance because of their excellent combination of high strength and corrosion resistance at elevated temperatures, 600 °C or above [1–3]. The superalloys generally consist of Ni, Fe or Co with lower amounts of other elements, which can be exemplified by Cr, Al, Ti, W, Mo and Nb. Since the 1940s, many superalloys have been developed for various industrial applications including rockets, nuclear reactors and gas and steam turbines, whose energy efficiencies strongly depend on the material under consideration. In the last few decades, an increase in the usage of mono-crystal superalloys has taken place for turbine blades used in aeroplanes due to their high creep strength. In addition, powder metallurgy methods have enabled the production of superalloys with a high concentration of additive elements for high-quality turbine discs. Both of them have superior tensile strength, fatigue strength and creep properties at elevated temperatures. However, the demand for less costly materials should also be considered particularly in industries like a car and car-part manufacturers, where costly superalloys cannot be justified despite their excellent properties.

Some stainless steels are also recognised as high-temperature alloys due to their resistance against oxidation and high strength at elevated temperatures [4, 5]. They can be classified into several groups by their crystal structures. Among these groups, austenitic stainless steels, whose crystal structure is the same as common superalloys, show the highest strength at temperatures above 600 °C. Although the high-temperature strength of austenitic stainless steels is still inferior to that of most superalloys, stainless steels are much less expensive as the amount of costly elements, such as Ni and Co, is lower and they are produced through less costly production processes.

As stated above, materials that can be used at high temperatures are in demand by many industries, where the required properties and service temperatures depend on the application and end user. In this study, materials that can be applied to a high-temperature sealing part used in a car exhaust system are studied. Development of the sealing material that can be used at high temperatures directly leads to improve the fuel efficiency of cars and contribute to reducing greenhouse gas emissions. In Japan, for example, 20 % of CO_2 emissions stem from the transport sector, of which emissions from cars feature 90 %. Improving fuel economy in cars may also have a large impact on society with people becoming more conscious of global environmental problems. Despite their potential impact, not much attention has been paid to these materials.

The sealing parts used for an exhaust system in cars are produced from a thin alloy sheet

of about 0.2 mm in thickness. The product is manufactured by stamping or laser cutting, mechanical pressing and assembled in between two exhaust parts as shown in Figure 1.1 [6]. A convex part called "bead" in the gaskets prevents exhaust gas from leaking out from the

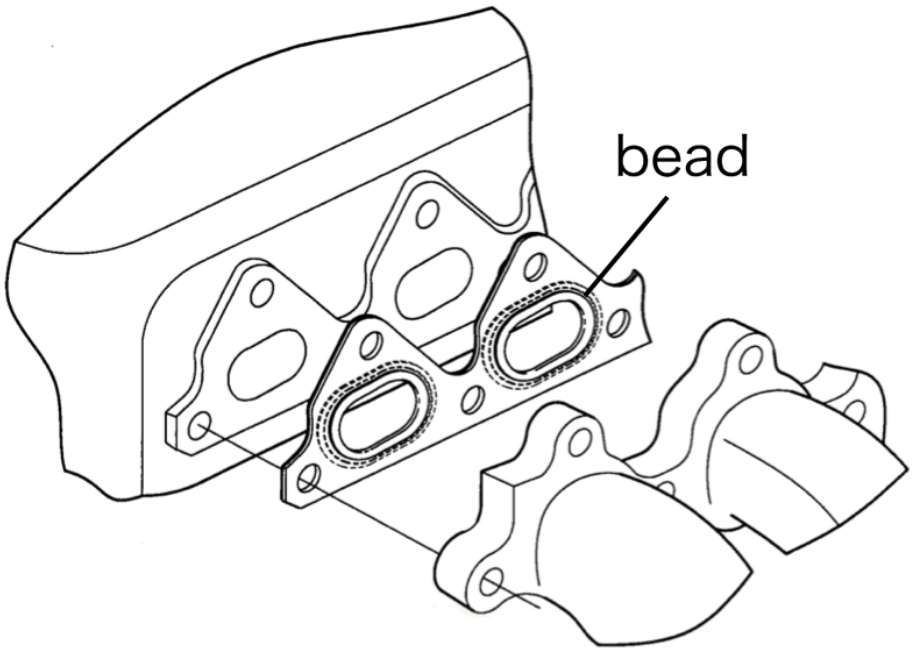

Fig. 1.1 Appearance of gaskets used in cars [6].

chasm between the exhaust parts as far as it maintains its initial shape. When the material becomes soft and the convex part collapses during service, sealability is not guaranteed any more. The temperatures at which these gaskets are exposed to depend on their location with respect to the overall design of the system, including the layout of the cooling water circulation system. Therefore, the materials used for these gaskets vary from conventional stainless steels for relatively mild environments, like 500 °C or lower, to Ni-based superalloys, such as Inconel 718, for temperatures as high as 700 °C [7]. However, even Inconel 718 cannot be adopted if the temperature of the gasket exceeds 700 °C or several gaskets should be stuck, which leads to increasing the costs. As mentioned above, the challenge for developing new materials for the automotive industry is to achieve high performance without either using expensive processing or adding a high amount of costly elements.

Despite the strong demand for alloys that can be adopted as car parts, the development of new materials for this market has progressed only in a sluggish manner. There are several reasons for that. Firstly, as the material is exposed to high temperatures for a long period of time, the microstructure of the material and its properties are prone to change during service, which takes a long time to be assessed quantitatively. Secondly, there are too many possibilities

for alloy optimisation. Every superalloy or stainless steel contains several elements, each of which is added for a specific purpose. The relation between the amounts of each alloy addition and the properties is not necessarily linear, and the effect of each element often influences others. It should be added that also heat treatments strongly affect the alloy properties. Hence, optimising these parameters requires a vast amount of time and money. In summary, the development of new high-temperature alloys is inevitably challenging. In addition to the inherent difficulties in developing high-temperature alloys, the development of alloys for car parts has an extra hurdle; they should be much less costly than those for other industries. For the above reasons, it is highly desired to establish a method to develop new alloys more efficiently. There have been several computational techniques to predict the microstructure and the strength by calculation, which will be stated in detail in the following chapters. In this study, the design of new alloys with the aid of computational simulations is endeavoured.

Although there are many alloys used in a high-temperature environment, it is important to narrow down the potential candidates for the applications considered here. Features required for the materials for exhaust gaskets are high yield strength after a long time exposure to high temperatures and acceptable corrosion resistance. For satisfying these properties, the alloys should have a microstructure with a face-centred cubic (FCC) matrix and fine precipitates that have a coherent interface with the matrix. The FCC matrix is inherently strong and ductile and also beneficial in terms of the stability of the microstructure because the diffusion coefficient in FCC is generally much lower than that in a body-centred cubic (BCC) matrix. For stability of the microstructure, a coherent interface between the matrix and the precipitates is also desired. Based on this discussion, it follows that Ni- and Fe-based alloys with an FCC matrix and fine strengthening precipitates should be the best candidates. However, to design and develop them is, in fact, not so simple because of the following difficulties,

1. Large search space for both chemical composition and processing path
2. Complicated microstructures
3. Long exposure time during service.

Due to these inherent difficulties in developing these alloys, a trial and error approach with an empirical background can easily end up without any fruitful results.

In this study, an integrated computational approach is employed for alloy design. Briefly introducing, microstructural evolution during heat treatment and service at high temperatures

of an alloy are predicted by a phase transformation calculation. Then, yield strength after service is estimated from the calculated microstructural parameters according to classical alloy strengthening theories. Based on the strength estimation, the chemical composition of the potential alloy is optimised from a vast solution space by a genetic algorithm, a nature-inspired heuristic optimisation approach. This work focuses both on the developed alloy as well as the approach for designing it.

1.2 Scope and outline of the thesis

In this thesis, a literature review on microstructures for high-temperature alloys and strengthening modelling approaches are presented in **Chapter 2**. Special emphasis is made on the precipitation evolution and its strengthening effects because the alloys considered here are strengthened mainly by precipitates. Several computational alloy design approaches studied by researchers so far are briefly reviewed in **Chapter 3**. Then, the strategy for alloy design using computational schemes studied in this work is presented in this chapter. The microstructure and strength calculation results are also presented and compared with the experimental values taken from literature. **Chapter 4** explains the actual alloy designing process conducted in this work. A case study for selecting proper calculation parameters for the optimisation is also presented. The optimisation results and experimental validation by using samples made from small ingots are also shown in this chapter by comparing the microstructure and properties of the designed alloy with those of conventional Ni- and Fe-based high-temperature alloys. Further experimental validation in terms of the microstructure and mechanical properties is conducted with an alloy sheet produced by a similar way of mass production procedure in **Chapter 5**. Alloy 718Plus, a relatively newly developed superalloy, was used as a reference material here. The experimental results are compared to the calculated values. **Chapter 6** shows the experimental characterisation of the designed alloy without Tungsten (W), which is supposed to negatively influence the properties of the alloy by promoting the formation of the undesired coarse precipitates. The influence of W on the microstructure and mechanical properties are also analysed by using Alloy 718Plus without W. In this chapter, the chemical composition of the alloy, which can potentially be used for automobile sealing parts is proposed. **Chapter 7** presents the overall conclusions of the work.

Chapter 2

Literature review - Microstructure and mechanical properties of high-temperature alloys

A key aim of the present study is to design a new high-temperature alloy with the aid of several computational tools. In order to design the new alloy, it is essential to predict its microstructural constituents, such as phase formation, fraction, size and chemical composition of the matrix and precipitates, as alloy properties depend on such microstructural parameters. In this chapter, a general outline and features of high-temperature alloys are presented with a special focus on their microstructures. Then, a basic concept for predicting relevant microstructural parameters is presented. Strengthening mechanisms, such as precipitation and their theoretical models are also introduced.

2.1 Outline of high-temperature alloys

2.1.1 High-temperature alloys

Alloys used in high-temperature environments range from conventional carbon steels or stainless steels to superalloys, depending on their operational temperature and the properties required in their corresponding environments. In this thesis, the focus is on superalloys rather than on carbon steels used in relatively mild environments. Superalloys are usually categorised into three groups by its base alloying element, Ni-, Co- and Fe-based; Fe-based superalloys can include stainless steels [1]. Several alloying elements other than these are added for improving properties, such as a room/high-temperature strength, creep life

and high-temperature oxidation resistance. Each element has an intended purpose, such as promoting the formation of desired phases, reducing macro/micro segregation and reducing material costs. Therefore, the selection and amount of alloying elements should be carefully determined for obtaining the aimed properties at the reasonable cost. The producibility of the alloy is also a matter that demands consideration as the producibility often has an inverse relationship with the properties of the alloy; the harder the high-temperature strength is, the more difficult to be hot rolled.
The nominal chemical compositions of common superalloys and the role of each element are presented in Tables 2.1 and 2.2, respectively [1, 4, 8–12]. The role of elements used in the common high-temperature alloys is as follows.

- **Nickel (Ni)**: Ni is the most common base element for superalloys. Ni is an austenite former and also enhances the formation of the strengthening precipitates γ' and γ'', both of which are intermetallic compound consisting of Ni (details will be presented later).
- **Cobalt (Co)**: Co is a common element for superalloys. Co is an austenite former and also is present in γ' and γ'' by occupying lattice positions of Ni. However, the amount of Co should be carefully determined from a commercial point of view, as the addition of Co substantially increases alloy costs.
- **Iron (Fe)**: Some amount of Fe is also added in most superalloys. Fe is a less costly element than other base elements (Ni and Co). So, the amount of Fe is balanced by considering the total elemental cost and properties.
- **Chromium (Cr)**: Most of the high-temperature alloys contain a large amount of Cr to improve oxidation resistance. However, excess Cr content can impair the microstructure stability by forming TPC phases, such as σ phase. Cr also promotes the formation of carbides and borides.
- **Molybdenum (Mo)**: Mo usually increases high-temperature strength via solid solution or carbide formation. However, high Mo content promotes the Laves phase, especially when the alloy contains a high amount of Fe.
- **Aluminium (Al)**: Al forms γ' by being combined with Ni. The amount and size of the precipitates strongly depend on the ratio of Al, Nb and Ti. Al is often added in high-temperature alloys for the formation of Al_2O_3 oxide layer, which improves the oxidation resistance.

- **Titanium (Ti)**: Ti is often added to precipitate-strengthened superalloys as it forms γ' and increases the degree of strengthening effect of γ'. However, large amounts of Ti enhance the formation of η phase, which is usually undesired to be precipitated.
- **Niobium (Nb)**: Nb plays an important role in superalloys by forming γ' and γ''. Nb is also a strong solid solution strengthening element. However, large amounts of Niobium lead to lower solidus temperatures causing difficulties in the hot forming process. Excessive Nb also promotes non-strengthening precipitates: σ, δ and Laves phases.
- **Tantalum (Ta)**: Ta, which is one of the refractory elements, promotes the formation of γ' by replacing Al on the second sublattice in Ni-based superalloys. In general, the stability of γ' at high temperature is improved by adding Ta. In addition, Ta is also a strong MC type carbide former, which can be used for strengthening and grain boundary control.
- **Tungsten (W)**: W usually increases high-temperature strength via solid solution or carbide formation. However, high W content promotes the Laves phase when the alloy contains a high amount of Fe. It is worth mentioning that W is one of the most costly elements.

Table 2.1 Nominal chemical composition of common superalloys and stainless steels in mass%.

Alloy	Ni	Co	Fe	Cr	Mo	Al	Ti	Nb	Mn	Si	V	Zr	W	C	B	Ref
Alloy625	Bal		2.5	21.5	9	0.2	0.2	3.6						0.05		[1]
Alloy 718	Bal		18.5	19.0	3	0.5	0.9	5.1						0.04		[1]
Alloy 718Plus®	Bal	9	10	18.0	2.8	1.45	0.7	5.4					1	0.02	0.006	[9]
Waspaloy	Bal	13.3		19.4	4.3	1.3	3.0							0.035	0.006	[9]
Rene 95™	Bal	8		14.0	3.5	3.5	2.5	3.5				0.05	3.5	0.15	0.010	[1]
Nimonic® 105	Bal	20.1	0.10	15.0	5.0	4.9	1.3		0.30	0.35		0.11		0.128	0.005	[10]
Incoloy 908	47.5		41.8	4.5		2.33	1.8	1.9	0.09	0.35				0.05		[8]
Haynes 21	3.0	Bal	1	27.0	5									0.25		[4]
Incoloy 800	32.5		Bal	21.0		0.38	0.38							0.025		[1]
Alloy A286	25.1		Bal	14.5	1.20	0.25	2.00			0.11	0.20			0.052		[11]
AISI 310S/EN 1.4845	19.4		Bal	24.7			0.01		1.8	0.61	0.18			0.054		[13]
AISI 316/EN 1.4401	10.2		Bal	16.8	2.07				1.7	0.28				0.011		[14]
AISI 304/EN1.4301	8.24		Bal	18.3	0.40				1.7	0.26				0.012		[14]

Table 2.2 Role of alloying elements in superalloys.

Effect	Ni	Co	Fe	Cr	Mo	Al	Ti	Nb	Ta	Zr	Hf	W	C	B
FCC matrix stabiliser	○	○										○	○	
Precipitation (inter metallic) strengthening	○	○				○	○	○	○	○	○			
Precipitation (carbide) strengthening				○	○		○	○	○	○		○	○	
Solid solution strengthening	○	○		○	○			○				○	○	
Improve creep strength	○	○	○		○				○			○	○	○
Improve oxidation resistance				○	○	○								

2.1.2 Common phases in high-temperature alloys

The microstructure of high-temperature alloys usually consists of a matrix with various precipitates. The following and Table 2.3 summarise the phases observed in typical high-temperature alloys.

- γ **(matrix)**:
  In principle, high-temperature alloys should have a face-centred cubic (FCC) crystal structure matrix because of the advantage over other crystal structures. First, the FCC is inherently tough and ductile. Secondly, it has broad solubility, which enables the matrix to accommodate a high concentration of elements as a solid solution. These solute elements, then, can form strengthening precipitates during the ageing treatment. Another advantage of having the FCC matrix is the lower diffusivity of atoms compared with hexagonal close-packed (HCP) and body-centred cubic (BCC) structures. The microstructures of FCC alloys, therefore, are more stable than other crystal structures at elevated temperatures [1].

- γ' **(Ni_3(Al, Ti))**:
  Gamma prime γ', is the primary strengthening phase in most Ni-based superalloys and some Fe-based superalloys [1]. It is an intermetallic compound with an ordered $L1_2$ crystal structure (see Figure 2.1 (a)). Due to an interfacial coherency between γ' and the matrix (γ) with a mismatch of 1 % or even less, γ' nucleates and scatters homogeneously throughout the matrix and is stable for a long period of time at high temperatures. Initially, γ' forms in a spherical shape because a sphere has the least surface area/volume ratio, but it changes to cuboidal as it grows to maintain a continuous γ/γ' interface with $\{100\}_\gamma || \{100\}_{\gamma'}$ and $\langle 010\rangle_\gamma \,||\, \langle 010\rangle_{\gamma'}$ orientation relationship [4, 15].
  Figure 2.2 shows the temperature dependence of the 0.2% flow stress of γ' and Ni-based alloys with γ' [1]. Another important feature in γ' is that its strength has a positive dependence on temperature up to about 800 °C, which stems from the ordered $L1_2$ crystal strcutre[1, 16–18]. This anomalous property of γ' has made the precipitate used in many superalloys.
  Although γ' is often represented by Ni_3(Al, Ti), some other elements can dissolve into the precipitate. For example, Co and Cu can substitute Ni, whereas Nb, V, Ta and Hf

can replace Al or Ti on the second sublattice.

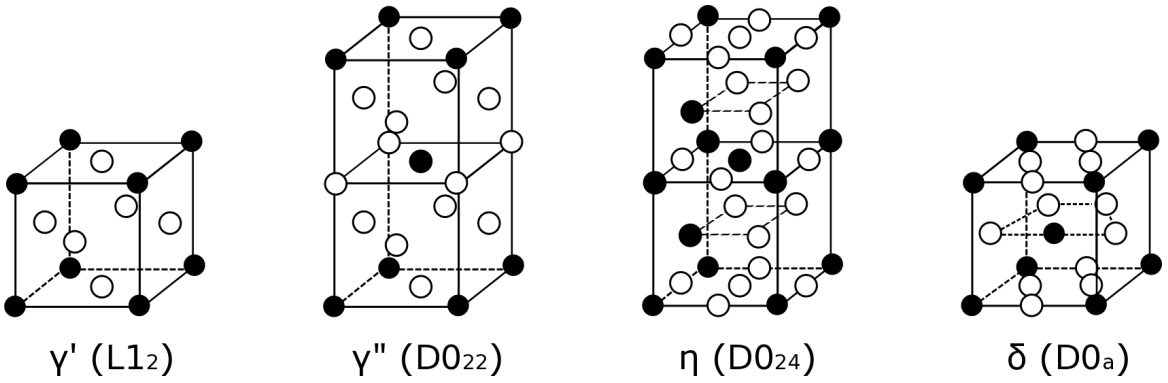

Fig. 2.1 Crystal structures of (a) γ', (b) γ'', (c) η and (d) δ, extracted from Sugimura *et al.* [19]. Open circles represent Ni atoms.

- γ'' **(Ni_3Nb)**:
  Gamma double prime, or γ'', is another intermetallic compound, which has an ordered body-centred tetragonal (BCT) $D0_{22}$ crystal structure with Ni_3Nb stoichiometry (see Figure 2.1 (b)). This precipitate displays the orientation relationship $\{001\}_{\gamma}||\{001\}_{\gamma''}$ and $\langle 100\rangle_{\gamma}\,||\,\langle 100\rangle_{\gamma''}$ with a very small lattice mismatch [4]. The γ'' phase forms as a sphere-shaped precipitate, but it turns into disc-shaped as it grows, which is of great importance for both its precipitation evolution and the influence on the alloy strength [20–22]. The γ'' phase is the principal strengthening precipitate in some alloys with high Nb content, such as Alloy 718 [23].
  As γ'' is a meta-stable phase, when it is exposed to a high-temperature environment for a long period of time, particularly at temperatures above 700 °C, rapid coarsening and dissolution of γ'' occurs followed by the formation of a stable δ phase [4].

- η **(Ni_3Ti)**:
  η phase has a hexagonal $D0_{24}$ crystal structure with a Ni_3Ti composition (see Figure 2.1 (c)). This phase often precipitates in superalloys with high Ti/Al ratios, at the expense of the γ' phase when exposed to a high-temperature environment for a long period of time [24, 25]. In this sense, the formation of this phase is not desired as it lowers the yield strength and creep strength of the alloy due to the consumption of the γ' phase.

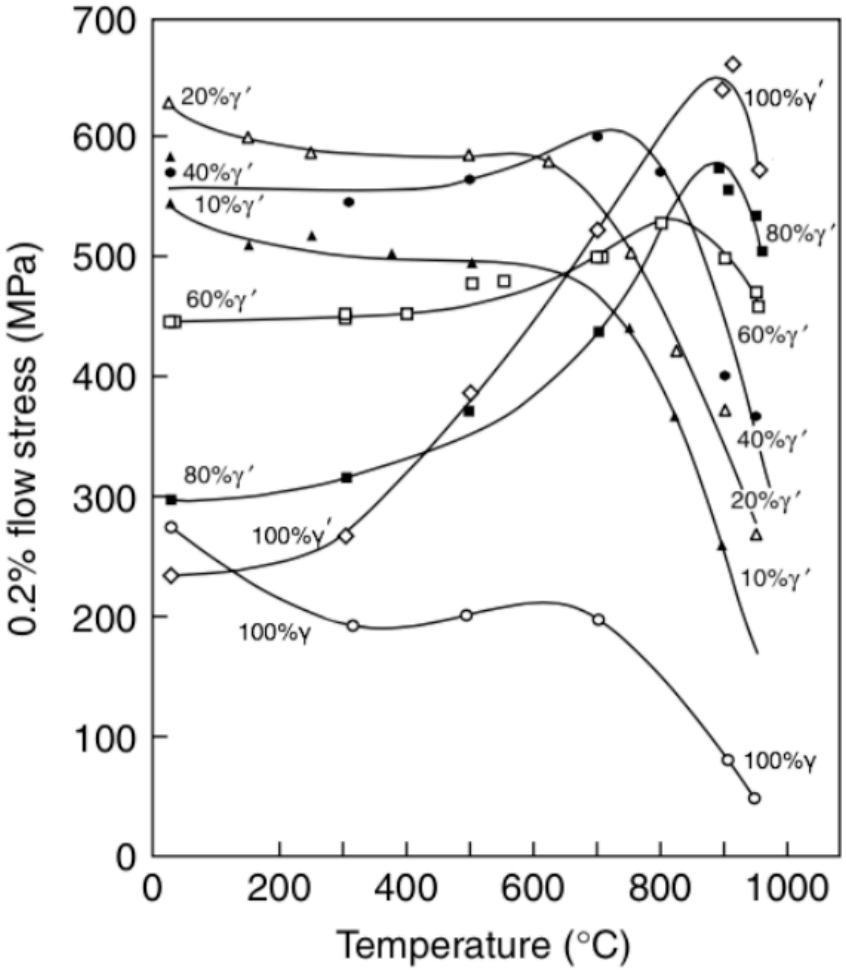

Fig. 2.2 Temperature dependence of 0.2% flow stress of γ' and Ni-based alloy with γ' as the second phase [1].

- δ **(Ni_3Nb)**:
  δ phase has an orthorhombic $D0_a$ structure (see Figure 2.1 (d)) and is observed when superalloys with γ'' are overaged. This stable phase is reported to form at the expense of metastable γ'', so it has a negative influence on the strength of the alloy [26]. Therefore, the δ phase should be suppressed during the ageing treatment and service, although this phase can be used for grain size control during hot working and solution treatment as is η phase [27, 28].

- **Laves (A_2B)**:
  Conversely to geometrically close-packed (GCP) precipitates, such as γ', topologically

close-packed (TCP) phases, such as Laves, μ and σ, have layers of close-packed atoms and are recognised as deleterious because TCP phases are not only brittle but also deplete the potent strengthening elements in the matrix [29]. Laves is a plate-like phase with an A_2B stoichiometry and has an orientation relationship with the matrix of $(004)_{\text{Laves}}||\{111\}_\gamma$, $[110]_{\text{Laves}}||\langle 110\rangle_\gamma$ [30]. Si, Nb, Mo, W and Fe promote the formation of this phase, which affects subsequent precipitation in its vicinity due to the depletion of Nb [5, 28, 31].

- μ **($\mathbf{A_6B_7}$)**:
  μ phase is a TCP phase with an A_6B_7 stoichiometry, *e.g.* Ni_6Nb_7 in the Ni-Nb system. Owing to its poor mechanical properties, the presence of μ degrades the mechanical properties of the alloy. Moreover, the formation of μ leads to chemical degradation, due to the loss of Nb in the matrix [32].
- σ **($\mathbf{A_xB_y}$)**:
  σ is another TCP phase and a hard and brittle precipitate with a complex chemical composition. The formation of σ is more common in Fe- and Co-based alloys than in Ni-based alloys. The σ phase nucleates and grows from the liquid and/or from the γ matrix during solution treatment [29, 33]. As σ imparts brittleness and a degradation of creep-rupture strength, its formation is usually undesired.

- **Carbides ($\mathbf{M_6C}$, $\mathbf{M_{23}C_6}$, $\mathbf{M_7C_3}$, MC)**: Carbides like M_6C, $M_{23}C_6$, M_7C_3 and MC, where M represents a metallic element, are sometimes observed in common high-temperature alloys. The typical metallic elements that form carbides are Cr, Fe, Ti, Nb, V, Co, Ta and W [4, 5]. Some carbides on grain boundaries retard grain growth.
- **Borides ($\mathbf{M_3B_2}$)**: A small amount of B is often added to superalloys because this element retards the formation of η phase at grain boundaries and strengthen grain boundaries [5]. However, if a high amount of B is added, it segregates to grain boundaries and forms detrimental borides with Mo and Nb [34].

Table 2.3 Precipitates in superalloys (GBs, TBs and SFs stand for grain and twin boundaries and stacking faults, respectively).

	Crystal structure	Region	Morphology	Size range /nm	Interface	Young's modulus /GPa	References
γ	FCC		matrix	1.0-5.0x10^5	-	207	[1]
γ' Ni_3(Al,Ti)	FCC	matrix	from spherical to cuboidal	10-50 (appropriate size)	coherent with γ (<1% mismatch)	178, 253	[4, 35–37]
γ'' Ni_3(Nb)	BCT	matrix	from spherical to disc shaped	10-100 (appropriate size)	coherent with γ 1-4% mismatch	235	[5, 38, 39]
η Ni_3Ti	HCP	matrix	cellular at GBs platelets at matrix	several 10^3	incoherent with γ		[4, 25, 29]
δ Ni_3Nb	orthorhombic	GBs matrix	acicular cellular	100-3000	incoherent with γ		[4, 26, 40]
Laves A_2B	hexagonal	GBs matrix	globules platelets	100-3000	$(004)_{Laves}\|\|\{111\}_\gamma$ $[110]_{Laves}\|\|<110>_\gamma$		[4, 30, 31, 41]
μ A_7B_6	rhombohedral	matrix	platelets	- several 10^3	coherent with both γ&γ'		[4, 32, 42]
σ A_xB_y	tetragonal	GBs	globules	- several 10^3	$(111)_\gamma\|\|(001)_\sigma$ $[011]_\gamma\|\|[110]_\sigma$		[4, 29, 33]
M_6C	FCC	matrix (primary) GBs (secondary)	Widmanstatten blocky at GBs	- several 10^3			[4, 43–45]
$M_{23}C_6$	FCC	GBs, TBs SFs	globular, film platelets lamellar	- several 10^3			[4, 43–46]
M_7C_3	hexagonal	GBs	blocky	- several 10^3			[4]
MC	cubic	matrix	round, blocky	- several 10^3		370-670	[4, 43, 44, 47]
M_3B_2	tetragonal	GBs	blocky	- several 10^3		390	[4, 34, 45, 48]

2.1.3 Processing schedules and microstructure evolution

As the final product aimed for in this study is a sealing component, the alloys are produced as a thin sheet. The alloy sheet is produced from slabs by hot/cold rolling and subsequent heat treatment steps. The slab is prepared by ingot metallurgy through a cast-wrought route rather than powder-metallurgy because of high processing costs. Also, monocrystal superalloys, which are often used for turbine blades of an aeroplane, are not considered for the same reason.

A typical sequence for preparing the cast and wrought slab starts from vacuum induction melting followed by remelting. Impurities are reduced in both melting processes. These processes are followed by homogenisation and hot rolling for tailoring the shape of the material and reducing microsegregation.

Although the slab preparation procedures are important for obtaining the desired microstructures and properties, heat treatments and cold rolling applied at the last few stages of production are more critical to the microstructures and mechanical properties of the final product. In general, two heat treatments, solutionising and ageing, are adopted for precipitation-strengthened high-temperature alloys. The solutionising is conducted so that secondary phases, which formed at previous stages, dissolve into the matrix. Although this treatment is sometimes conducted on conditions that a small amount of precipitates still remains at the grain boundaries for preventing rapid grain growth, the main purpose of solutionising is to attain a homogenised matrix where no secondary phase exists. During the cooling stage after the solutionisng, very fine γ' and γ'' particles form in the matrix. The next step is an ageing treatment, where the strengthening particles (γ' and γ'') dispersed in the matrix are controlled to an appropriate size.

While the microstructures of high-temperature alloys can vary depending on chemical composition and heat treatment, the typical microstructure evolution can be summarised as in Figure 2.3. After solutionising treatment (Figure 2.3 (a)), the γ matrix is the only phase except for some coarse primary carbides and/or the secondary phases at the grain boundaries. Then, fine precipitates, such as γ' and γ'', form throughout the matrix during ageing (Figure 2.3 (b)). These fine precipitates grow and coarsen during ageing and service at high temperatures, and finally transform into platelets or rather bulky coarse precipitates, which have less coherent interfaces with the matrix (Figure 2.3 (c)).

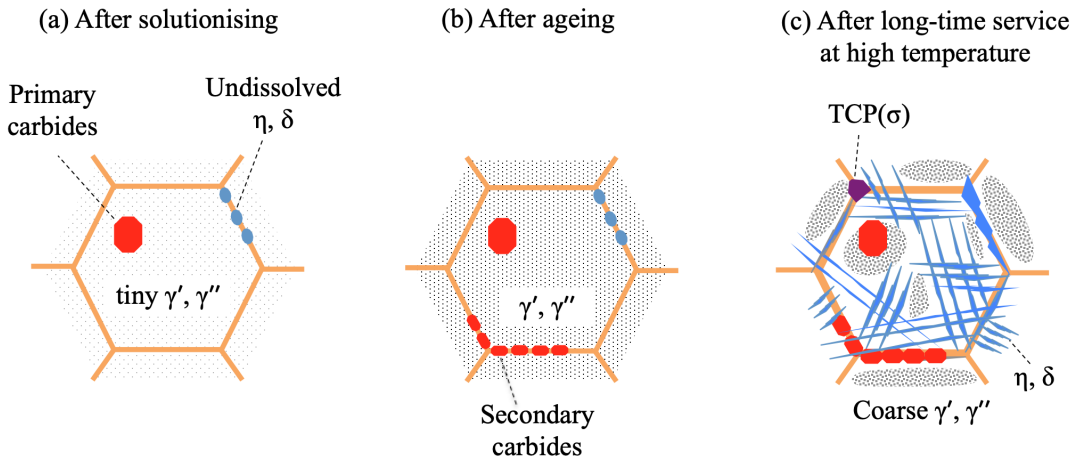

Fig. 2.3 Schematic illustrations of microstructure evolution: after (a) solutionising, (b) ageing heat treatment and (c) service at high temperature.

The microstructure evolution can also be described by the time-temperature-transformation (TTT) diagram (Figure 2.4 [49]). Solutionising treatment is usually carried out above the δ solvus line. Then, the alloy is aged to control γ' and γ'' particles. It is obvious from the TTT diagram, undesired phases, such as δ, are observed after long-time exposure to the high-temperature environment.

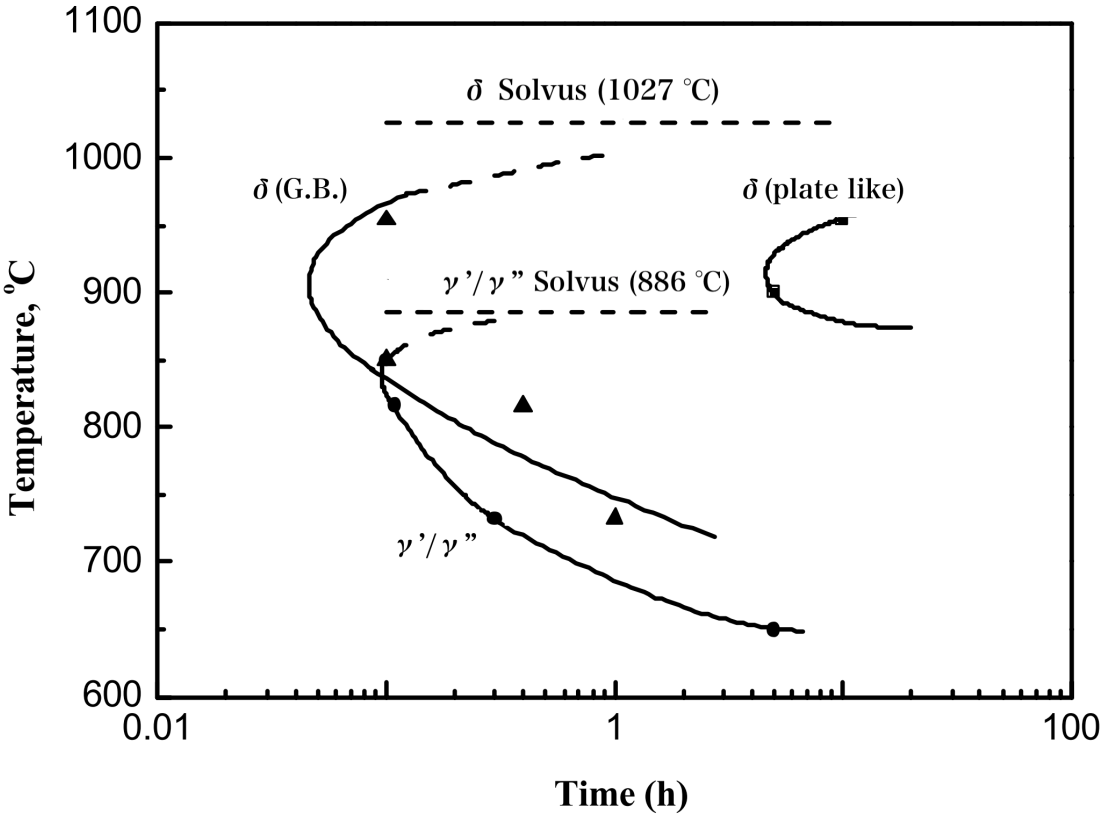

Fig. 2.4 Time-temperature-transformation diagram of Inconel 718 [49].

2.1.4 Mechanical properties of high-temperature alloys

Mechanical properties of high-temperature alloys depend upon their microstructure. Particularly, the volume fraction and size of γ' and γ'' are very influential on the high-temperature strength of the alloys. Fig 2.5 shows the relationship between yield stress at 650 °C and fraction of γ' and γ''. As the volume fraction of these precipitates increases, the high-temperature yield stress increases. The size of precipitates is also important as shown in Fig. 2.6. The increment of the critical resolved shear stress (CRSS) by γ' increases as the size of precipitates increases. However, when the precipitate becomes larger than a certain radius, the CRSS decreases with precipitate size. This can be explained by a combination of several precipitation strengthening mechanisms.
Theoretical descriptions of the precipitation evolution and strengthening by precipitations in high-temperature alloys are reviewed in the next section.

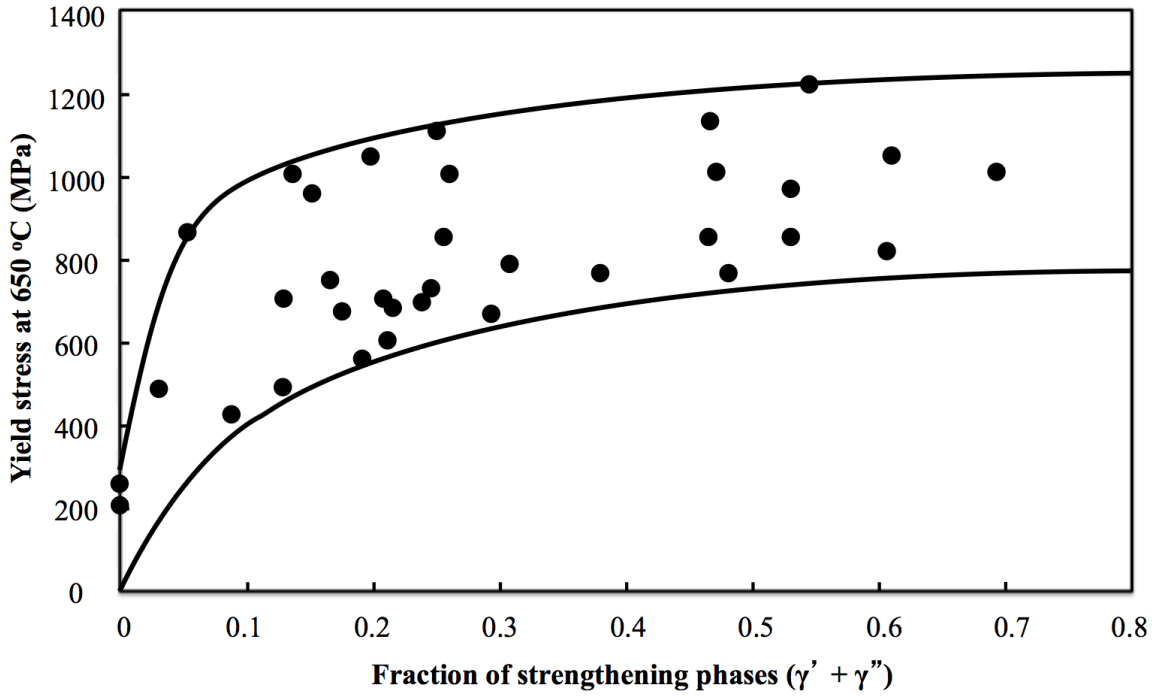

Fig. 2.5 Yield stress of common turbine disc alloys at 650 °C with the total fraction of the γ' and γ'' [1].

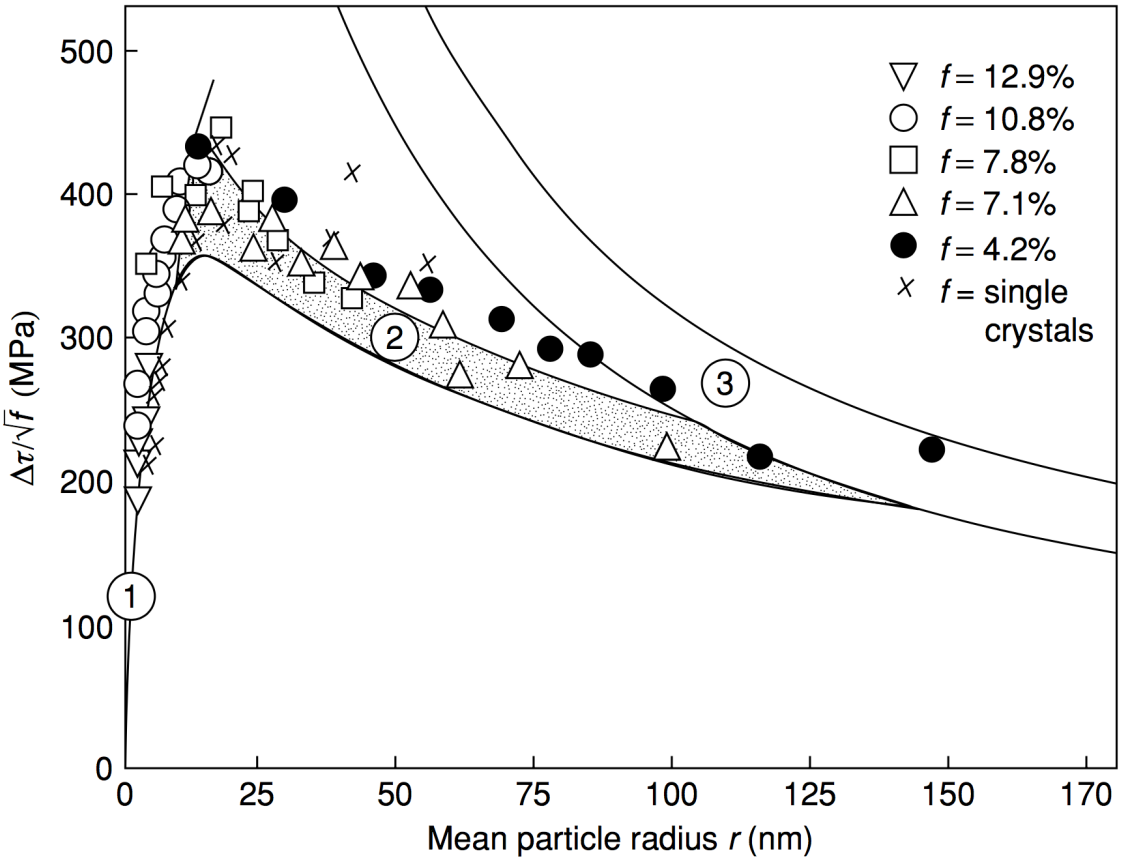

Fig. 2.6 Critical resolved shear stress (divided by the square root of the volume fraction f) *vs* mean precipitate radius in Nimonic PE16 [1].

2.2 Microstructure evolution in high-temperature alloys

The development of precipitates, which plays a key role in microstructure evolution, can be divided into three stages: nucleation, growth and coarsening, although they sometimes overlap each other as illustrated in Figure 2.7. During the first stage of microstructure evolution, nuclei of a new phase form in the supersaturated matrix. Following nucleation, the particle grows by incorporating atoms from the matrix. At this growth stage, the fraction and size of precipitates increase with time. Finally, the large precipitate becomes even larger at the expense of smaller precipitates. Therefore, the number density of particles decreases at this coarsening stage. In this section, established theories for describing these precipitation evolution stages are reviewed and put together in the context of a unifying numerical modelling scheme.

2.2.1 Nucleation

In the classical nucleation theory, the free energy change of a system undergoing the nucleation of a new phase (ΔG) depends on three contributions: (1) volume free energy reduction $-V\Delta G_{\mathrm{v}}$, (2) increase in interfacial energy between the matrix and the nucleus $A\gamma_{\mathrm{int}}$ and (3) misfit strain energy $V\Delta G_{\mathrm{st}}$ [50], which is illustrated in Figure 2.8 and expressed as

$$\Delta G = -V\Delta G_{\mathrm{v}} + A\gamma_{\mathrm{int}} + V\Delta G_{\mathrm{st}}, \tag{2.1}$$

where ΔG is the free energy change, V is the volume, γ_{int} is the interfacial energy between a matrix and nucleus.

Assuming the nuclei are spherical with a mean radius r, Equation 2.1 can be rewritten as follows:

$$\Delta G = -\frac{4}{3}\pi r^3(\Delta G_{\mathrm{v}} - \Delta G_{\mathrm{st}}) + 4\pi r^2\gamma_{\mathrm{int}}. \tag{2.2}$$

By differentiating Equation 2.2 with respect to r, the critical radius (r^*) and the critical energy (ΔG^*) are derived as

$$r^* = \frac{2\gamma_{\mathrm{int}}}{\Delta G_{\mathrm{v}} - \Delta G_{\mathrm{st}}} \tag{2.3}$$

and

$$\Delta G^* = -\frac{16\pi\gamma_{\mathrm{int}}^3}{3(\Delta G_{\mathrm{v}} - \Delta G_{\mathrm{st}})^2}. \tag{2.4}$$

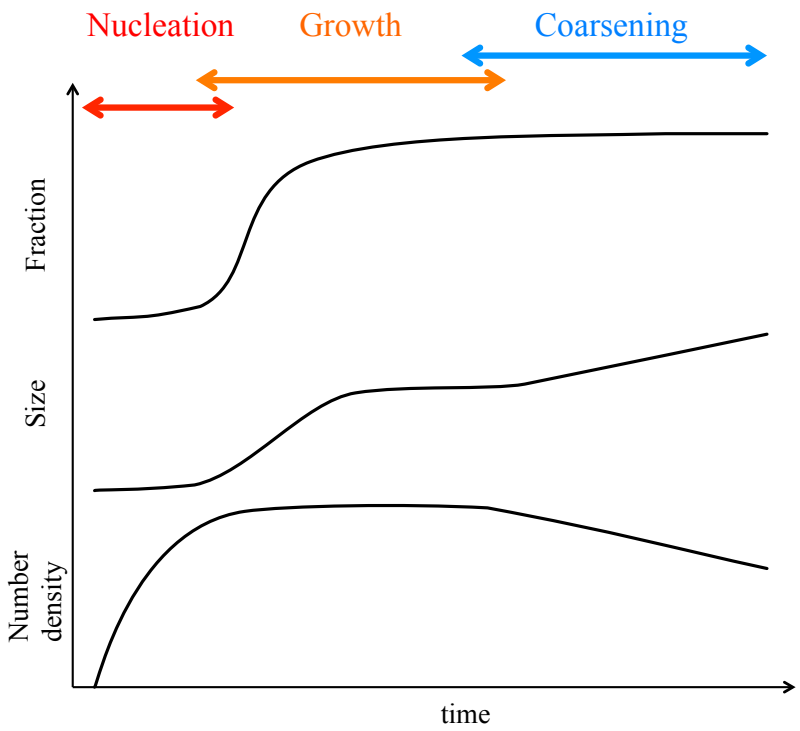

Fig. 2.7 Schematic illustration of fraction, size and number density of precipitates during microstructure evolution.

The nucleus should have a radius larger than r^* for growing, otherwise, it dissolves into the matrix. Statistically, the concentration of the nucleus whose radius is r^* is given by

$$C^* = C_0 \exp\left(\frac{-\Delta G^*}{k_B T}\right), \tag{2.5}$$

where C^* is the number density of atomic clusters with radius r^*, C_0 is the total number of atoms per unit volume, which corresponds to the number of potential nucleation sites for homogeneous nucleation, and k_B is Boltzmann constant [50].
According to Russell [51], the steady-state nucleation rate (J_s) is described with C^*, the Zeldovch factor (Z) and an atomic attachment rate (β^*) by

$$J_s = Z\beta^* C^* = Z\beta^* C_0 \exp\left(\frac{-\Delta G^*}{k_B T}\right). \tag{2.6}$$

While Equation 2.6 assumes an equilibrium distribution of atoms and atomic clusters, an expression for the nucleation rate with time dependence (J) has been proposed by Turnbull

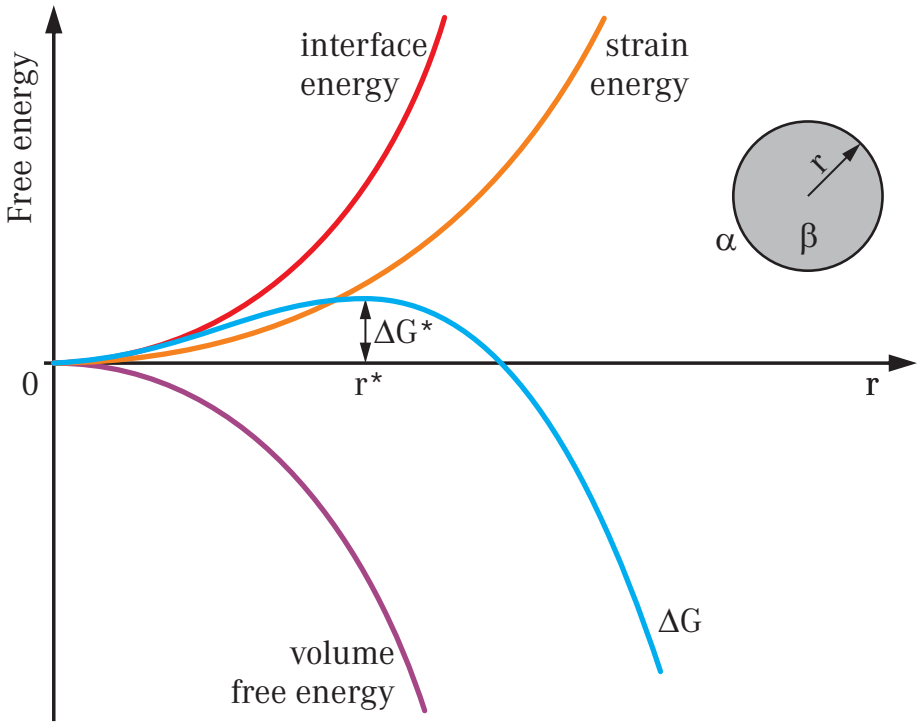

Fig. 2.8 Schematic illustration of free energy change by precipitation based on a classical nucleation theory.

[52] as

$$J = J_s \exp\left(-\frac{\tau_{\text{inc}}}{t}\right) = Z\beta^* C_0 \exp\left(\frac{-\Delta G^*}{k_B T}\right) \exp\left(-\frac{\tau_{\text{inc}}}{t}\right), \tag{2.7}$$

where τ_{inc} is the incubation time and t is time.

In a multicomponent system, β^* is expressed as a function of the concentration of each element in both the precipitate and the matrix and the diffusivity of each element in the matrix [53]. This can be expressed as the following equation:

$$\beta^* = \frac{4\pi (r^*)^2}{a_{\text{ia}}^4 V_\alpha} \left[\sum_{i=1}^{n} \frac{(c_{i\beta} - c_{i\alpha})^2}{c_{i\alpha} D_{i\alpha}}\right]^{-1}, \tag{2.8}$$

where a_{ia} is the interatomic distance, V_α is the molar volume, $c_{i\beta}$ and $c_{i\alpha}$ are the concentration of element i in the precipitate and the matrix, respectively, and $D_{i\alpha}$ is the tracer diffusivity of element i in the matrix.

The description above is based on the homogeneous nucleation theory. Regarding heterogeneous nucleation, which occurs at crystallographic defects, Equation 2.1 can be rewritten by

adding a term reducing the free energy of defects (ΔG_{def}) as

$$\Delta G = -V\Delta G_{\mathrm{v}} + A\gamma_{\mathrm{int}} + V\Delta G_{\mathrm{st}} - \Delta G_{\mathrm{def}}. \tag{2.9}$$

Therefore, the critical energy of the heterogeneous nucleation is lower than that of homogeneous nucleation due to non-equilibrium defects: vacancies, dislocations, stacking faults, grain and interphase boundaries and free surface, whose ΔG_{def} typically increases in this sequence [50].
As for some Ni-based superalloys, it has been reported that γ', which is the primary strengthening precipitates, can be formed via a spinodal decomposition depending on the chemistries and processing conditions of the alloy [54, 55]. However, whether the γ' precipitation at an early stage of the precipitate formation occurs by classical nucleation or spinodal decomposition has not been fully understood and still remains to be discussed. In the present work, the formation of γ' is recognised as the consequence of the classical nucleation rather than the spinodal decomposition.

2.2.2 Precipitate growth

Precipitate growth can be described in terms of the advancement of the interface between the precipitate particle and the matrix. The boundary migration has been conventionally modelled with a mass balance equation and following the local equilibrium hypothesis. Then, an approach based on the thermodynamic extremal principle has also been developed.

Mass balance model

A classical precipitate growth theory is based on mass balance at the matrix/precipitate interface, which is schematically illustrated in Figure 2.9 (a). The mass balance can be expressed by Equation 2.10 with the flux of element *i* into the matrix from the precipitate ($J_{i\alpha}$) and the flux into the precipitate from the matrix ($J_{i\beta}$). The difference in concentration of *i* at the matrix and at the precipitate times the velocity of the interface movement (v) determines the flux across the interface [53].

$$J_{i\alpha} + J_{i\beta} = \left(c_{i\beta} - c_{i\alpha}\right) \cdot v. \tag{2.10}$$

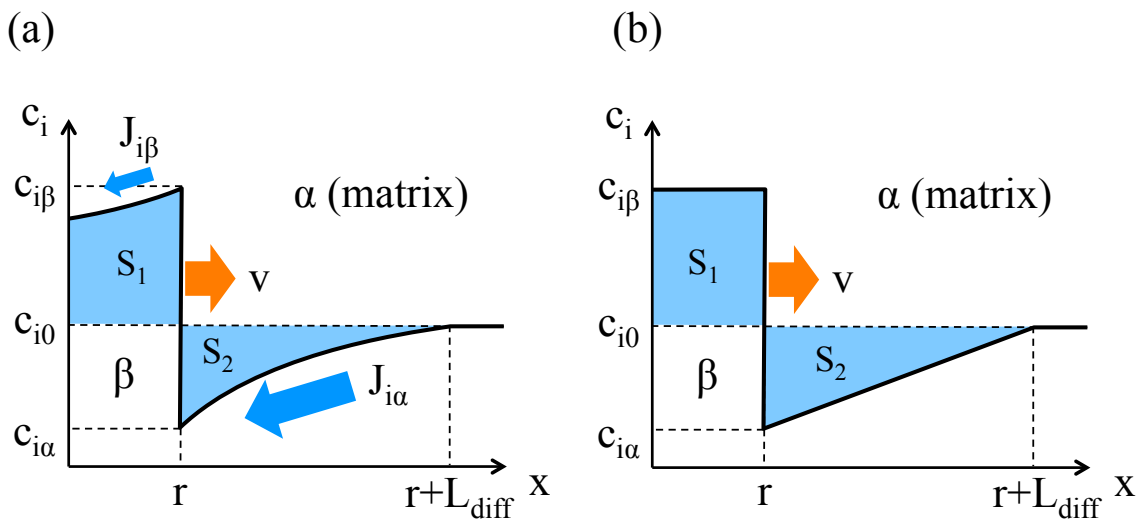

Fig. 2.9 Schematic illustration of the growth of a spherical precipitate (β) in a matrix (α) based on (a) mass-balance model and (b) Zener's assumption.

The precipitate growth rate, therefore, can be acquired by solving this mass balance equation. Assuming the number of components is n, the system has $4n-3$ unknown variables: $2(n-1)$ for the chemical compositions at both sides of the interface, $2(n-1)$ for the flux to the matrix from the precipitate and to the precipitate from the matrix and one for the interface velocity. This problem can be solved by adopting several practical assumptions, which were originally introduced by Zener [56]. First, the interface mobility is assumed to be sufficiently high so that the movement is controlled by diffusion. Second, local equilibrium at the interface is assumed, which provides the chemical compositions at both sides of the interface by thermodynamic calculation. Third, the precipitate is considered to be stoichiometric, *i.e.* $J_{i\beta}=0$. Finally, as illustrated in Figure 2.9 (b), the concentration gradient in the matrix is assumed to be linear.

Then, the mass balance equation can be rewritten as

$$v=\frac{J_{i\alpha}}{c_{i\beta}-c_{i\alpha}}=\frac{D_{i\alpha}\frac{\partial c_i}{\partial x}}{c_{i\beta}-c_{i\alpha}}=\frac{D_{i\alpha}\left(c_{i0}-c_{i\alpha}\right)}{\left(c_{i\beta}-c_{i\alpha}\right)L_{\mathrm{diff}}}, \tag{2.11}$$

where $D_{i\alpha}$ is the diffusion coefficient of i in the matrix α, c_{i0} is the nominal content of i and L_{diff} is the length of the diffusion zone. The conservation law that the area S_1 in the figure is equal to S_2 gives

$$\left(c_{i\beta}-c_{i0}\right)r=\frac{1}{2}\left(c_{i0}-c_{i\alpha}\right)L_{\mathrm{diff}}. \tag{2.12}$$

From Equations 2.11 and 2.12, the interface velocity is expressed as

$$v = \frac{D_{i\alpha}(c_{i0} - c_{i\alpha})^2}{2r(c_{i\beta} - c_{i\alpha})(c_{i\beta} - c_{i0})}. \tag{2.13}$$

Finally, the radius of the precipitate is given by integrating this equation for v as

$$r = \frac{(c_{i0} - c_{i\alpha})}{(c_{i\beta} - c_{i\alpha})^{\frac{1}{2}}(c_{i\beta} - c_{i0})^{\frac{1}{2}}} (D_{i\alpha} t)^{\frac{1}{2}}. \tag{2.14}$$

This equation indicates that the radius of the precipitate increases with $t^{1/2}$ in the growth stage.

The SFFK model

The mass-balance model describes the precipitate evolution in many cases with sufficient accuracy. However, its complexity prevents it from being adopted for calculating complex multicomponent-multiphase systems. On the contrary to the mass-balance model, an approach based on the thermodynamic extremal principle (TEP) with a mean-field approach is more appropriate for solving the problem, especially when considering computational speeds. The basic concept of the TEP, which was originally proposed by Onsager in 1931 [57], is that the reaction occurs along a particular path that produces the maximum entropy. It has been improved for analysing the precipitate evolution in multicomponent and multiphase alloys, which is now recognised as the SFFK model after four main contributors: Svoboda, Fischer, Fratzl and Kozeschnik [58, 59].
This model assumes maximising the entropy production ($\dot{S}$) at a constant temperature is equivalent to maximise the Gibbs energy dissipation rate ($\partial G/\partial t$), which is expressed as

$$\dot{S} = -\frac{1}{T}\frac{\partial G}{\partial t}. \tag{2.15}$$

According to the SFFK model, the total Gibbs energy of a system with n components and m precipitate species can be expressed as

$$G = \underbrace{\sum_{i=1}^{n} N_{i\alpha}\mu_{i\alpha}}_{\text{I}} + \underbrace{\sum_{k=1}^{m} \frac{4\pi r_k^3}{3}\left(\Delta G_{\text{st},k} + \sum_{i=1}^{n} c_{ik}\mu_{ik}\right)}_{\text{II}} + \underbrace{\sum_{k=1}^{m} 4\pi r_k^2 \gamma_{int}}_{\text{III}} \tag{2.16}$$

where $N_{i\alpha}$ and $\mu_{i\alpha}$ are the numbers of moles and the chemical potential of component i in the matrix, respectively, k represents the precipitate species and $\Delta G_{\mathrm{st},k}$ is the specific chemical energy generated by volume misfit. The term I represents the Gibbs energy of the matrix, II stands for the bulk free energies of all precipitates and III is the matrix/precipitate interfacial energy contribution.

Under the TEP assumption, the Gibbs energy dissipation rate is expressed as the sum of three contributions: the movement of the matrix/precipitate interface, diffusion in the precipitate and diffusion in the matrix [58]. This can be expressed as

$$-\frac{\partial G}{\partial t} = \sum_{k=1}^{m} \frac{4\pi r_k^2}{M_{int,k}} \dot{r}_k^2 + \sum_{k=1}^{m}\sum_{i=1}^{n} \frac{4\pi RT r_k^5}{45 c_{ki} D_{ik}} \dot{c}_{ik}^2 + \sum_{k=1}^{m}\sum_{i=1}^{n} \frac{4\pi RT r_k^3 \left(\dot{r}_k (c_{ik} - c_{i\alpha}) + r_k \dot{c}_{ik}/3\right)^2}{c_{i\alpha} D_{i\alpha}} \tag{2.17}$$

where $M_{int,k}$ is the interface mobility, which is dealt with as a coefficient. Parameters, such as the radius and the chemical composition of the precipitate are obtained by solving these equations.

2.2.3 Precipitate coarsening

In the latter stages of precipitation evolution, large precipitates become even coarser and smaller particles dissolve for minimising the total interfacial energy. This behaviour is called Ostwald ripening after the chemist who first described this phenomenon [60]. The origin of Ostwald ripening is explained by the Gibbs-Thomson effect, which is expressed as

$$\Delta P = \frac{\gamma_{int}}{r} \tag{2.18}$$

where ΔP is the pressure due to the matrix/precipitate interface [53]. It is obvious, from the equation, that the pressure has an inverse relationship with the particle radius. Accordingly, smaller particles have a higher molar free energy than larger ones. As schematically illustrated in Figure 2.10, the difference in energy due to the precipitate curvatures works as the driving force for Ostwald ripening.

This behaviour was analysed further by Lifshitz, Slyozov and Wagner, which resulted in the LSW theory [61, 62]. According to this approach, the growth rate of a spherical particle in this stage can be expressed as

$$r^3 - r_0^3 = k_{\mathrm{lsw}} \cdot t \tag{2.19}$$

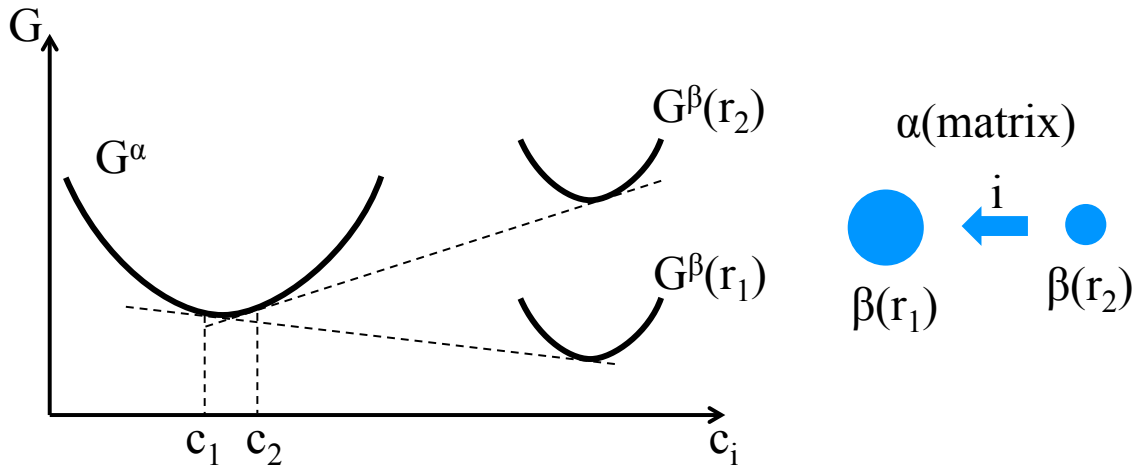

Fig. 2.10 Schematic illustration of the Gibbs-Thomson effect, which describes the origin of precipitate coarsening.

and

$$k_{\mathrm{lsw}} = \frac{8D_{i\alpha}\gamma_{int}c_{i\alpha}V_{\beta}}{9\left(c_{i\beta}-c_{i\alpha}\right)RT} \tag{2.20}$$

where k_{lsw} is a coefficient, r and r_0 are the mean radius of the particle at time t and $t = 0$ and V_{β} is the molar volume of the precipitate. An important indication here is that, at this stage, the radius of the precipitate increases as $t^{1/3}$.

2.2.4 Numerical modelling for precipitation evolution

In the previous sections, several basic theories that describe precipitate evolution have been reviewed. These theories can be integrated by the following numerical models for precipitation volume fraction and particle size distribution (PSD) simulations.

JMAK model

The first model is the Johnson-Mehl-Avrami-Kolmogorov (JMAK) model [63–65]. In this model, the progress of overall phase transformation (ξ) is expressed in terms of the system volume (V) and the extended volume (V_{ex}) as follows:

$$\xi = 1 - \exp\left(\frac{-V_{\mathrm{ex}}}{V}\right), \tag{2.21}$$

where V_{ex} is the total extended volume of the precipitates estimated by assuming no particle impingement. Accordingly, it can be bigger than the volume of the system at the later stages

of transformation. ξ changes from 0 ($V_{ex} = 0$) to 1 ($V_{ex} = \infty$) as the transformation progresses. If nucleation and growth progress at a constant rate J and $\dot{r}$, respectively, the number of nuclei created during the period between τ and $\tau + d\tau$ is $VJd\tau$ and the extended volume at t per particle is $\frac{4}{3}\pi(\dot{r}(t-\tau))^3$. Therefore, the total extended volume in the system will be

$$V_{ex} = \int_0^t \frac{4}{3}\pi \left(\dot{r}\left(t-\tau\right)\right)^3 VJd\tau = \frac{\pi}{3}\dot{r}^3 VJt^4. \tag{2.22}$$

From Equation 2.21 and 2.22, the following expression is deduced.

$$\xi = 1 - \exp\left(-\frac{1}{3}\pi\dot{r}^3 Jt^4\right) = 1 - \exp\left(-k\cdot t^4\right). \tag{2.23}$$

While Equation 2.23 is derived by assuming constant nucleation and growth rates, a generic form of this equation is

$$\xi = 1 - \exp\left(-k\cdot t^n\right) \tag{2.24}$$

where k and n are the Avrami coefficient and exponent, respectively, and they depend on the nucleation and growth mechanisms. The fraction evolution of the precipitate is estimated by adopting proper values for k and n, and multiplying the fraction of the second phase at the equilibrium state.

LS model

A differential equation for describing the size distribution function of precipitates, $f(r,t)$, is

$$\frac{\partial f(r,t)}{\partial t} = \frac{\partial}{\partial r}\left(f(r,t)\dot{r}\right) + j(r,t) \tag{2.25}$$

where $j(r,t)$ is the nucleation rate of precipitates of radius r at time t. In LS model, which was proposed by Langer and Schwarz in 1980, two major assumptions are employed for simplifying the analysis of the precipitate distribution [66]. First, the model only takes into consideration the precipitates whose radius is bigger than the critical radius. Therefore, the nucleation rate in the entire system is given by

$$J = \int_{r^*}^{\infty} j(r,t)dr \tag{2.26}$$

Second, the size distribution of the particle $f^*(r^*,t)$ is assumed to obey

$$f^*(r^*,t) = N_{LS}\frac{b_{LS}}{\bar{r} - r^*}, \tag{2.27}$$

where N_{LS} is the total number of precipitates in the system, b_{LS} is a constant and $\bar{r}$ is the mean radius of the particle. Figure 2.11 schematically illustrates the precipitate size distribution (PSD) by these two assumptions.

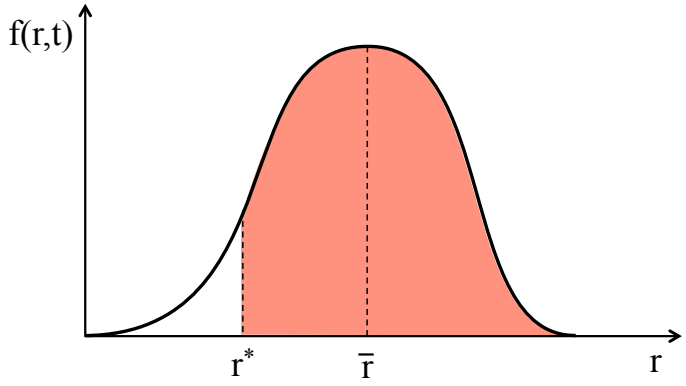

Fig. 2.11 Schematic illustration of precipitate size distribution based on the LS model.

From these assumptions, the evolution of the total number of precipitates and the mean radius is given by

$$\frac{\mathrm{d}N_{\mathrm{LS}}}{\mathrm{d}t} = J - f^*(r^*,t)\frac{\mathrm{d}r^*}{\mathrm{d}t} \tag{2.28}$$

and

$$\frac{\mathrm{d}\bar{r}}{\mathrm{d}t} = v_{\bar{r}} + (\bar{r} - r^*)\frac{f^*(r^*,t)}{m_{\mathrm{LS}}}\frac{\mathrm{d}r^*}{\mathrm{d}t} + \frac{1}{m_{\mathrm{LS}}}J_{r^*}(r^* + \Delta r^* - \bar{r}) \tag{2.29}$$

where $v_{\bar{r}}$ is the radial growth rate of precipitates with the mean radius in a supersaturated matrix, J_{r^*} is the nucleation rate of the critical size particle and $r^* + \Delta r^*$ represents the size of the nuclei, which is slightly larger than the critical value. These equations can be solved by the mass balance law.
Later, Kampmann and Wagner incorporated the Gibbs-Thomson effect with the LS model, which is called the modified LS model, or the MLS model [63].

KWN model

A numerical model proposed by Kampmann and Wagner (KWN model) is now widely used for calculating precipitate evolution [63]. The model is based on the MLS model and some additional modifications have been incorporated. First, while the MLS model describes a continuous size distribution of the precipitates by a rough approximation with Equation 2.27, the KWN model assumes a discrete distribution of precipitate sizes as schematically illustrated in Figure 2.12. Hence, the distribution function $f(r,t)$ is subdivided into size

classes represented by c. The number of precipitates (n_c) and their radius (r_c), which are defined for each class, are identical in the same class.
The time is also discretised in this model by employing a time interval, in which the precipitate parameters remain constant. In addition, precipitates smaller than the critical size, which is ignored in the MLS model, are considered in this model. This has an influence on the estimation of the precipitate parameters particularly in the coarsening stage, where some particles become smaller than the critical radius.

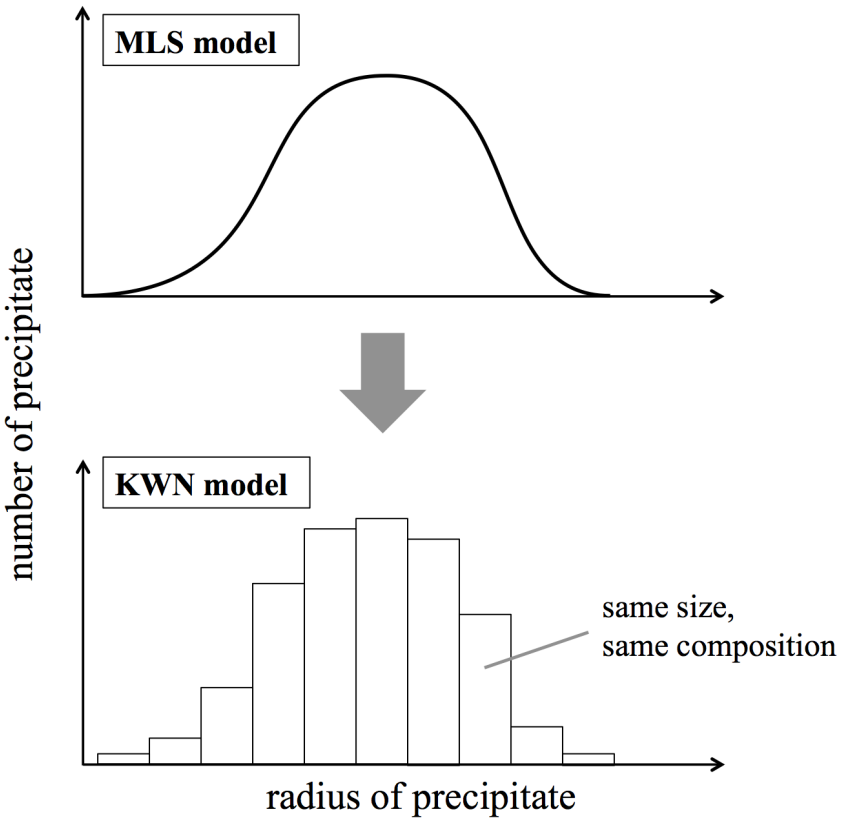

Fig. 2.12 Schematic comparison between MLS and KWN models.

2.3 Precipitation strengthening

In this study, it is necessary to estimate the yield stress of an alloy from microstructural parameters, such as the volume fraction or size of precipitates and the chemical composition of the matrix. The alloys studied in this work are strengthened by several mechanisms. Here, theoretical models for describing the strengthening are summarised. Of all strengthening mechanisms, precipitation strengthening is the most important and effective, although also solid solution and grain boundary strengthening play an important role in obtaining high strength.

2.3.1 Shearable precipitates

Precipitates that work as strengthening media can be divided into two categories: shearable and non-shearable. In general, shearable precipitates are small and observed in the early stages of ageing, while non-shearable precipitates, which are observed at the late stages of precipitation evolution, are too large for dislocations to proceed by cutting. Shearable particles can be further categorised into weak and strong [1, 67–71]. The important difference between weak and strong precipitate configurations is the distance (λ) between two precipitates along a dislocation line. λ of weak precipitates is longer than those in strong and non-shearable precipitate configurations because the dislocation bowing angle (Ψ) is large (dislocations do not bow much) at weak precipitates.
When an external shear stress (τ_{ex}) is imposed onto a small precipitate, a dislocation experiences reactive forces from the precipitates. Such force stems from two different effects, the anti-phase boundary energy and the coherency effects.

Anti-phase boundary effect

Once the dislocation shears an ordered particle, such as γ', an altered atomic arrangement, or anti-phase boundary (APB), is produced. In the case of γ', the dislocations cut the precipitate with two super-partial dislocations jointly passing through the particle: the first dislocation forms the APB and the second one removes it [1, 70]. For example, when a dislocation enters into $\{111\}$ planes of γ', they can be expressed as the following:

$$a/2\{111\}\langle 1\bar{1}0\rangle + \text{APB} + a/2\{111\}\langle 1\bar{1}0\rangle, \tag{2.30}$$

where a is the lattice parameter. This is because the shortest lattice vector of the matrix γ is $a/2$<110> whereas that of the matrix γ' is a<100>. The contribution of this planar fault on strengthening is quite large in γ' strengthened alloys.
The forces balance on the first and second dislocations (Fig. 2.13): the Peach–Koehler force from the applied shear stress $\tau_{\mathrm{ex}} b\lambda_i$ $(i = 1,2)$, the elastic repulsive force between the dislocations $F_{\mathrm{rep}}\lambda_i$ $(i = 1,2)$, the pinning force $E_{\mathrm{apb}} l_1$ and the force acting on the particle $2\tau_{\mathrm{ex}} br$, can be expressed as

$$\tau_{\mathrm{ex}} b\lambda_1 + F_{\mathrm{rep}}\lambda_1 - E_{\mathrm{apb}} l_1 + 2\tau_{\mathrm{ex}} br = 0 \tag{2.31}$$

and

$$\tau_{\mathrm{ex}} b\lambda_2 - F_{\mathrm{rep}}\lambda_2 = 0, \tag{2.32}$$

where τ_{ex} is the external applied shear stress, b is the magnitude of Burgers vector, $\lambda_{(1,2)}$ is the distance between two particles on the first and second dislocations, F_{rep} is the elastic repulsive force between coupled dislocations, E_{apb} is the anti-phase boundary energy and l_1 is a segment length of the leading dislocation [71]. By arranging the equations 2.31 and 2.32, the critical resolved shear stress (CRSS) is expressed as

$$\tau_{\mathrm{apb}} = \frac{E_{\mathrm{apb}} l_1}{2b(\lambda_1 + r)}, \tag{2.33}$$

where τ_{apb} the CRSS by the APB effect.

The effective distance of particles cut by the leading dislocation (λ_1) can be expressed by

$$\lambda_1 = \begin{cases} \lambda_s & (\lambda_{\mathrm{s}} \geq L - l_1, \mathrm{weakly-coupled}) \\ L - l_1 & (\mathrm{otherwise}, \mathrm{strongly-coupled}) \end{cases} \tag{2.34}$$

where λ_{s} is the Friedel spacing (mean particle distance on a straight dislocation) and L is a square lattice spacing (mean particle distance on a plane). Equation 2.34 indicates that the effective particle distance is represented by the mean particle distance on a straight dislocation when the particles are small and finely dispersed, whereas the effective distance can be modelled by the mean particle space on a plane when the particles are coarse. By considering a geometric configuration of the particles and dislocations [1, 71], λ_{s} and L are expressed as

$$\lambda_{\mathrm{s}} = \left(\frac{T_{\mathrm{dis}}}{E_{\mathrm{apb}} r} \right)^{1/2} L, \tag{2.35}$$

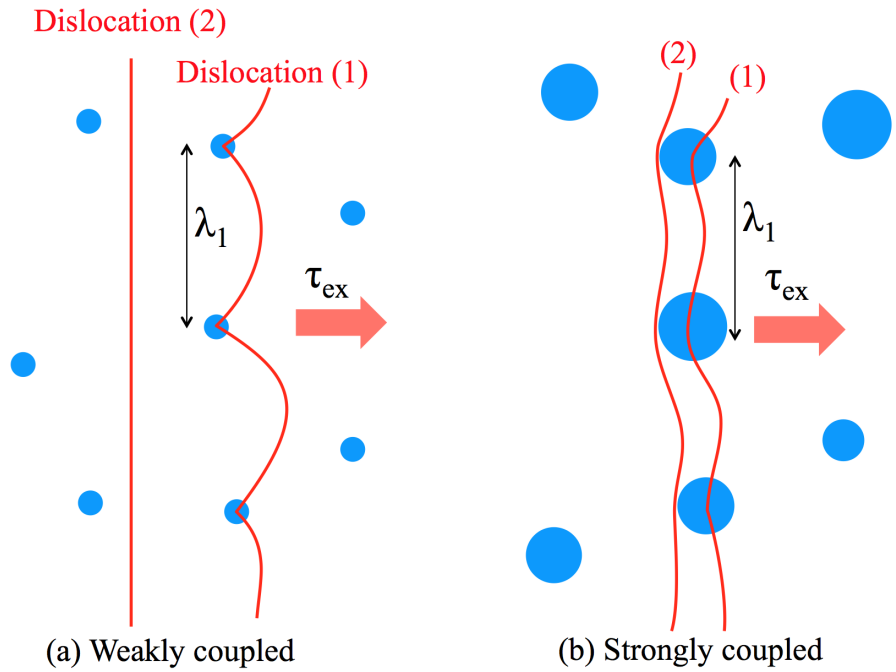

Fig. 2.13 Configuration of precipitate strengthening due to the formation of anti-phase boundary (a) weakly-coupled dislocations and (b) strongly-coupled dislocations.

$$L = \left(\frac{2\pi}{3f_{\mathrm{pr}}}\right)^{1/2} r, \tag{2.36}$$

where T_{dis} is the dislocation line tension and expressed by $1/2\mu b^2$ with the shear modulus μ, and f_{pr} is the fraction of the precipitate [67].
In addition, the segment length of the leading dislocation that shears the precipitate particle is expressed by

$$l_1 = \begin{cases} 2r & (r < r_{\mathrm{m}}, \mathrm{weakly-coupled}), \\ 2r(r^2 - (r - r_{\mathrm{m}})^2)^{1/2} & (\mathrm{otherwise}, \mathrm{strongly-coupled}). \end{cases} \tag{2.37}$$

The geometric configuration of l_1 when the particle size is large compared to the distance between the leading and the following dislocations is shown in Figure 2.14. Although the segment length is represented by the diameter of the particle when the particle is small, it is represented by the function of r_{m} $(1/2\mu b^2/E_{\mathrm{apb}})$ when the precipitate is large and partially sheared by the dislocation [71].

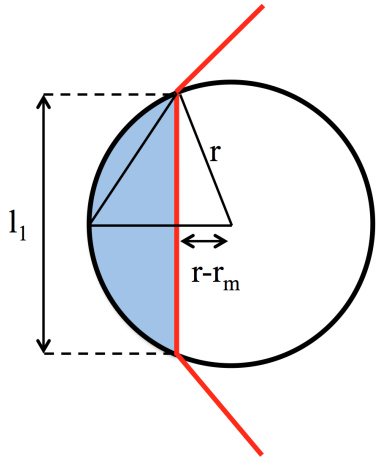

Fig. 2.14 Geometric configuration between l_1 (segment length of the leading dislocation), r (mean particle radius) and r_m (particle radius with maximum strength) [71].

By using relationships described so far, τ_{apb} can be calculated by Equation 2.33 and variables r, f_{pr}, μ, b and E_{apb}. Here, E_{apb} (anti-phase boundary energy) depends on the chemical composition of the precipitate. Fig. 2.15 shows the change in E_{apb} on the $\{111\}$ plane when Al in the γ' is substituted by other elements, such as Ti and Nb [72]. When the fraction of Ti and Nb in γ' increases by replacing Al, APB energy would substantially increase, which leads to an increase in alloy strength.

Coherency effect

Due to the lattice parameter misfit between the matrix and the precipitate, a strain field develops around the precipitate, which acts as a barrier for dislocation motion. This effect should be considered for alloys containing γ''. The strengthening effect increases as the misfit becomes larger, which can be expressed as

$$\tau_{coh} = 1.7\mu\Delta\varepsilon^{1.5}\left(\frac{h^2 f_{\gamma''}(1-\beta)}{2bl}\right)^{0.5}, \tag{2.38}$$

where τ_{coh} is critical resolved shear stress by coherency effect, μ is shear modulus, $\Delta\varepsilon$ is strain misfit, h and l are the height and length of disc-shaped precipitates, $f_{\gamma''}$ is the volume fraction of γ'' and β is the fraction of particles whose c axis (the longitudinal axis in Figure 2.1 (b)) is normal to the Burgers vector [73].

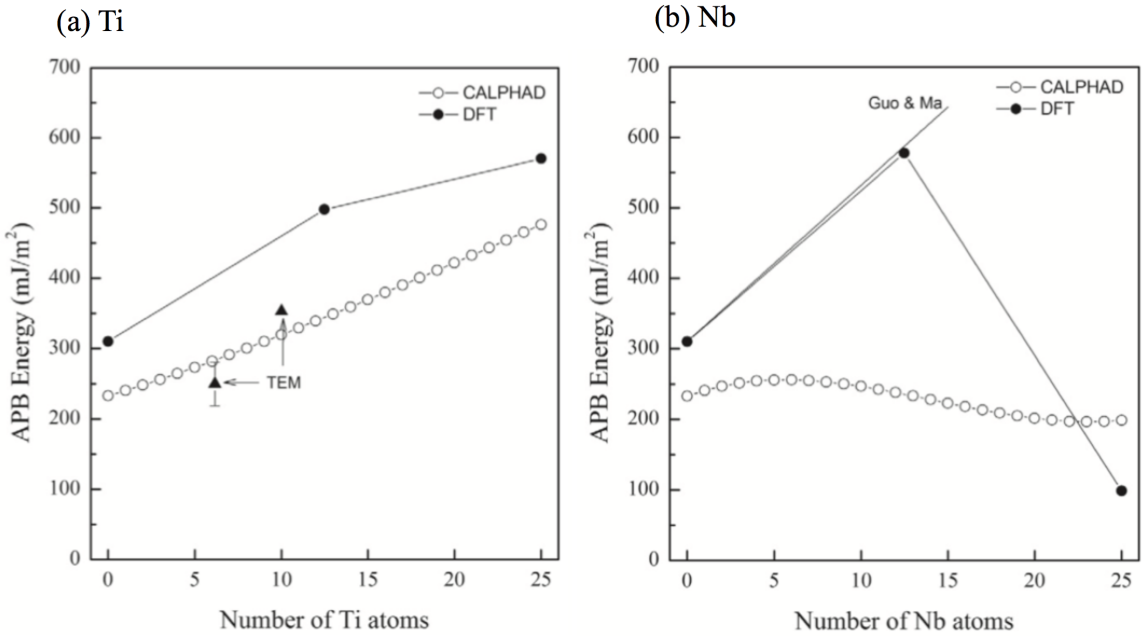

Fig. 2.15 The change in APB energy on the $\{111\}$ plane when (a) Ti or (b) Nb substitutes Al in the γ' phase. Adapted from Crudden *et al.* [72].

2.3.2 Non-shearable precipitates

If precipitates are large and strong so that dislocations are not able to cut them but only bypass them, those precipitates are called non-shearable. When a dislocation is about to pass a precipitate, the dislocation must have a high enough force to overcome the resistance from the precipitate (F_{m}). Several models for describing the bypass mechanism have been proposed after Orowan's original work [68]. In this study, a recent formulation by Galindo *et al.* [71], which was expressed by the following equation was employed.

$$\tau_{\mathrm{oro}} = \frac{3\mu b}{2L}. \tag{2.39}$$

In the equation, τ_{oro} is the increase in the shear stress by non-shearable precipitates [71].

2.3.3 Competition between dislocation - precipitate interactions

Strengthening effects from several precipitates have been introduced. When an alloy is deformed under an external shear stress, the dislocations in the material move through the minimum energy path. In other words, the effect which has the smallest barrier for the

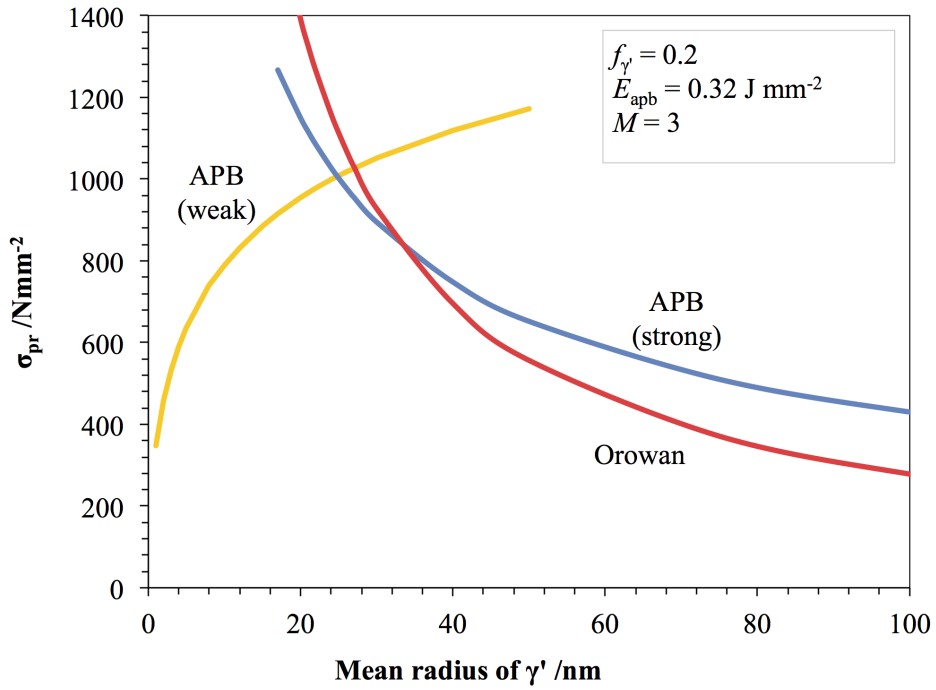

Fig. 2.16 Competition of 3 different strengthening effects: APB effect (weakly coupled), APB effect (strongly coupled) and Orowan effect). $f_{\gamma'}$ and E_{apb} are the volume fraction and anti-phase boundary energy of γ' and M is Taylor factor.

dislocation movement would prevail. For example, if the CRSS estimated by APB effects is smaller than that estimated by Orowan's bypass mechanism, the dislocation would move by cutting the particles.

Figure 2.16 presents an example of calculated precipitation strengthening. During the underaged condition, at which the precipitates are small, two dislocations are weakly coupled when cutting γ' and the strengthening is dominated by APB effects. When the precipitates have grown, the dislocations are strongly coupled when they pass the precipitates. Once precipitates have coarsened to; for example when larger than 40 nm, the dislocation cannot cut the particle any more and the Orowan effect becomes the dominant strengthening mechanism. So, the effect transits as the size of precipitates increases.

In some alloys, several different species of precipitates are dispersed in the matrix and contribute to alloy strengthening. For example, it is highly predictable that a Ni-based alloy with high Nb and Al contents would be strengthened by both γ' and γ''. Several studies on the combined effects from different precipitates have been conducted [69, 74] and a

generalised equation can be expressed as

$$\sigma_{\mathrm{pr}}^{q} = \sum_{m=1}^{n} \sigma_{\mathrm{pr},m}^{q} \tag{2.40}$$

where q is an exponent and $\sigma_{\mathrm{pr},m}$ is the strengthening from the precipitate species m. q varies from 1 to 2 depending on the precipitate character but putting 2 for q (Pythagorean superposition) is reported to give a good agreement with experimental results [75, 76].

2.4 Other strengthening mechanisms

2.4.1 Solid solution strengthening

Solid solution strengthening is one of the most common strengthening mechanisms for advanced alloys. Several theoretical explanations to describe this mechanism have been proposed. According to Fleischer, the elastic interactions between the substitutional impurity atoms and dislocations result in hardening due to the difference in moduli and size of the substituted atom and the surroundings [77].
According to his model, solid solution strengthening by the solute element i in a binary alloy can be calculated by the fraction of the element (c_i) and the coefficient (k_{fl}) as follows:

$$\sigma_{\mathrm{fl},i} = k_{\mathrm{fl}} c_i^{1/2}, \tag{2.41}$$

where the coefficient k_{fl} is given by a combination of two effects: modulus and atomic size misfits as

$$k_{\mathrm{fl}} = \frac{3}{2}\mu \left(|\eta_i'| + \alpha|\delta_i|\right)^{3/2}. \tag{2.42}$$

Here, η_i' and δ_i account for the modulus and atomic size misfits, respectively, and α is a constant. η_i' and δ_i can be broken down into

$$\eta_i' = \frac{\eta_i}{1+0.5|\eta_i|}, \tag{2.43}$$

$$\eta_i = \frac{d\mu}{dc_i}\frac{1}{\mu}, \tag{2.44}$$

$$\delta_i = \frac{da}{dc_i}\frac{1}{a}, \tag{2.45}$$

by the shear modulus (μ) and the cell parameter (a) of the alloy.
Labusch extended this theory by considering several solute atoms interacting with the dislocation rather than a process in which the dislocation is blocked by a single atom [78]. Based on his statistical study, the solid solution strengthening is described as:

$$\sigma_{\mathrm{lb},i} = k_{\mathrm{lb}} c_i^{2/3}, \tag{2.46}$$

$$k_{\mathrm{lb}} = \frac{3}{2}\mu \left(\eta_i'^2 + \alpha^2 \delta_i^2\right)^{4/3}. \tag{2.47}$$

The equation he proposed was similar to that by Fleischer's model, but the exponent value n in Labusch's is 2/3. In our study, Labusch's approach is taken as his theory can apply to alloys with a higher concentration of solute atoms than Fleisher's.

Both Fleisher's and Labusch's models were developed for binary alloys and Gypen and Deruyttrere have expanded these models to a multicomponent system [79, 80]. Later, Roth *et al.* validated Gypen and Deruttrere's model with the yield stress of multi-component Ni-based solid solution alloys [79–81] and concluded that the superposition of solid solution strengthening by each element in a multicomponent system (σ_{ss}) is expressed by coefficient q,

$$\sigma_{ss} = \left\{ \sum_i \left(k_{ss,i}^{1/q} c_i \right) \right\}^q . \tag{2.48}$$

In this study, the equation 2.48 was employed with a slight modification considering the volume fraction of the matrix. Further details on how the equation was implemented in the alloy design process will be presented in the next chapter.

2.4.2 Grain boundary strengthening

Grain boundary strengthening (grain boundary hardening) has been paid much attention by metallurgists because not only the yield strength but also toughness can be increased by this strengthening mechanism. The influence of grain size in polycrystalline metals on their properties was originally pointed out in the 1950s by Hall and Petch, which is now widely known as the Hall-Petch relationship [82, 83].
According to the Hall-Petch relationship, the influence of grain size on the strength of alloys, σ_{gb} is expressed as a function of grain size of the matrix by Equation 2.49:

$$\sigma_{gb} = \sigma_0 + k_{gb} D_{gr}^{-0.5} \tag{2.49}$$

where σ_0 is the lattice friction stress, k_{gb} is a coefficient and D_{gr} is the mean grain diameter. Although this relationship was established empirically, several theoretical models have also been proposed.

- **Dislocation pile-up model**: This model is based on an idea that grain boundaries behave like barriers that impede dislocation motion. After dislocations are generated from a Frank-Read source, they pile up at the grain boundaries. The stress at the tip of

Table 2.4 Coefficients for grain boundary strengthening of Ni- and Fe-based alloys.

Materials	Phases	σ_0 /MPa	k_{gb} /MPa $\mu m^{-0.5}$	Remark	Ref.
pure Ni	γ	21.8	158	d=0.12-130 μm	[93]
pure Ni	γ	25-35	40-200	depend on S content	[87]
Ni alloys	$\gamma + \gamma'$		450		[91]
Ni alloys	$\gamma + \gamma'$		750		[90]
Ni alloys	$\gamma + \gamma'$		500-1500	low amount of γ'	[94]
Ni alloys	$\gamma + \gamma'$		400	high amount of γ'	[94]
α steels	α	371	685	made by ball-milling	[88]
α steels	α	100	600		[92]
γ stainless steels	γ	100	600		[92]
γ stainless steels	γ	60-100	300-510	Interstitial free	[89]
γ stainless steels	γ	145	537	High N	[89]

this dislocation pileup must exceed a critical value so that the dislocation overcomes the grain boundary. This stress can be described with the number of pileup dislocations along the slip plane, which is usually limited by the size of the grain [84]. Although this concept explains the grain size dependency of the stress, direct evidence of pileup dislocations has not been observed in some alloys, despite the fact that the Hall-Petch relation seems to be applicable to most alloys [85].

- **Grain boundary source model**: This model, originally proposed by Li [85] assumes the grain boundaries behave as a source of dislocations. Therefore, the dislocation density depends on the surface area and volume of the grains. After the dislocations are emitted from the grain boundaries, they immediately interact with each other, which leads to strengthening. Some direct observations of the dislocations emitted from the grain boundary are reported by Tsuchiyama *et al.* [86].

Coefficients for the Hall-Petch relation of both Ni- and Fe-based alloys have been proposed by many researchers [87–94], which is summarised in Table 2.4.
Figure 2.17 shows a relation between the increment of strengthening and the mean diameter of grains. For plotting these curves, 20 MPa and 750 MPa $\mu m^{-0.5}$ were employed as σ_0 and k_{gb} for Ni-based alloys and 100 MPa and 600 MPa $\mu m^{-0.5}$ were used as σ_0 and k_{gb} for Fe-based alloys. If the mean grain diameter is 30 μm, which is a typical size for the alloys studied in this project, the strength increment by grain boundary strengthening mechanism would be 160 and 210 MPa for Ni- and Fe- based alloys, respectively.

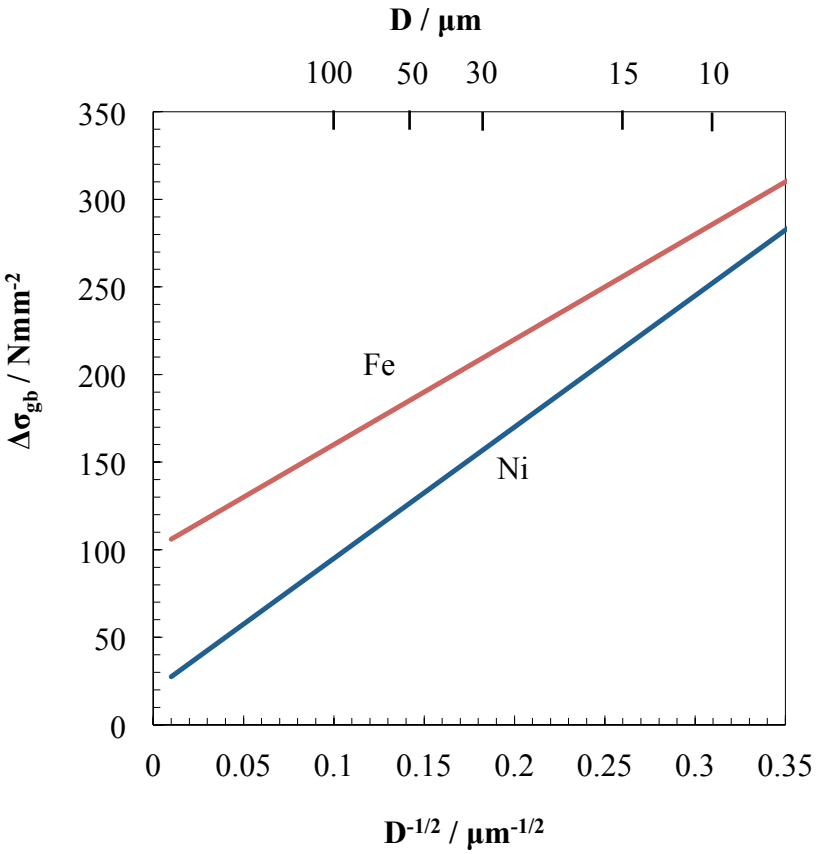

Fig. 2.17 Relationship between strengthening increment and mean grain size of Ni- and Fe-based alloys.

2.4.3 Dislocation strengthening

Dislocations play an important role in the plastic deformation of alloys. They can also act as an obstacle for other dislocations, which leads to the increase in the resistance force for deformation. This mechanism is called dislocation strengthening or work hardening. According to the Bailey and Hirsch's work, the increment of the strength by the dislocation forest is given by

$$\sigma_{\mathrm{dis}} = \sigma_0 + k_{\mathrm{dis}} G b \rho^{0.5} \tag{2.50}$$

where σ_0 and k_{dis} are constants and ρ is the dislocation density [95].

2.5 Summary

In this chapter, general knowledge of high-temperature alloys is reviewed with a focus on microstructural evolution and strengthening mechanisms. In the microstructure evolution of alloys featured in this study, precipitation and coarsening of γ' are of great importance as the precipitate has a large impact on the alloy strength. Although the microstructure of high-temperature alloys is complicated, many theoretical models that can describe the evolution of microstructure have been proposed by researchers. These models can be used for predicting microstructure parameters, such as precipitate volume and size. This chapter also contains a brief review of classical strengthening theories on precipitation, solid solution, grain boundary and dislocation strengthening. Precipitation strengthening is particularly important due to its influence on high-temperature alloy strength. Understanding the microstructures, combined with classical strengthening theories, can lead to alloy strength prediction, which is one of the essential parts in the present study.

Chapter 3

Strategy for alloy design

This chapter describes the alloy design strategy employed in the present study. In the present approach, several calculations were combined to circumvent the limitations of the experiment-based trial and error approaches. First, microstructural evolution during heat treatment and service at high temperatures was predicted by kinetic calculations as well as by considering thermodynamic equilibrium states. Then, the yield strength after heat treatment and service was estimated from the calculated microstructural parameters adopting classical strengthening theories. Based upon these calculations, the chemical composition of the alloy was optimised with a genetic algorithm (GA), a nature-inspired optimisation tool. In the following sections, computer-aided alloy design approaches are briefly reviewed and the optimisation process using the GA is explained. Then, the prediction of microstructural parameters and alloy properties is validated with experimental values taken from literature.

3.1 Alloy design using a genetic algorithm

3.1.1 Computer-aided alloy design

Many computer-aided alloy design approaches, sometimes referred to as Integrated Computational Materials Engineering (ICME) approaches, have been studied for decades [96–106]. The aim of employing such approaches is basically to reduce the cost and time for an alloy development. Most of them consist of two parts: prediction and optimisation. For predicting material's features, such as microstructural parameters and properties, from alloy compositions and processing parameters, empirical regression models are still widely used. Thermodynamics, physical based model and classical strengthening theories are also incorpo-

rated for predicting in several studies. In recent years Neural Network (NN) approaches for predicting alloy properties have been paid more and more attention. In NNs, input parameters are transformed into the final output values through one or several hidden layers. NNs have been recognised as a strong prediction tool for alloy design [107]. However, there are disadvantages in NNs. For example, the NNs-based approach requires a large database (usually prepared from pre-existing materials data) for training. In addition, the prediction process is not necessarily understandable for an operator (human), as the relationship between the input and output does not depend on theoretical knowledge of Materials Science. Therefore, in the present study, the prediction process was carried out by a combination of thermodynamics, kinetic calculations and classical strengthening theories. The advantage of this approach is that one can check and confirm the uncertainties of the calculation by validating the microstructure and mechanical properties and comparing them with the calculations. The recent progress in the understanding of the thermodynamics and kinetics in metallurgy, as well as the development of reliable strengthening models, has also encouraged the use of the present approach.

As for the optimisation part of the alloy design, the GAs were employed in the present work. As summarised in Table 3.1, the GA has been used as an optimisation tool for alloy design by many researchers. Details of this optimisation heuristic are described in the following section.

Table 3.1 Alloy design approaches using genetic algorithms (TD: Thermodynamics, CST: Classical strengthening theory, NN: Neural network, ERM: Empirical regression model, GA: Genetic algorithm, MOGA: multi-objective genetic algorithm, GP: Genetic programme, SA: Simulated annealing).

Materials	Optimised parameters	Objectives	Prediction model	Optimisation	Reference
Al alloy	Microstructural parameters	Low/high temp. strength, ductility	CST	GA	[100]
Steel	Composition, process parameters	UTS, EL	NN	MOGA	[101]
Steel	Composition,	Hardness, cost	ERM	GA	[103]
Steel	Composition, process parameters	YS, EL, work-hardening rate	ERM	GA	[99]
Stainless steel	Composition,	Number of precipitates	TD, driving force	GA	[104]
Steel	Composition, process parameters .	YS, UTS, EL	NN	MOGA	[108]
Stainless steel	Composition, process parameters	Precipitation strengthening	TD	GA	[105]
Maraging steel	Composition, process parameters	Precipitation strengthening	TD, CST	GA	[106]
Steel	Processing parameters	YS, UTS, EL	NN	MOGA	[102]
Al alloy	Composition, process parameters	YS, UTS, EL	NN	MOGA	[97]
Ni-base superalloy	Composition	YS	Gaussian	MOGA	[109]
Ni-base superalloy	Composition	Fatigue life, YS, UTS, etc.	NN	SA	[96]
Al alloy	Composition, process parameters	YS, UTS, EL	ERM	GP, MOGA	[98]

3.1.2 Genetic algorithm

In this study, an optimisation technique was employed for obtaining the best chemical composition due to the large solution space for the problem. Considering ten different elements are chosen to be optimised and the concentration of each is divided into 16 different values, the combination of the chemical composition of an alloy is as many as 16^9, which means 6.9×10^{10} different alloys are in the solution space. Assuming that each strength estimation calculation is performed in one second, searching the best composition by calculating all combinations would need more than 2000 years. It is, therefore, essential to employ an efficient optimisation algorithm. In this study, the GA was employed as the optimisation heuristic. The GA has been developed, inspired by the theory of evolution, or natural selection process, and is now one of the most common optimisation heuristics used in many fields including materials science [110–112].

As described in the first chapter, an empirical trial and error approach usually leads to failure due to the inherent difficulties in developing high-temperature alloys, such as a large search space and complex microstructures. In this study, calculations were adopted in an integrated alloy design approach. In a basic GA procedure, a set of individual candidate alloys, chromosomes, is randomly input in the first step. The number of chromosomes (population size) in the set (generation) should be carefully chosen depending on the problem to be solved, but it is typically in the range between 50 and 1000. Each chromosome is expressed by a string of genes with either a binary (A = [1, 0, 1, 0, 1, ...]) or stepped-value (B = [1, 5, 10, 2, 5, 11, ...]) expression. In either case, the chromosome is created by encoding the original input parameters, which can be exemplified by chemical composition of the alloy in the present study. Based on certain criteria, a fitness value for each chromosome is calculated and those who have a higher fitness have a higher probability to be passed down to the next generation. In the present work, the yield stress of the alloy after certain heat treatment or thermal exposure was adopted as the fitness parameter. When the fitness of the chromosome reaches the aimed value, the number of iterations reaches a certain condition or the progress of the fitness value is saturated, the optimisation process will end and the chromosome with the highest fitness in the last generation is decoded into the original variables, such as chemical compositions. Unless they do not satisfy any finishing criteria, the set of chromosomes, or the generation, is sent to the next step. The chromosomes in a generation are ordered by their fitness and some of them are selected to be passed down to the next generation while others are removed. Although there are several ways to pass down the chromosomes, the one with higher fitness should be more likely to survive. When they are passed down, three operations: crossover,

mutation and elitism are performed, which are illustrated in Fig. 3.1 and explained as follows;

- Crossover
  A new chromosome is produced by a crossover of two parent chromosomes. For example, if the gene strings of the parents are expressed as A1 = [44444] and A2 = [22222], the new chromosome can be A3 = [22424], where the third and fifth genes are inherited from A1 and the rest are from A2.
- Mutation
  Mutation is a process in which one or more elements in a chromosome change randomly. This step is essential for preventing a local optimum. In a computational simulation, the mutation can be undertaken by changing a gene at a certain position of the string from 0 to 1 or vice versa in a binary system or changing a gene to a different value in a stepped-value system.
- Elitism
  Elitism promotes a chromosome with the highest fitness value in a generation to be passed down to the next generation without either mutation or crossover. Elitism preserves the best solution in all generations developed so far. In other words, the highest fitness value in a generation can become lower in the next generation without this operation.

In this study, the GA approach was incorporated by Python for the alloy design. Each calculated alloy is evaluated by its yield strength after an ageing heat treatment that simulates the service. Then, the yield strength is employed as the fitness value and a set of input parameters, the chemical composition of the alloy, is optimised for obtaining the highest fitness value.

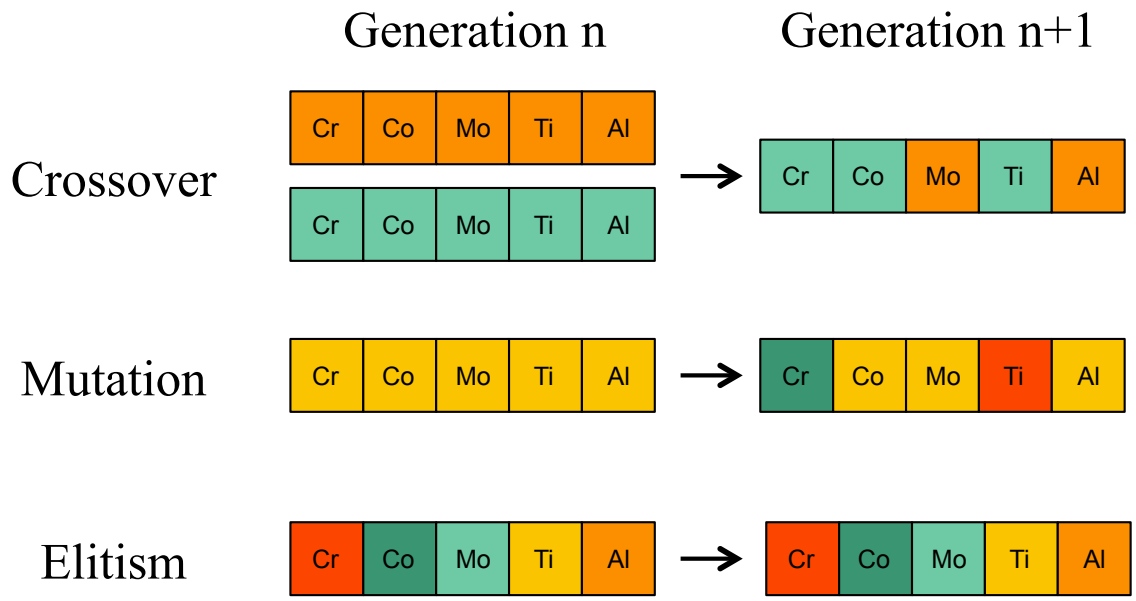

Fig. 3.1 Schematic illustrations that explain crossover, mutation and elitism in a genetic algorithm.

3.2 Overall strategy

Figure 3.2 shows an outline of the overall procedure for alloy design carried out in this study. The design procedure can be divided into five steps as follows:

1. Input parameters definition
2. Constraint calculation (elemental costs and manufacturability)
3. Microstructure prediction by kinetic calculation
4. Yield strength evaluation
5. Composition optimisation

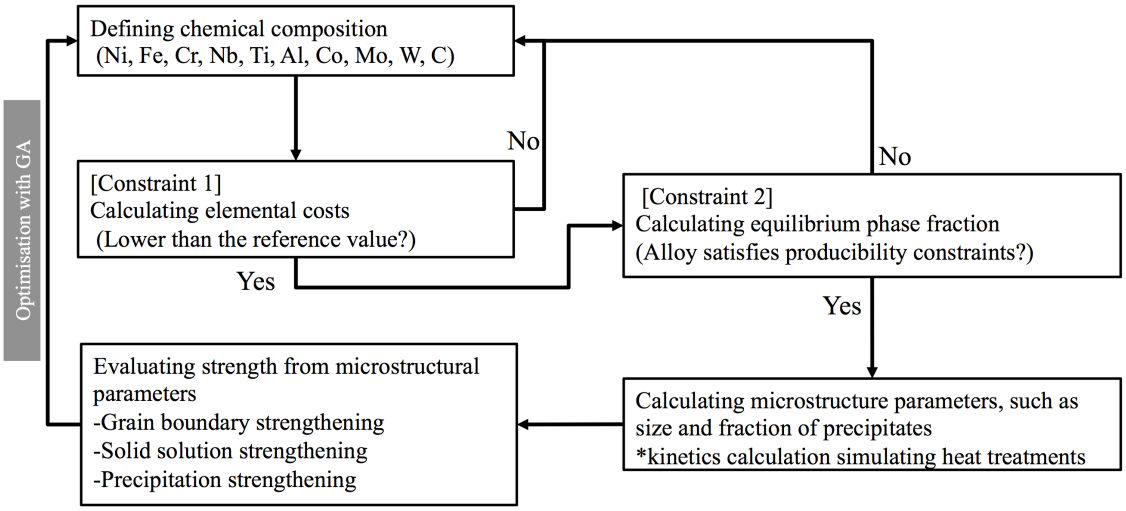

Fig. 3.2 Overall procedure for alloy design.

3.2.1 Input parameters definition

As the first step of the alloy design, the chemical compositions of candidate alloys were input as design parameters. In this work, Ni, Fe, Cr, W, Nb, Al, Ti, Mo, Co and C were considered. Elements sometimes added in high-temperature alloys, such as V, Mn, Si and B were ignored for the sake of calculation speed. The upper and lower limits of the concentration of each element, which is listed in Table 3.2, has been fixed based on the industrial and technical possibility to fabricate the alloy as well as for calculation efficiency. The lower limit of Ni is

Table 3.2 Maximum and minimum amount of each element employed for optimisation (mass%).

	Ni	Fe	Cr	Nb	Mo	Ti	Al	Co	W	C
MAX	Bal.	60	25	5	5	5	5	10	5	0.01
MIN	20	40	10	0.001	0.001	0.001	0.001	0.001	0.001	0.001

set so that the potential alloy can be strengthened by γ' or γ''. For reducing the elemental costs, the alloy is designed to contain Fe at least 40 %. The lower limit of Cr is settled to guarantee decent corrosion resistance in high-temperature environments.

3.2.2 Constraint calculation (elemental costs and manufacturability)

Costs and manufacturability constraints were considered in the design process. A cost index (I_{cost}) was defined and calculated from the chemical composition of the alloy by the following equation;

$$I_{\mathrm{cost}} = \sum_i p_{\mathrm{i}} \cdot c_{\mathrm{i}}, \tag{3.1}$$

where p_{i} is the price of the element i in US dollars per kilogram ($\$\cdot\mathrm{kg}^{-1}$) and c_{i} (mass%) is the concentration of i in the alloy. p_{i} was taken from the industrial raw material price (2010-2014 average) [113], which is shown in Figure 3.3. As shown in the figure, Ni, Nb, Co, Mo and W are expensive elements although they are known to have a beneficial influence on high-temperature properties. I_{cost} of common high-temperature alloys is summarised in Table 3.3. This study aims to develop an economical alloy whose cost index is lower than conventional high-temperature alloys, such as Alloy 718. Although production cost is not considered in the cost index, the value provides a reasonable index for understanding and comparing the material prices as far as the materials are produced by the similar cast and wrought processes.

Several other important constraints are considered for guaranteeing the manufacturability of the alloy. The designed alloy will be hot forged and hot rolled in a mass-production process and the alloy should have a wide processing production window. These constraints were implemented in our optimisation model by limiting the volume fraction of several phases estimated by a thermodynamic equilibrium calculation. In this study, the following constraints were employed;

$$f_{\mathrm{liq}} = 0 \quad (\mathrm{at}\,1200\,^{\circ}\mathrm{C}), \tag{3.2}$$

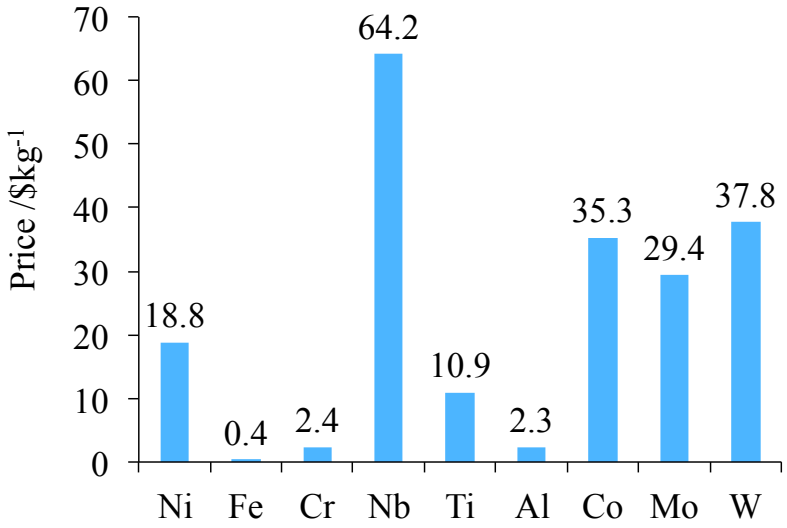

Fig. 3.3 Price of raw material averaged over 2010 to 2014 [113].

Table 3.3 Nominal chemical composition of the common high-temperature alloys in mass% and their cost index (I_{cost}).

($\$\cdot kg^{-1}$)	Ni (18.8)	Fe (0.4)	Cr (2.4)	Nb (41.7)	Ti (10.9)	Al (2.3)	Co (35.3)	Mo (29.4)	W (37.8)	I_{cost}
Alloy 718Plus	52	10	18	5.4	0.7	1.5	9	2.8	1	18.1
Waspaloy	59		19		1.3	3	13	4.3		17.7
Alloy 718	51	20	20	5	0.9	0.5		3		13.1
Incoloy 800	33	45	21		0.4	0.4				6.9
Alloy 660	25	57	15		2	0.25		1.2		5.8
AISI 310S	20	55	25							4.6

and

$$f_\mu, f_\sigma, f_\eta, f_\delta \leq 0.01 \quad (\text{at}\,1000\,^\circ\text{C}), \tag{3.3}$$

where f denotes the volume fraction of each phase in equilibrium. The first criterion is implemented as it is impossible to forge or hot roll a material if it contains a liquid phase due to the so-called liquid metal embrittlement. Considering practical hot forging and rolling conditions, the solidus temperature of the designed alloy should be restricted to 1200 °C or higher [114]. Condition 3.3 stems from the fact that hot forming would be difficult if the alloy contains a high volume fraction of secondary phases as these phases would potentially cause cracks. Equilibrium calculations are conducted by a thermokinetic simulation software, MatCalc, whose details are described in the next section.

3.2.3 Microstructure prediction by MatCalc

Once a candidate alloy satisfied the constraints described above, the input parameters (alloy chemical compositions) are used for the microstructure evolution kinetic calculation. The microstructure parameters considered are summarised in Table 3.4. These parameters are calculated with MatCalc, which is a multicomponent-multiphase phase kinetics simulation software [58, 59]. Table 3.5 shows a comparison of phase transformation simulation software used in modern metallurgy [53]. MatCalc employs classical nucleation theory and SFFK model for describing precipitation nucleation and its evolution, respectively. These models are incorporated by the KWN model in the software. Figure 3.4 shows a schematic illustration of the time integration of the precipitate evolution equations implemented in the software [53]. As for the time integration procedure of the precipitate evolution, the time is discretised into a small isothermal increment. In each time step, the nucleation, evolution and dissolution of the precipitates are calculated and the number, radius and chemical composition of the precipitate classes (precipitates with the same radius and chemical composition are contained in each precipitate class) are updated.
A feature standing out in MatCalc is that it calculates the interfacial energy from chemical compositions of the alloy based on the generalised nearest neighbour broken bond (GBB) model [115] and displays high computational efficiency for multicomponent-multiphase calculations. Additionally, the software can be linked to other software packages or programming languages (Python was employed in this study), which is also a very important feature as this study aims to integrate the calculated microstructural parameters into an optimisation programme.

Table 3.4 Microstructural parameters related to strength estimation.

strengthening mechanism	microstructural parameters
precipitation	precipitate size, volume, shape factor
grain boundary	grain size
solid solution	matrix chemical composition
forest	dislocation density

Six phases were incorporated in microstructural calculations, an FCC matrix, γ', γ'', η, δ and $M_{23}C_6$, where γ', γ'' were especially important for alloy strength. In the calculation, γ'

[1] classical nucleation theory
[2] Svoboda - Fischer - Fratzl - Kozeschnik model
[3] Kampmann-Wagner numerical model
[4] generalised nearest neighbour broken bond model

Table 3.5 Comparison of phase transformation simulation software [53].

Software (Developer)	MatCalc (E. Kozeschnik)	Dictra (Thermo-Calc Software)	Precipicalc (QuesTek Innovations)	TC-PRISMA (Thermo-Calc Software)
Nucleation	CNT[1]	-	CNT	CNT
Evolution equations	SFFK[2]	Moving boundary	Mean field	Moving boundary
Numerical model	KWN[3]	-	KWN	KWN
Interfacial energy	GBB[4]	-	-	GBB

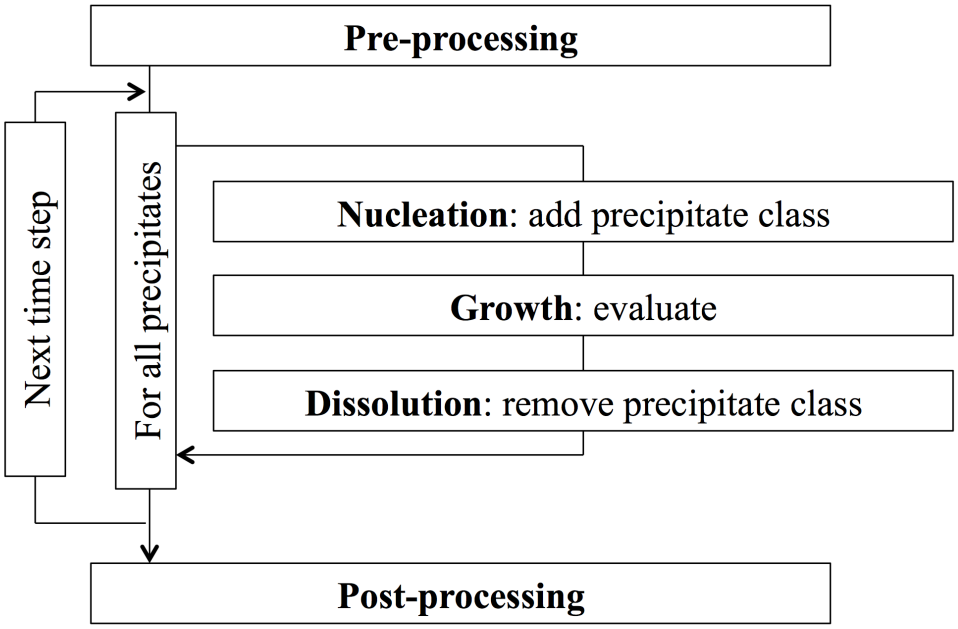

Fig. 3.4 Time integration of the evolution equations implemented in MatCalc [53].

was assumed to be spherical whereas γ'' was assumed to be disc-shaped and a shape factor (F_{shape}) of γ'' was considered. The shape factor was defined as the ratio of the thickness to the length of the precipitate as shown in Figure 3.5.

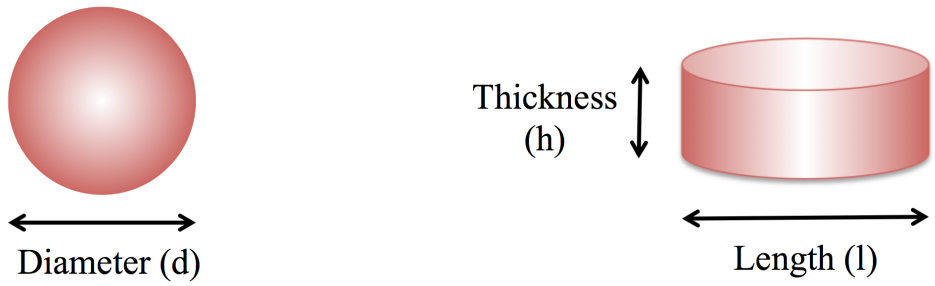

(a) Spherical (F_{shape}=1) (b) Disc shaped (F_{shape} = h/l)

Fig. 3.5 Schematic illustration of spherical and disc-shaped precipitates and their shape factor (F_{shape}).

Figure 3.6 shows the shape factor of γ'' in several Ni-based superalloys collected from literature [21, 23, 38, 116–118]. An empirical parabolic relationship between the shape factor and the particle length was obtained and the influence of the chemical composition of the alloy on the shape factor was small.

In the MatCalc calculation, the size of precipitates is calculated under the assumption that they are spherical. In this study, the influence of the shape factor was considered by using the empirical parabolic equation derived from Figure 3.6, which is expressed as

$$F_{\text{shape}} = \omega_1 r^{\omega_2}, \tag{3.4}$$

where the coefficients ω_1 and ω_2 were 1.17 and -0.473, respectively, which was estimated by curve fitting (the least square method). As shown in the line in Figure 3.6, Equation 3.4 can reasonably describe the trend of the F_{shape}. In the microstructure prediction, the F_{shape} was calculated as a function of the volume fraction of the precipitate.

3.2.4 Yield strength estimation

The yield strength at room temperature after a certain heat treatment is estimated from the microstructural parameters kinetically calculated by MatCalc. As shown in the equation below, the strength (σ_{ys}) was estimated by the summation of three strengthening mechanisms:

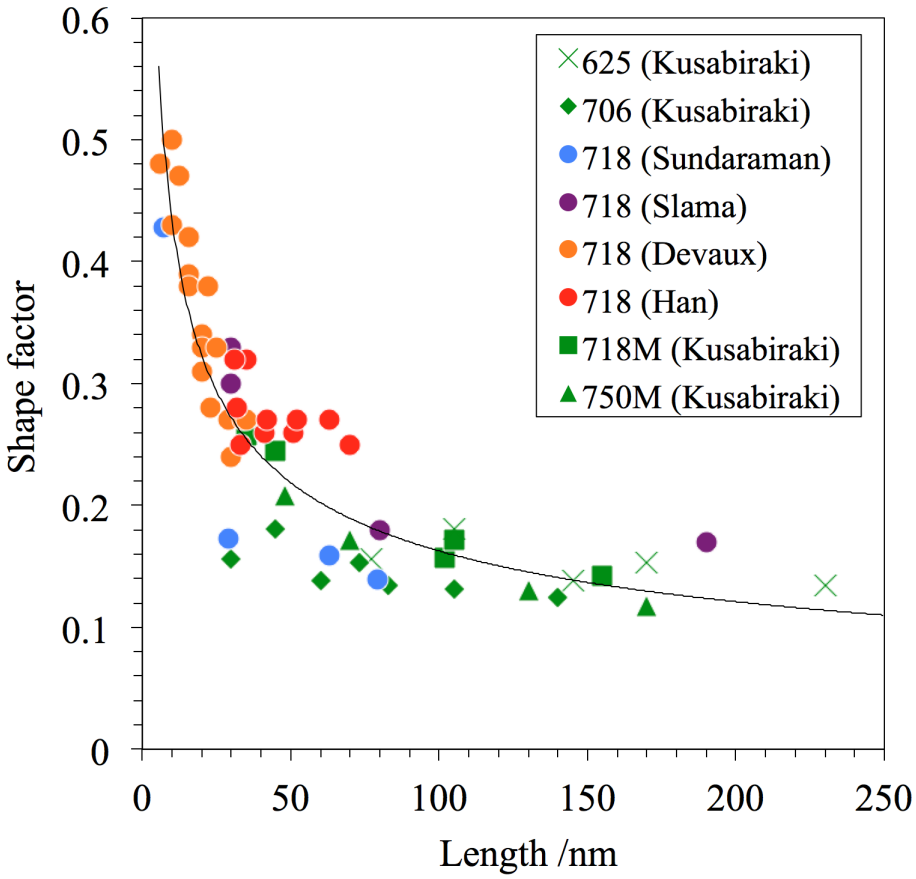

Fig. 3.6 Shape factor of γ'' in superalloys [21, 23, 38, 116–118]. The curve line in the figure represents an empirical parabolic equation expressed by Equation 3.4.

grain boundary (σ_{gb}), solid solution (σ_{ss}) and precipitation strengthening (σ_{pr}):

$$\sigma_{ys} = \sigma_{gb} + \sigma_{ss} + \sigma_{pr}. \tag{3.5}$$

Some hardening parameters were neglected for computational efficiency, which included the dislocation strengthening because the alloys considered being fully solutionised and the dislocation density was low. Additionally, the mean grain size was assumed to be constant during ageing and service as it was not supposed to change significantly after solutionising. Grain boundary strengthening was estimated from the Hall-Petch relationship:

$$\sigma_{gb} = \sigma_0 + k_{gb} D_{gr}^{-0.5}, \tag{3.6}$$

where σ_0 is the friction stress or lattice stress, k_{gb} is the Hall-Petch coefficient and D_{gr} is the mean grain diameter [82, 83]. σ_0 and k_{gb} adopted in this study were 100 MPa and 600 MPa

$\mu m^{-0.5}$, respectively [92].
Solid solution strengthening was estimated from a multi-component model developed by Gypen and Deruyttere, which was formulated as Equation 2.48. In this study, an additional term for the effect of the volume fraction of the matrix was incorporated,

$$\sigma_{ss} = f_{mat} \left\{ \sum_i k_{ss,i}^{3/2} c_{ss,i} \right\}^{2/3}, \tag{3.7}$$

where f_{mat} is the volume fraction of the matrix, $k_{ss,i}$ is the solid solution strengthening coefficient for element i and $c_{ss,i}$ is the concentration of element i in the matrix [79, 80]. $k_{ss,i}$ is calculated from moduli and atomic size misfits,

$$k_{ss,i} = \frac{3}{2}\mu \left(\eta_i'^2 + 16^2 \delta_i^2 \right)^{2/3}, \tag{3.8}$$

where, η_i' and δ_i are the modulus and atomic size misfits with respect to Fe, respectively. In the present study, they are calculated as follows,

$$\eta_i' = \frac{\eta_i}{1 + 0.5|\eta_i|}, \tag{3.9}$$

$$\eta_i = \frac{\mu_{Fe} - \mu_i}{\mu_{Fe}}, \tag{3.10}$$

$$\delta_i = \frac{a_{Fe} - a_i}{a_{Fe}}, \tag{3.11}$$

where μ_{Fe} and μ_i are the shear modulus of Fe and the solid solution element i, and a_{Fe} and a_i are the atomic size of Fe and the solid solution element i, respectively.
Table 3.6 shows the values of $k_{ss,i}$ used in this study. The coefficients $k_{ss,i}$ of substitutional elements were calculated from Equations (3.9), (3.10), (3.11) using the elemental shear modulus and atomic size [119, 120], while the carbon coefficient was taken from literature [121].

As described in the previous chapter, strengthening precipitates can be divided into two categories: shearable and non-shearable particles. For strengthening by shearable γ' particles, the increment of critical resolved shear stress was calculated by Equation 2.33. The main parameters used for the calculation were the volume fraction of the matrix and the precipitates, the mean radius of the precipitates, and the anti-phase boundary energy. The

Table 3.6 Atomic radii, shear moduli and coefficient for solid solution strengthening $k_{ss,i}$ [119–121].

i	Fe	Ni	Co	Cr	Mo	Al	Ti	W	Nb	C
a_i /nm	0.124	0.117	0.118	0.13	0.146	0.124	0.148	0.15	0.156	-
μ_i / MPa	80	80	75	115	126	26	44	161	38	-
$k_{ss,i}$ / MPa	0	112	90	102	637	43	720	826	1106	1984

increment is linear to the anti-phase boundary energy E_{apb}, which depends on the chemical composition of γ' [72]. In this study, the influence of the chemical composition of γ' on E_{apb} is incorporated by the equation below.

$$E_{\mathrm{apb}} = E_{\mathrm{apb},0} + \sum_i \Delta E_{\mathrm{apb,i}}, \tag{3.12}$$

where $E_{\mathrm{apb},0}$ is the APB energy for Ni_3Al (0.240 $\mathrm{mJ{\cdot}m^{-2}}$), $\Delta E_{\mathrm{apb,i}}$ is the increment in the APB energy by element i. The increment of the APB energy was calculated based on the chemical composition of γ' by a third order polynomial derived from the data in [72]:

$$\Delta E_{\mathrm{apb,i}} = a_{1,i}x_i^3 + a_{2,i}x_i^2 + a_{3,i}x_i \tag{3.13}$$

where $a_{1,i}$, $a_{2,i}$ and $a_{3,i}$ are coefficients and x_i is the concentration of the solute i in γ' in at.%. The coefficients for Cr, Nb, Ti, Mo and W used in this study are shown in Table 3.7.

As the size of precipitates becomes larger, the particle turns from shearable to non-shearable,

Table 3.7 Coefficient for APB energy ($\mathrm{mJ{\cdot}m^{-2}}$) in Equation 3.13 [72].

	Cr	Nb	Ti	Mo	W
$a_{1,i}$	-0.0039	0.0254	-0.0028	0.0441	0.00552
$a_{2,i}$	-0.2468	-1.0747	0.1695	-2.5065	-2.2455
$a_{3,i}$	-2.6911	9.7279	7.2324	21.837	13.69

which leads the change in the strengthening mechanism from APB effect (γ') or coherency effect (γ'') into Orowan effect. In this study, both APB and Orowan effects for γ' and both coherency and Orowan effects for γ'' were calculated. The lower value of these two was employed as the dominating strengthening effect by γ' or γ''. The strengthening effect from other precipitates (η, δ and $M_{23}C_6$) was assumed to stem from Orowan mechanism as these precipitates were usually too large to be sheared by dislocations. The superposition of the strengthening from each precipitate was calculated by Pythagorean superposition as the following equation.

$$\sigma_{\mathrm{pr}}^2 = \sum_{m=1}^{n} \sigma_{\mathrm{pr},m}^2 \tag{3.14}$$

where $\sigma_{\mathrm{pr},m}$ was the strengthening from the precipitate species m.

3.3 Validation of calculations with literature

Before the optimisation work, microstructure and strength calculations conducted in this study were validated with experimental results taken from the literature.

3.3.1 Calculation

The main calculation parameters and conditions are summarised in Table 3.8. For microstructure calculation, MatCalc version 5.61 was used. The thermodynamics and mobility databases, mc_ni2.011.tdb and mc_ni_2.007.ddb were used, respectively. Ni, Fe, Cr, W, Nb, Al, Ti, Mo, Co and C were considered. In the kinetic calculation with MatCalc, six phases: the FCC matrix, γ', γ'', η, δ and $M_{23}C_6$ were considered. In the calculation, all phases except for the matrix were divided into multi-classes. In each class, the precipitates are the same in size and chemical compositions. If the number of classes is larger, a distribution of precipitates can be expressed smoothly, although it would take a longer time for the calculation to be completed. In this study, each phase was divided into ten classes by considering a balance between accuracy and efficiency of the calculation. The grain diameter was fixed to 20 μm, which is a typical size for many high-temperature alloys. The yield strength was calculated by the microstructure parameters obtained from MatCalc calculations.

Table 3.8 Parameters and conditions used for the microstructure and strength calculations.

For microstructure calculation	
Software	MatCalc ver. 5.61
Elements	Ni, Fe, Cr, W, Nb, Al, Ti, Mo, Co and C
Phases	matrix(FCC), γ', γ'', η, δ and $M_{23}C_6$
Thermodynamics DB	mc_ni2.011.tdb
Mobility DB	mc_ni_2.007.ddb
Number of particle size classes	10
Mean grain diameter / μm	20
Room temperature / °C	20

For estimating strength	
Taylor factor	2.6
k_{ss}	Table 3.6
σ_0 / MPa	100
k_{gb} / MPa·μm$^{-0.5}$	600
b / nm	$2.5 \cdot 10^{-10}$

3.3.2 Comparison between calculation and experiment

Calculations of microstructure and strength of several conventional alloys were performed and compared to experimental results in the literature for validating the accuracy of the calculations. Table 3.9 shows the chemical compositions and heat treatments of the alloys used for the validation [10, 20, 21, 23, 117, 122–126]. Alloy 625, Alloy 706, Alloy 718 and its derivatives, Alloy 718Plus, Alloy 939, Nimonic 105 and Waspaloy were used. As for the heat treatment conditions, when processing conditions (heating rate, holding temperature and time and cooling rate) were described in the literature, they were used in the calculation. For those without any description in the literature, 10 $^{\circ}C \cdot s^{-1}$ was employed for both the heating and cooling rate.

Figures 3.7 to 3.9 show a comparison between the calculated and measured microstructural parameters in several alloys with different heat treatments. Figure 3.7 explains that γ' fraction calculated by MatCalc agrees well with the experimental results in both Alloy 718Plus and Alloy 939. Judging from Figure 3.8, calculations for the size of γ' are also supported by the measurements with a wide range of sizes and alloys. Figure 3.9 shows that the measured size of γ'' is larger as the calculated value is larger, although the difference between experimental and calculated values is slightly larger than that in γ'. There is no certain tendency on the discrepancy of the relation between the calculation and experimental results.

Fig 3.10 shows a comparison between the calculated and experimental yield stress for several alloys. The agreement is not as good as with the microstructural parameters. However, considering that some heat treatment conditions used in the calculation were set by the author and parameters for estimating strength, such as the Taylor factor and the grain size, were fixed to a representative value for all calculations, the agreement between the calculations and experiments in the figure is regarded as acceptable.

Based on these results, it is concluded that the model and parameters employed in the calculation can be used for estimating microstructural parameters and strength of high-temperature alloys.

Table 3.9 Chemical composition of the alloys in weight percent and heat treatment condition used for model validation.

	Alloy	Ni	Fe	Cr	Nb	Mo	Ti	Al	C	B	Co	W	Ref
A	Alloy 625	60.6	4.66	21.51	4.01	8.54	0.28	0.15	0.02	-	0.01	-	[117]
B	Alloy 706	41.5	37.3	16.2	3.0	0.05	1.52	0.24	0.021	-	16.2	-	[124]
C	Alloy 718	53.4	18.0	18.3	5.45	2.97	0.92	0.59	0.037	-	0.13	-	[124]
D	Alloy 718	Bal	19.24	18.24	4.94	3.07	0.97	0.52	0.03	-	-	-	[23]
E	Alloyl 718	Bal	18.1	17.9	5.3	2.99	0.97	0.5	0.026	0.003	-	-	[21]
F	Alloy 718	Bal	16.33	18.39	5.43	2.93	0.076	0.074	0.048	0.0023	-	-	[20]
G	Alloy 718M	Bal	17.3	19	5.38	2.93	0.87	0.6	0.047	0.0031	-	-	[20]
H	Alloy 718Plus	Bal	9.66	17.42	5.48	2.72	0.71	1.46	0.028	0.0001	9.13	1.04	[122]
I	Alloy 939	Bal	-	22.4	2.4	-	3.7	1.9	0.15	-	19	2	[125]
J	Alloy 718S	53.4	18.5	18.5	5.0	1.0	0.5	-	-	-	-	-	[123]
K	Nimonic 105	Bal	0.098	15.03	-	4.96	1.25	4.85	0.128	0.005	20.12	-	[10]
L	Waspaloy	Bal	-	19.42	-	4.24	2.94	1.37	0.06	-	13.15	-	[126]
M	Waspaloy	57.8	0.40	19.6	0	4.25	2.92	1.44	0.018	-	13.8	-	[124]

	Alloy	Solutionising	Ageing
A	Alloy 625	1100 °C (0.5 h)	670, 720, 760 °C (up to 200 h)
B	Alloy 706	982 °C (1 h)	718 °C (8 h), 621 °C (8 h), 593 °C (up to 10000 h)
C	Alloy 718	982 °C (1 h)	718 °C (8 h), 621 °C (8 h), 593, 704 °C (up to 10000 h)
D	Alloy 718	1200 °C (1 h)	700, 725, 750 °C (up to 300 h)
E	Alloy 718	970 °C (1 h)	670, 700, 730 °C (up to 32 h)
F	Alloy 718	1100 °C (0.5 h)	720, 760, 800 °C (up to 200 h)
G	Alloy 718	1100 °C (0.5 h)	720, 760, 800 °C (up to 200 h)
H	ATI 718Plus	975 °C (1 h)	788°C (up o 50 h)
I	Alloy 939	1150 °C (4 h)	850 °C (6 h)
J	Alloy 718S	1024 °C (1.5 h)	788 °C (7 h)
K	Nimonic 105	1150 °C (4 h)	800, 900, 950 °C (up to 200 h)
L	Waspaloy	1150 °C (0.5 h)	700, 800 900, 1000 °C (up to 1000 h)
M	Waspaloy	1020 °C (4 h)	850 °C (4 h), 760 °C (16 h), 704 °C (up to 5000 h)

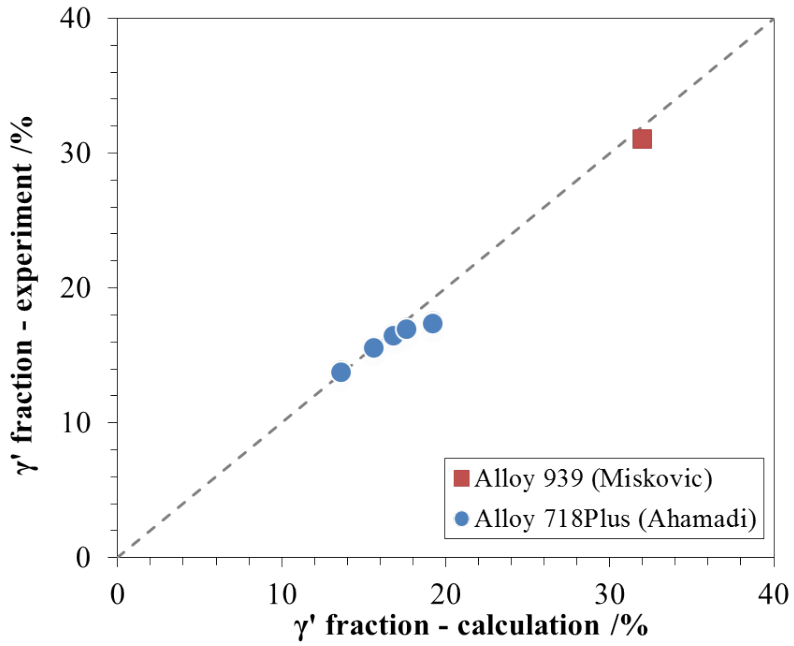

Fig. 3.7 Comparison between calculated and experimental γ' fraction of high-temperature alloys.

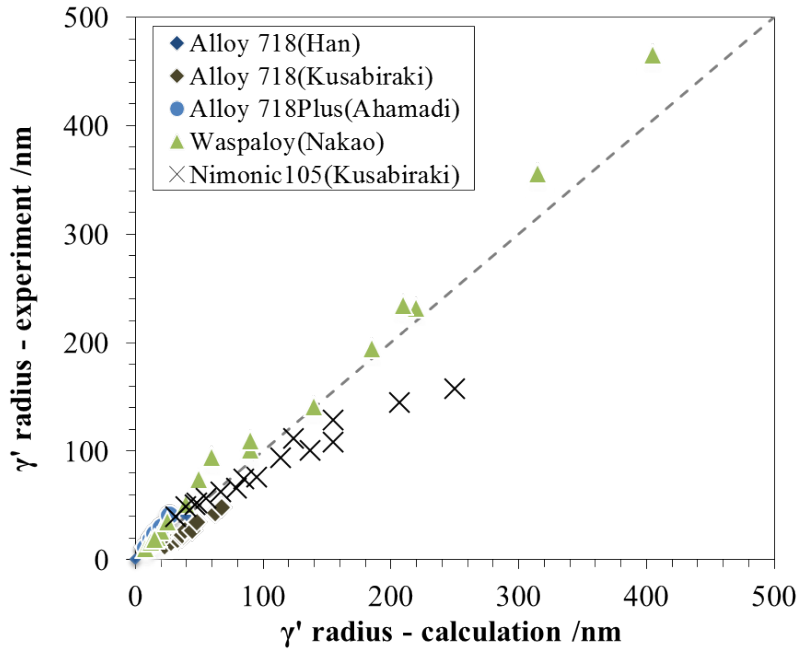

Fig. 3.8 Comparison between calculated and experimental mean γ' radius of high-temperature alloys.

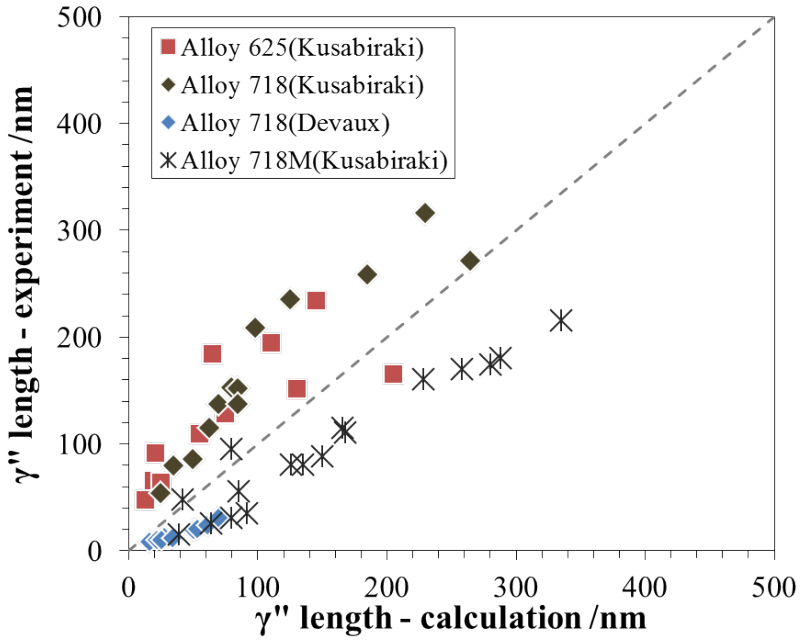

Fig. 3.9 Comparison between calculated and experimental mean γ'' length of high-temperature alloys.

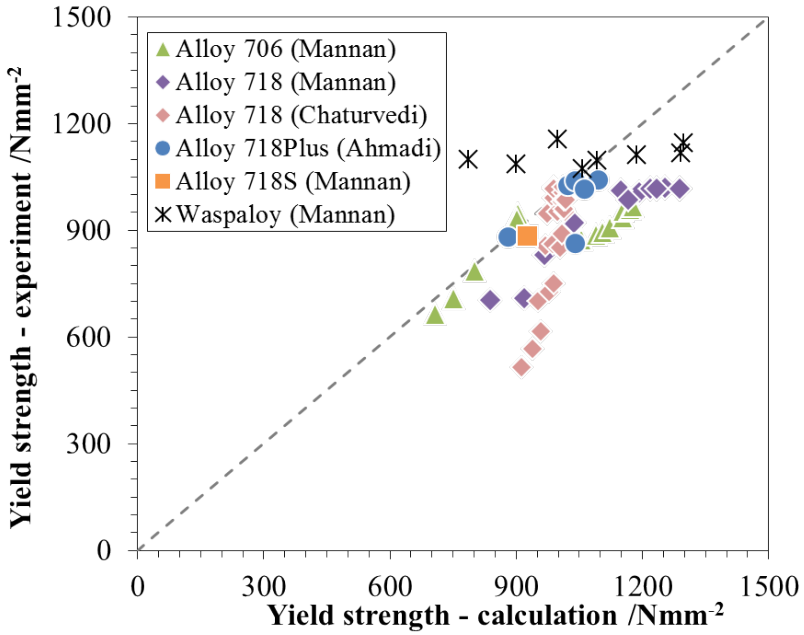

Fig. 3.10 Comparison between calculated and experimental yield stress of high-temperature alloys.

3.4 Alloy design case study

In this study, an alloy for the exhaust gasket is designed as an example of practising the integrated computational alloy design approach. A provisional target is set for the yield stress of the material to be 1000 MPa or higher after heat treatment at 750 °C for 400 hours, which imitates service conditions as a sealing part in cars. It would be quite beneficial to estimate strengthening by microstructural parameters for gaining insight into how the alloy with the aimed properties would be like.

The typical mean grain size of common high-temperature alloys is in the range of 10 to 50 μm. Assuming that the mean grain size is decreased to about 15 μm, the increment in strength by grain boundary strengthening mechanism would be about 250 MPa, which includes the friction stress. Solid solution strengthening also plays an important role as shown in the previous chapter. The increment of strengthening by solid solution is typically in the range of 100 to 200 MPa; 150 MPa is employed for estimation here. In terms of dislocation strengthening, it does not look promising to apply this strengthening mechanism since the dislocation density is low after the solutionising treatment and ageing. Hence, strengthening increment by forest hardening is ignored here.

Finally, but most importantly, it is obvious that precipitation strengthening has the biggest influence on the strength of the alloys discussed in this study. Based on the estimation that the sum of the grain boundary and solid solution strengthening is 400 MPa, the precipitation strengthening should be as high as 600 MPa to achieve a yield stress of 1000 MPa. Now, precipitation parameters necessary for this target are analysed. The γ' is considered as a strengthening precipitate because this intermetallic compound is the most common and promising precipitate in many alloys used in high-temperature environments. Figure 3.11 (a) shows the relationship between the increment of strength by precipitate and mean radius of γ'. For calculating this, other variables, such as the volume fraction and anti-phase boundary energy of γ' and the Taylor factor are fixed to 0.2, 0.32 J·mm^{-2} and 2.6, respectively. The figure tells us that the strength peaks when the average radius of γ' is around 10 to 20 nm. If the precipitates whose radius is in the range are uniformly dispersed in the matrix, it is highly probable that the yield stress of the alloy achieves 1000 MPa. However, reckoning that the mean size of precipitates is held to less than 20 nm after long time exposure at 750 °C looks too optimistic. Assuming the radius has a realistic value of 30 nm, the relationship between the strength and the volume fraction of γ' can be plotted as figure 3.11 (b). The figure indicates that an alloy consisting of 20 vol% γ' may have the yield strength of 1000 MPa. On the other hand, if the volume fraction of γ' is less than 15 vol%, it should only

have a slim chance to achieve the target unless it acquires the strength by other mechanisms, which is also not so straightforward.
To summarise, a yield stress of 1000 MPa can theoretically be broken down into 150 MPa by solid solution strengthening, 250 MPa by grain boundary strengthening with the mean grain diameter of 15 μm and 600 MPa by precipitation strengthening with γ' whose mean radius and volume fraction are 30 nm and 0.2, respectively. Although the estimation is rough and simplified, a realistic and also clearer image of the alloy to be designed has been given.

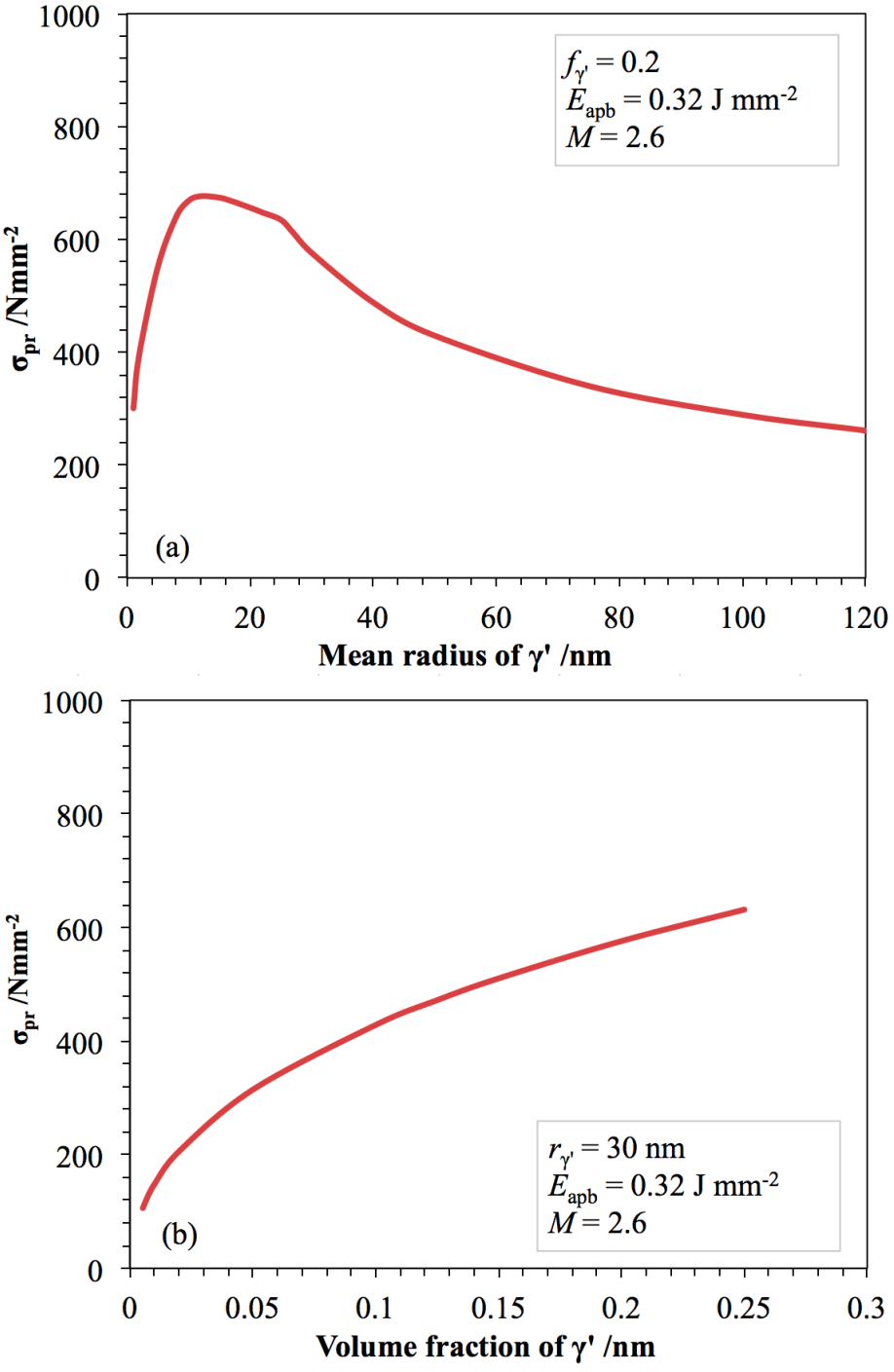

Fig. 3.11 Relation between strengthening increment due to precipitation and (a) size and (b) volume fraction of γ'. $f_{\gamma'}$, E_{apb} and M are volume fraction of γ', anti phase boundary energy of γ' and the Taylor factor, respectively.

3.5 Summary

In this chapter, the overall alloy design methodology is described after the review of calculation-aided alloy design approach and the genetic algorithm. For the prediction part of the design, the yield strength after a certain heat treatment and ageing are estimated from microstructural parameters calculated by MatCalc. Then, the chemistries of the alloy are optimised with the GA to obtain the highest yield strength with some cost and manufacturability constraints.

Calculations for the microstructural parameters and the yield strength of conventional alloys were compared with experimental values taken from literature, where the acceptable agreement between the calculation and measurement are obtained. The next chapter shows the optimised results by using a high-temperature alloy for the exhaust gasket material as a practical example of the designing process.

Chapter 4

Alloy design

In the last chapter, the overall idea for designing a new high-temperature alloy was introduced with a comparison between the calculated and experimental microstructural parameters and mechanical properties. In the present chapter, the alloy optimisation was performed and the results are described. Then, the calculations were experimentally validated via small cast ingot specimens.

4.1 Optimisation process

One of the main aims of the present study is to design a Fe-Ni-based alloy with an integrated computational optimisation approach described in the previous chapter. The overall design process is schematically summarised in Figure 4.1. A candidate alloy chemical composition was evaluated in terms of both cost and producibility constraints. Then, microstructural parameters, such as the size and fraction of precipitates, were calculated. The heat treatment employed here was for simulating the solutionising, ageing and service as a product. The yield stress after the heat treatment was then estimated from these microstructural parameters. The yield stress was incorporated as a fitness parameter in the GA.

Table 4.1 shows a summary of the main calculation parameters and conditions used in the optimisation. For the microstructure calculation, MatCalc version 5.61 with mc_ni2.011.tdb and mc_fe_2.010.ddb as thermodynamics and mobility databases were used. In the optimisation, ten elements: Ni, Fe, Cr, W, Nb, Al, Ti, Mo, Co and C, were considered. The maximum and minimum concentration of each element is in Table 4.2. The amount of them were divided into 30 different levels. So, the total combination of the chemical compositions would be as large as $30^9 = 2 \cdot 10^{13}$.

In the kinetic calculation by MatCalc, six phases: an FCC matrix, γ', γ'', η, δ and $M_{23}C_6$

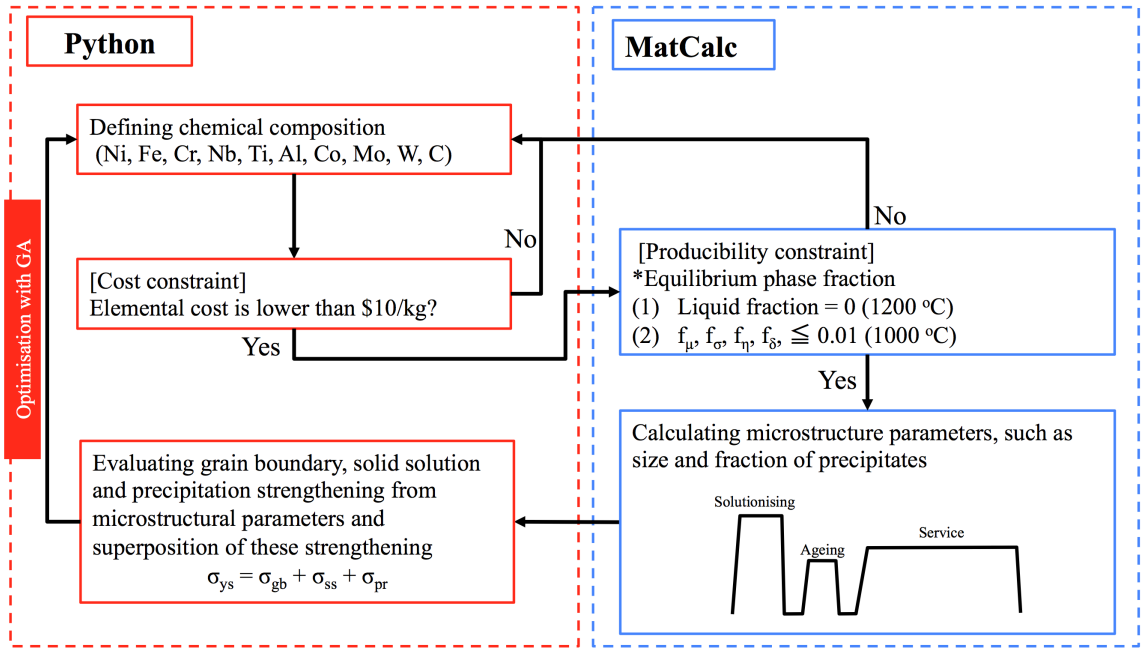

Fig. 4.1 Overall procedure for alloy design process performed in this study.

were taken into consideration. In addition to these six phases, liquid, σ and μ phases were also considered in the equilibrium calculation performed for the optimisation constraints. Each secondary phase was classified into ten size classes, which had precipitates with the same size and chemical compositions. Therefore, the size and chemical composition of precipitates were described not only as a mean value but also with a distribution. The mean grain diameter was fixed to 20 μm, which was in a typical grain size range of many high-temperature alloys manufactured by a cast and wrought process.

The heat treatments used for the microstructure parameter calculation are schematically illustrated in Figure 4.2. As shown in the figure, three different heat treatments were considered for simulating solutionising, ageing and service. The heat treatment at 1200 °C for 24 hours was employed as the solutionising, where heating and cooling rates were 1 °C·s^{-1} and 1000 °C·s^{-1}, respectively. 1200 °C was employed as the solutionising temperature for making every secondary phase fully solutionised in the matrix, although the solutionising temperature for conventional high-temperature alloys was usually lower than 1200 °C. As a heat treatment condition after solutionising, 720 °C for 16 hours was employed. Both 720 °C and 16 hours were in the range of typical conditions for ageing high-temperature alloys [124, 127, 128]. The temperature elevating and cooling rates were the same as those used in solutionising. Finally, heat treatment of 750 °C for 400 hours was adopted in the calculation. Although the temperature during service, in reality, is more complex, this proposed heating

Table 4.1 Parameters and conditions used for alloy design.

For microstructure calculation	
Software	MatCalc ver. 5.61
Elements	Ni, Fe, Cr, W, Nb, Al, Ti, Mo, Co and C
Phases	matrix(FCC), γ', γ'', η, δ and $M_{23}C_6$
Thermodynamics DB	mc_ni2.011.tdb
Mobility DB	mc_fe_2.010.ddb
Particle size classes	10
Grain diameter / μm	20
Room temperature / °C	20
Solutionising temperature and time / °C, hours	1200, 24
Ageing temperature and time/ °C, hours	720, 16
Service temperature and time/ °C, hours	750, 400

For estimating strength	
Taylor factor	2.6
Solid-solution strengthening	Table 3.6
Friction stress / MPa	100
G.B. strengthening coefficient / MPa·μm$^{-0.5}$	600
b / nm	$2.5 \cdot 10^{-10}$

For optimisation	
Cost constraint /\$ kg^{-1}	< 10
Producibility constraints	Equations 3.2 and 3.3
Mutation probability	0.2
Elite ratio	0.1
Population size	100
Total iteration	1000

pattern would provide a reasonable estimate [129].

In the optimisation process, cost constraints were implemented; the elemental cost defined in the previous chapter was limited to a maximum of \$10 per kg. The value was $2/3$ of the elemental cost of Alloy 718. Several constraints for producibility, which were also described in the previous chapter, were employed. Before the kinetics calculation, equilibrium calculations were performed at 1200 °C and 1000 °C. In these equilibrium calculations, liquid, σ and μ phases were also considered. As a constraint for guaranteeing hot forming feasibility, the amount of liquid at 1200 °C was limited to zero. In addition, any candidate compositions that formed μ, σ, η and δ at 1000 °C more than 0.01 in the volume fraction were omitted.

Table 4.2 Maximum and minimum amount of each element employed for optimisation (mass%).

	Ni	Fe	Cr	Nb	Mo	Ti	Al	Co	W	C
MAX	Bal.	60	25	5	5	5	5	10	5	0.01
MIN	20	40	10	0.001	0.001	0.001	0.001	0.001	0.001	0.001

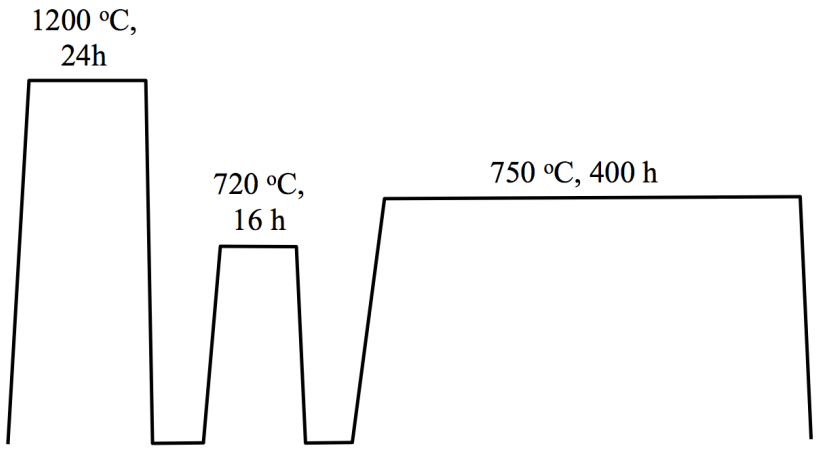

Fig. 4.2 Heat treatment employed for microstructure parameter calculation.

4.2 Genetic algorithm parameter selection

As previously described, the GA is employed as an optimisation heuristic. Before starting the optimisation, the influence of three calculation parameters: mutation probability, elite ratio and population size per generation on the efficiency of optimisation was investigated. The typical influence of each parameter on the optimisation calculation is described next.

- mutation probability (the probability of a mutation in each generation): If the mutation probability is high, the calculation would be more randomised and easy to escape from a local optimum although the efficiency of the calculation would be lower. If the value is low, it would be easier to become stuck on the local optimum.
- elite ratio (the ratio of candidate alloys passed down from one generation to the next without any change): This parameter is employed so that the highest fitness individuals in a generation can be preserved. However, if the elite ratio is too high, the probability to generate a better candidate would decrease.
- Population size (the number of chromosomes in each generation): If the size is too small, it would be more likely to be stuck on a local optimum, and to need a larger number of generations until convergence. However, a larger population size usually leads to longer calculation time.

For understanding the influence of these calculation parameters on the efficiency of the optimisation, calculations were performed with different optimisation parameters; 0.01 to 0.3 for mutation probability, 0.05 to 0.3 for elite ratio and 10 to 500 for population size. The total number of generations was determined so that the total number of calculations (product of population size and total generation) becomes equal. The combination of the parameters is shown in Table 4.3. For the sake of calculation speed, several simplifications were incorporated: (1) The concentration of each element was divided into only 10 levels (In the actual alloy designing process, the concentration was divided into 30 levels). (2) Only γ' were considered as secondary phase, whereas other secondary phases were considered in the actual optimisation process. 3) The heat treatment was also simplified; only heating at 750 $^{\circ}$C for 16 hours was considered.

Figures 4.3 show the relationship between the maximum fitness (the yield stress of a candidate alloy) and (a) mutation probability, (b) elite ratio and (c) number of population per generation. As shown in the figures, the maximum fitness changes by these calculation parameters and it is suggested that the mutation probability of 0.2, elite ratio of 0.1 and population size of 100 were appropriate parameters to find the optimised candidate efficiently. Therefore, in this study, these calculation parameters were employed.

Table 4.3 Calculation parameters (mutation probability, elite ratio, population size and total generation) and the maximum fitness (yield stress) obtained from the calculations.

mutation probability	elite ratio	population size	total generation	maximum fitness /MPa
0.01	0.1	50	200	1242
0.1	0.1	50	200	1285
0.2	0.1	50	200	1334
0.3	0.1	50	200	1322
0.2	0.05	50	100	1290
0.2	0.1	50	200	1334
0.2	0.2	50	100	1295
0.2	0.3	50	100	1288
0.2	0.1	10	1000	1297
0.2	0.1	25	400	1296
0.2	0.1	50	200	1334
0.2	0.1	100	100	1344
0.2	0.1	200	50	1292
0.2	0.1	500	20	1294

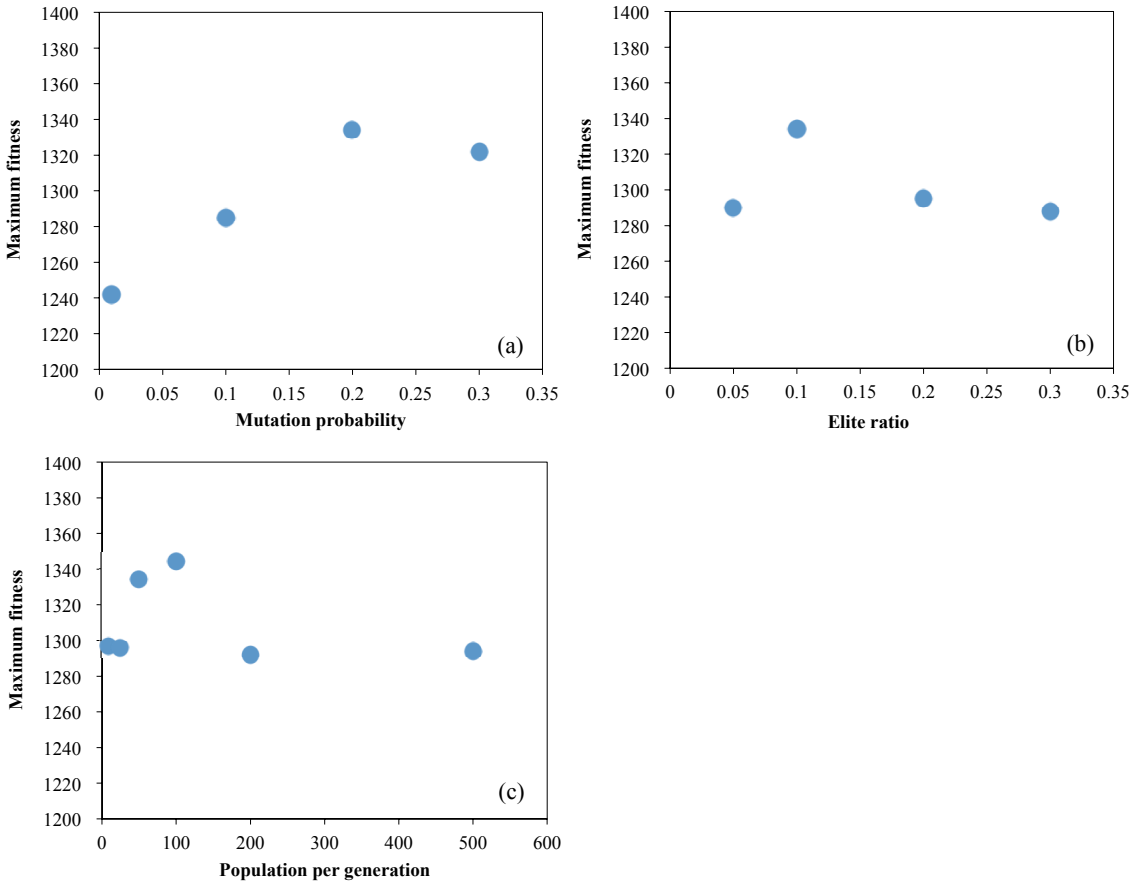

Fig. 4.3 Relation between the maximum fitness (yield stress) and (a) mutation probability, (b) elite ratio and (c) number of population per generation.

4.3 Optimisation results

Optimisation by the heuristics described so far was performed (the code used for the optimisation was attached on Appendix section). Table 4.4 shows the chemical compositions of the alloy resulting from the optimisation process (denoted as Fe-opt). Reference materials are also shown in the table; Alloy 718 is the most widely used commercial Ni-based high-temperature alloy and Alloy 660 is a conventional Fe-based γ' strengthened alloy. Fe-opt contains a higher amount of Ti, Al and W, but a lower amount of Nb and Mo than Alloy 718. Ni content of the optimised alloy is also smaller than 718, which contributes to the low elemental cost of Fe-opt.

Tables 4.5 and 4.6 respectively show microstructural parameters and strength after ageing, where f, r, l and E_{apb} denote the volume fraction of precipitates, mean radius of precipitates, diameter of disc-shaped precipitates and anti-phase boundary energy, respectively. According to the calculation, Fe-opt has a large amount of γ' and none of γ''. On the other hand, Alloy 718 is predicted to have both γ', γ'' phase in this calculation, which is supported by the literature [130]. As for Alloy 660, the volume fraction of γ' in Table 4.5 seems smaller than reported by researchers [25, 131, 132]. In the calculation, a database for Ni-based alloys was used. However, the amount of Ni in the alloy might have been too small to be calculated by the database.

As far as judging from the calculation, the amount of γ' in Fe-opt after the long-time heat treatment is much higher than that of Alloy 718 or Alloy 660. This can be understood by the high concentration of Al and Ti with a low amount of Nb. In addition to that, a very small amount of η, δ and $M_{23}C_6$ are predicted in Fe-opt, whereas a higher amount of these phases is predicted in Alloy 718. It is suggested that these microstructural characteristics of Fe-opt should result in the higher yield stress of the alloy than other reference alloys.

Table 4.4 Chemical composition (mass%) and elemental cost ($\$\cdot kg^{-1}$) of optimised alloy and reference materials [113].

		Ni	Fe	Cr	Nb	Mo	Ti	Al	Co	W	C	V	Cost
Fe-opt	Designed	32.49	42.54	15.62	0.31	0	2.81	1.56	0.94	3.72	0.01	0	-
Fe-opt	Actual	32.3	bal.	16.1	0.30	-	2.73	1.66	0.90	3.67	0.027	-	8.9
Alloy 718	Actual	51.9	bal.	17.7	5.3	2.8	1.0	0.55	-	-	0.03	-	14.8
Alloy 660	Actual	24.4	bal.	15.7	<0.002	1.20	2.09	0.20	0.08	0.03	0.045	0.31	5.8

Table 4.5 Calculated microstructure parameters of designed alloy and reference materials.

	$f_{\gamma'}$ /%	$r_{\gamma'}$ /nm	E_{apb} /J·mm^{-2}	$f_{\gamma''}$ /%	$l_{\gamma''}$ /nm	f_{η} /%	r_{η} /nm	f_{δ} /%	r_{δ} /nm	$f_{M_{23}C_6}$ /%	$r_{M_{23}C_6}$ /nm
Fe-opt	19.15	29.6	0.40	0	1.0	0.05	151	0	1	0.09	154
Alloy 718	6.7	32.0	0.36	14.8	7.0	0	2	6.8	914	0.4	184
Alloy 660	0.2	270	0.46	0	1.0	0.1	170	0	0	0.2	223

Table 4.6 Calculated strength of designed alloy and reference materials (MPa).

	σ_{ss}	σ_{gb}	$\Delta\sigma_{\gamma',apb}$	$\Delta\sigma_{\gamma',or}$	$\Delta\sigma_{\gamma'',coh}$	$\Delta\sigma_{\gamma'',or}$	$\Delta\sigma_{\gamma'}$	$\Delta\sigma_{\gamma''}$	$\Delta\sigma_{prec}$	σ_{ys}
Fe-opt	92	234	646	847	0	10	646	0	646	973
Alloy 718	118	234	378	463	60	217	378	60	383	735
Alloy 660	122	234	27	9	1	123	9	1	9	405

4.4 Experimental validation with a small cast

4.4.1 Experimental procedures

The designed alloy was experimentally characterised for validation. Alloys with chemical compositions shown in Table 4.4 were cast with an arc-melting furnace. The appearance of the 50-gram ingot is shown in Figure 4.4. The ingots were first homogenised in a vacuum glass tube at 1200 °C for 24 hours, then swaged into a rod shape from 11 mm to 7 mm in diameter. Swaged samples were then solutionised at 1200 °C for 24 hours followed by water quenching and aged at 720 °C for 16 hours followed by air cooling. Finally, the samples were heat treated at 750 °C for 400 hours, which simulated in-service conditions [129].
Samples for optical microscopy (OM) were prepared by polishing the alloy with a slurry containing 1 μm diamond powder and etching in aqua regia (the mixture of nitric acid and hydrochloric acid with the volume ratio of 1:3). For transmission electron microscopy (TEM), thin samples were prepared by electropolishing in a mixture of 10 % perchloric acid and 90 % methanol (cooled to -5 °C) with a twin-jet electro-polisher. TEM images were obtained by using Tecnai F20 with a 200 kV electron beam voltage. Vickers hardness was measured at room temperature on the ground surface of the OM specimen, where the indentation load was 10 kgf.

Fig. 4.4 Appearance of the ingot used for experimental validation.

4.4.2 Microstructures

Figures 4.5 and 4.6 show the OM and TEM images of the specimens. The microstructure of each alloy evolves as follows:

- Fe-opt: Few precipitates are found in the solutionised condition. However, after the ageing, a large number of very fine precipitates, which are supposed to be γ' particles, are dispersed almost uniformly through the matrix as shown in the TEM image (Figure 4.6 (a)). After the heat treatment at 750 °C for 400 hours, many precipitates still remain although they are coarsened to several tens nm in diameter (Figure 4.6 (b)). Also, some precipitates are present on grain boundaries after the long-time ageing treatment (Figure 4.5 (c)).
- Alloy 718: The solutionised alloy does not have any precipitates except for some sparsely dispersed bulky ones (Figure 4.5 (d)). The microstructure after the ageing treatment at 750 °C for 400 hours contains many needle-like precipitates not only at grain boundaries but in the matrix (Figure 4.5 (f)). The result is agreeable to the calculation result that predicted the existence of a high fraction of δ phase.
- Alloy 660: Some large compounds are observed in the solutionised condition. Many precipitates are formed during ageing. Compared with Fe-opt, the amount of large precipitate on grain boundaries after the long-time ageing is small. It is also confirmed that the fine precipitates (γ') are seen in the alloy after the long time ageing.

4.4.3 Hardness

Figure 4.7 shows the experimental Vickers hardness of the samples after the solutionising, ageing and long-time (400 hours) heat-treatment. By comparing long-time heat treated samples, Fe-opt shows the highest hardness of the three. All samples show increasing hardness upon ageing for 16 hours. Fe-opt keeps its hardness and actually becomes even harder after the long-time heat treatment, whereas the reference alloys become softer.
It should be mentioned that, as shown in Table 4.4, elemental cost of Fe-opt is lower than that of Alloy 718 [113], which can render the alloy competitive in practice. The experimental results so far have demonstrated the high potential of the designed alloy. Further investigations for validating the performance of the designed alloy are presented in the next chapter, where a larger sample is prepared by the process that imitates mass-production (hot and cold rolling) and is experimentally validated.

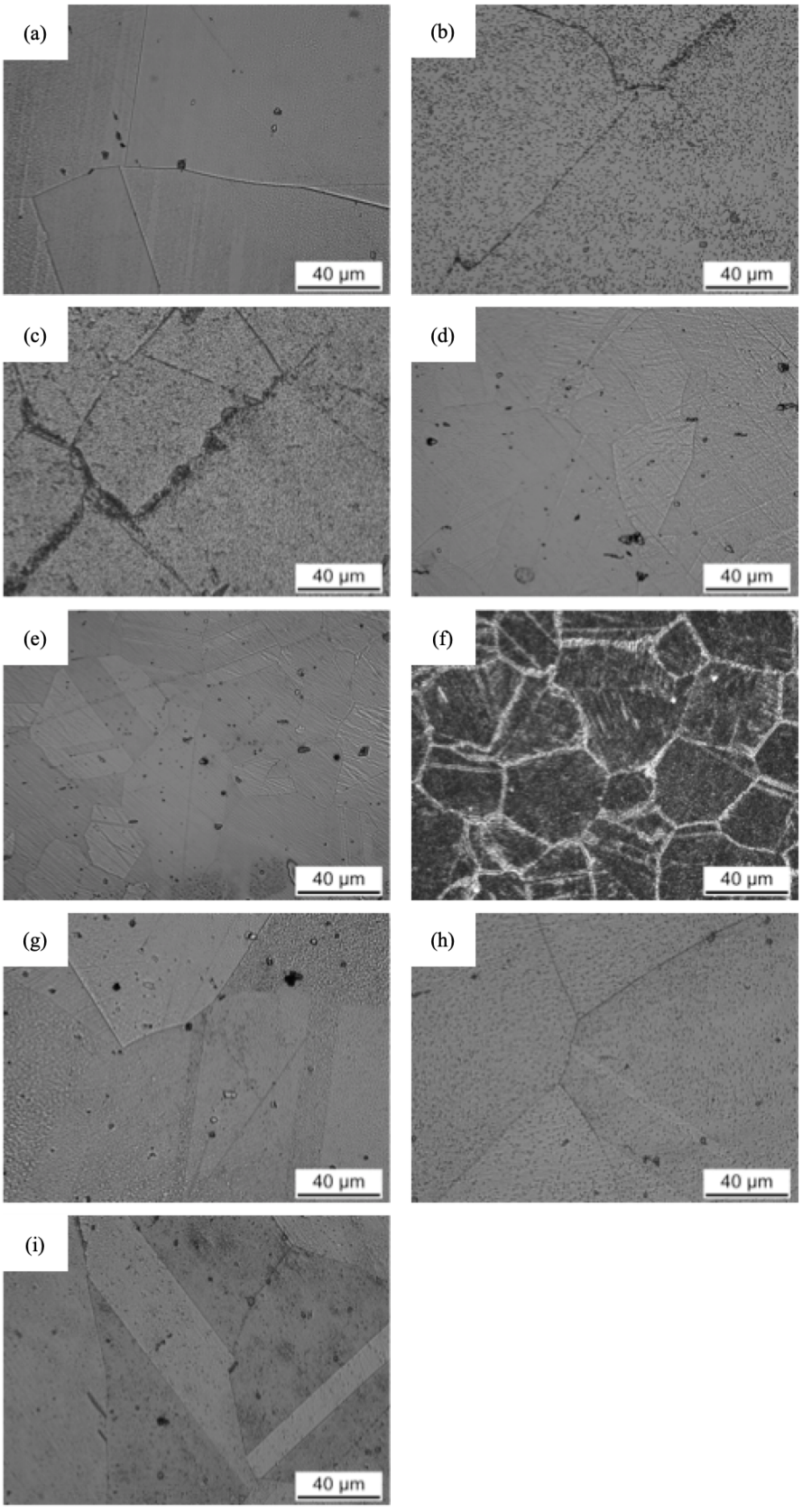

Fig. 4.5 Optical microscopy images of the samples. (a)-(c): Fe-opt, (d)-(f): Alloy 718, (g)-(i): Alloy 660. (a), (d) and (g): solutionised, (b), (e) and (h): aged for 16 hours and (c), (f) and (i): heat treated for 400 hours.

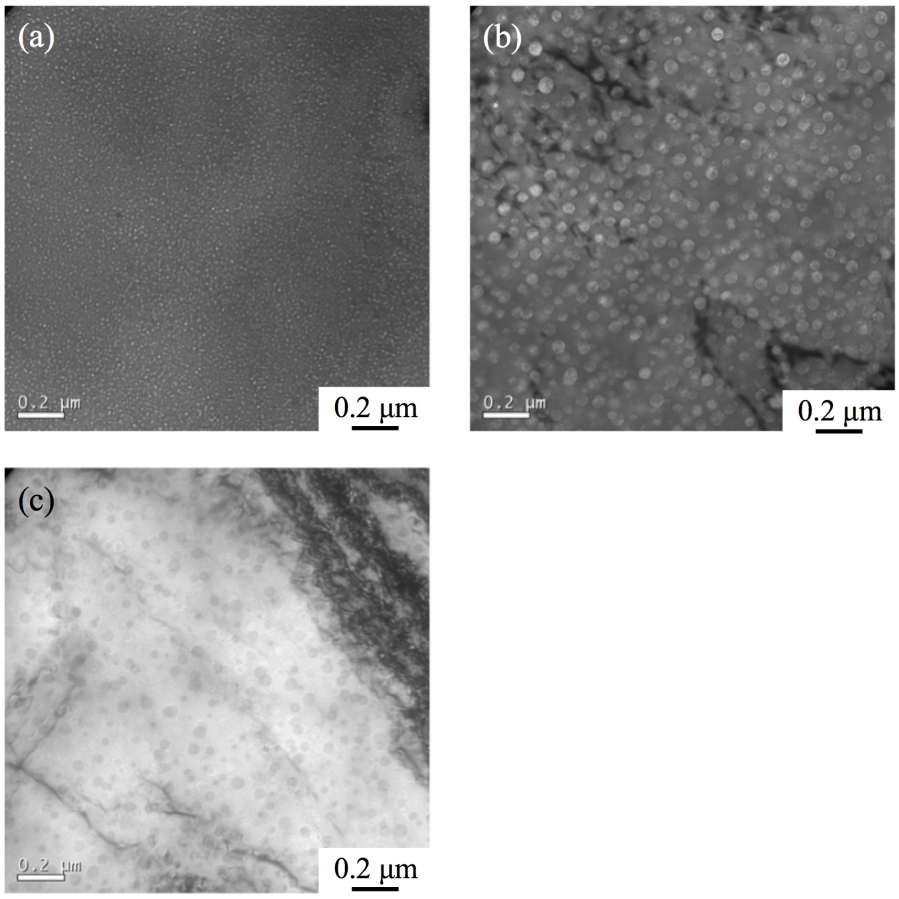

Fig. 4.6 TEM (bright field) images of (a) Fe-opt aged at 720 °C for 16 hours, (b) Fe-opt aged at 720 °C for 16 hours and subsequent 750 °C for 400 hours, and (c) Alloy 660 aged at 720 °C for 16 hours and subsequent 750 °C for 400 hours.

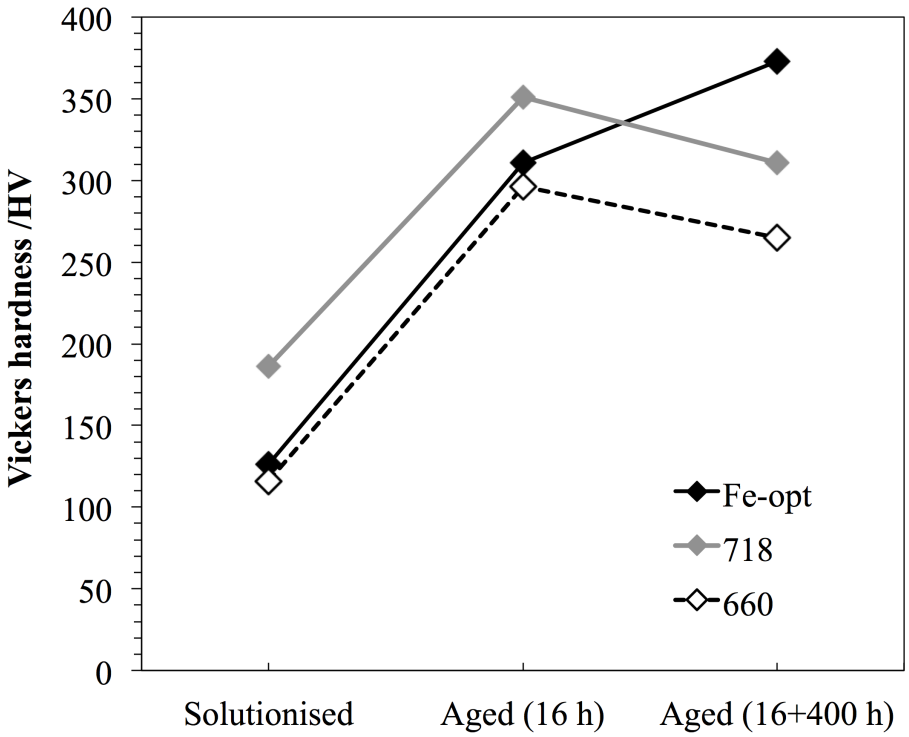

Fig. 4.7 Experimental Vickers hardness of samples after solutionising and ageing treatment at 720 °C for 16 hours and subsequent 750 °C for 400 hours.

4.5 Summary

The new high-temperature alloy with high strength after long time ageing was designed by a combinatory design approach including microstructure kinetics simulation, classical strengthening theories and the genetic algorithm. The optimised chemical composition was 43Fe-33Ni-16Cr-2.8Ti-1.6Al-0.9Co-0.31Nb whose elemental cost was relatively low due to the low amount of nickel. The microstructure and mechanical properties of the alloy was experimentally validated and compared with conventional high-temperature alloys (Alloy 718 and Alloy 660). The designed alloy kept higher hardness than Alloy718 and 660 after 400-hour ageing treatment at 750 °C. According to the TEM analysis of the designed alloy, the high hardness of the alloy is thought to stem from γ' particles finely dispersed in the matrix.

Chapter 5

Experimental validation with alloy sheet sample

In the previous chapter, an alloy with high strength after the long time exposure to a high-temperature environment was designed by a combination of microstructure/properties calculations and optimisation heuristics using a genetic algorithm. The alloy was experimentally produced from a small cast ingot of 50 grams and was proved to have a hardness superior to a conventional high-temperature alloy, such as Alloy 718, after a long-time high-temperature ageing treatment at 750 °C for 400 hours
In the present chapter, further experimental validation of the designed alloy is presented. As for the experiment, an alloy sheet sample with the optimised chemical composition is prepared through a way similar to an industrial cast and wrought manufacturing process. Then, the microstructure evolution during ageing treatment and the mechanical properties are investigated. Alloy 718Plus, a newly developed γ' strengthening alloy, is used as reference material and compared to the designed alloy [28, 127, 133].

5.1 Experimental procedures

5.1.1 Sheet sample preparation

The designed alloy sheet was produced through a way similar to an industrial mass production schedule. Figure 5.1 shows the sheet sample production procedure for the designed alloy and reference material (Alloy 718Plus). The appearance of the designed alloy in each step is presented in Figures 5.2. First, 25 kg ingots were cast by a vacuum induction-melting

furnace in Nippon steel. The casting mold of 95 x 95 mm^2, 115 x 115 mm^2 and 300 mm for the bottom, top and depth, respectively, was used. The casting temperature was 1550 °C. The chemical composition of the resulting alloys is presented in Table 5.1. The composition was measured by an inductivity coupled plasma optical emission spectrometer for metal elements, an infra-red absorption method after combustion in an induction furnace for carbon and an inert gas fusion thermal conductivity detection method for nitrogen. As shown in the table, the actual chemistries of the ingots are confirmed to be accurately controlled as designed. The ingots were ground for obtaining a smooth surface (Figure 5.2 (a)). The ground samples of 90 x 90 x 200 mm^3 were then soaked at 1100 °C for 2 hours and hot forged into a slab of 45 x 100 x 400 mm^3 in thickness, width and length, respectively (Figure 5.2 (b)). The slabs were reheated at 1150 °C for 1 hour and hot rolled by 3 rolling passes to 4 mm in thickness. As shown in Figure 5.2 (c), any cracks were not observed on the edge of the hot-rolled sheets, which was beneficial in terms of the production costs because any trimming process would not be necessary. The hot rolled sheets were repeatedly heat treated and cold rolled to obtain a cold-rolled sheet of 0.4 mm in thickness. Again, no crack was observed on the edge of the cold-rolled sheets. So any serious difficulties in producing the alloy sheet of the designed chemical composition have not been found as far as checking the appearance of the laboratory-scale produced samples. The sheets were solutionised at 1100 °C for 30 minutes subsequently water quenched to the room temperature, and pickled by hydrofluoric acid (Figure 5.2 (d)). Finally, the solutionised specimen was aged at 750 °C for up to 400 hours followed by air-cooling.

Table 5.1 Chemical composition of the designed (Fe-opt) and reference (Alloy 718Plus) alloys in mass%.

		C	Si	Mn	P	S	Cu	Ni	Cr	Mo	V	Nb	Al	Ti	B	W	Co	N
Fe-opt	Designed	0.01	-	-	-	-	-	32.5	15.6	0.001	-	0.31	1.56	2.81	-	3.72	0.94	-
Fe-opt	Actual	0.010	0.08	0.1	0.016	0.001	0.01	32.8	15.5	0.01	0.01	0.32	1.59	2.84	0.002	3.74	0.89	0.0013
718Plus	Actual	0.021	0.09	0.1	0.015	0.001	0.01	52.2	18.1	2.75	0.01	5.34	1.48	0.73	0.002	1.06	9.03	0.0035

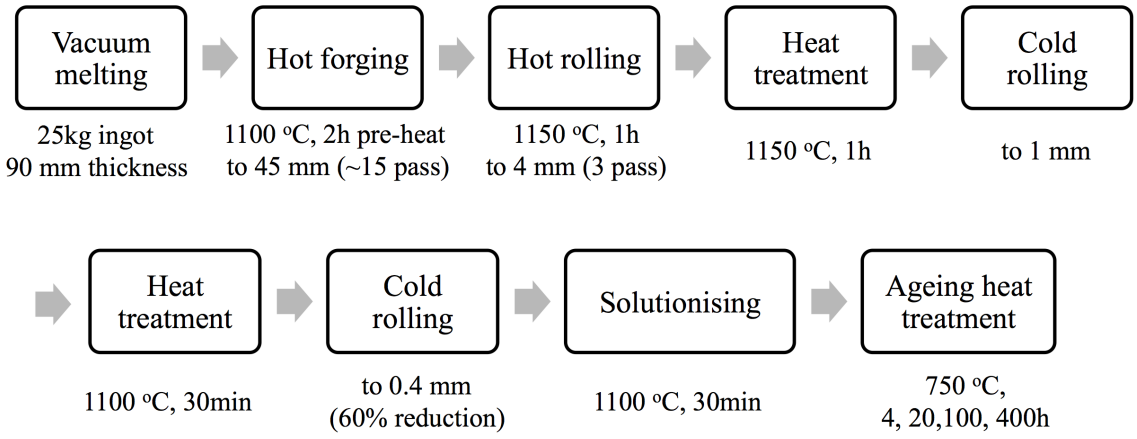

Fig. 5.1 Alloy sheet preparation procedure.

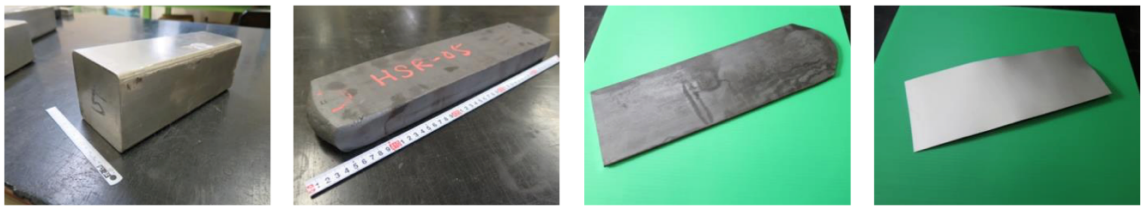

Fig. 5.2 Appearance of the designed alloy in each preparation process.

5.1.2 Procedure for microstructure and mechanical property investigation

The microstructures of the solutionised and aged specimens were investigated by optical microscopy (OM), scanning electron microscopy (SEM) and transmission electron microscopy (TEM) with energy dispersive spectroscopy (EDS). The OM and SEM were carried out on the cross section perpendicular to the rolling direction polished and etched by aqua regia (the mixture of nitric acid and hydrochloric acid with the volume ratio of 1:3). The thin foil specimen for TEM was prepared by mechanical polishing to about 50 μm in thickness and electropolishing in a mixture of 10 % perchloric acid and 90 % methanol with a twin jet polisher at -5 °C. The observation was conducted with a JEOL JEM-2100Plus operated at 200 kV.

The mechanical properties were investigated by a Vickers hardness test and tensile test at

room temperature for the aged and unaged specimens. The hardness was measured on the cross section perpendicular to the rolling direction with a load of 0.5 kgf. The tensile test specimens were prepared according to Japanese Industrial Standard Z2241 “Method of tensile test for metallic materials” No. 13 (b) whose gauge length and width were 50 mm and 12.5 mm, respectively.

5.2 Experimental results

5.2.1 Microstructure characteristics

Figures 5.3 and 5.4 show the OM images of Fe-opt and 718Plus (solutionised at 1100 °C for 0.5 hour and aged at 750 °C for 4, 20, 100 and 400 hours after the solutionising), respectively. In both alloys, some inclusions are dispersed in the solutionised condition as can be seen in the figures. After the ageing treatment, large precipitates are observed on grain boundaries in Fe-opt and the volume of them increases with the ageing time, whereas large precipitates are rarely observed in 718Plus by the OM even after the 400-hour ageing.
Figures 5.5 show the SEM images of these materials aged for 400 hours. The results of the chemical composition analysis by SEM-EDS are summarised in Table 5.2. The results reveal that coarse precipitates in aged Fe-opt contain a higher amount of W than the matrix. Coarse precipitates are also found in 718Plus. The blocky precipitate on the grain boundaries of 718Plus (Figures 5.5 -p3) is Nb(C, N), according to the EDS results.

Considering that the resolution of the SEM used is not high enough for analysing the fine precipitates expected in the alloys, the aged specimens were also investigated by TEM. Figures 5.6 and 5.7 show transmission electron micrographs of fine precipitates observed in Fe-opt and 718Plus aged at 750 °C for 400 hours. Both materials contain fine precipitates dispersed in the matrix and they are identified as γ' by the diffraction patterns. The shape of γ' in Fe-opt and 718Plus are slightly different: the precipitates in Fe-opt are spherical whereas that in 718Plus shows the morphology between spherical and cuboidal. As the shape of γ' is known to change from spherical to cuboidal with increasing ageing time, the experimental results are consistent with the former studies [1, 15]. Figure 5.8 shows γ' size distribution in Fe-opt and 718Plus measured from the TEM images. The average radii of γ' in Fe-opt and 718Plus are 24 and 35 nm, respectively and γ' in Fe-opt is smaller than those in 718Plus, which is consistent with the calculation results shown later. The γ' in both alloys show uni-modal distribution, which suggests that the γ' particles precipitate mainly at the ageing stage rather than solutionising or its cooling stage.
As shown in the SEM images (Figure 5.5), both Fe-opt and 718Plus contain coarse precipitates other than fine γ'. Figures 5.9 and 5.10 show the TEM images of coarse precipitates in Fe-opt and 718Plus. Table 5.3 shows the chemistries of these coarse precipitates investigated by EDS attached to the TEM. In Fe-opt, most coarse precipitates are identified as Laves phase, although σ phase is also observed. These Laves phases contain a high amount of W as can be seen in Table 5.3. Ti and Nb, which are supposed to form γ' are also consumed in the

Table 5.2 Chemistries of Fe-opt and 718Plus measured by SEM-EDS (the location signs, such as "m1" refer to Figures 5.5).

Element	Fe-opt			718Plus		
	m1	p1	p2	m2	p3	p4
Ni	31.4	16.9	32.2	50.3	8.88	48.3
Fe	43.3	40.6	39.8	10.4	2.95	10.0
Cr	16.3	33.7	15.3	19.0	4.23	16.9
Al	3.85	2.62	5.25	3.93	0.49	4.59
Nb	-	-	-	3.01	63.3	5.28
Ti	3.42	2.50	3.65	0.91	10.7	1.35
W	1.65	3.71	3.72	0.94	1.63	1.85
Mo	-	-	-	1.86	5.22	2.14
Co	-	-	-	9.33	2.16	9.17

Laves phase. On the other hand, P phase ($Cr_9Mo_{21}Ni_{20}$) is observed on the grain boundaries of Alloy 718Plus. The P phase is one of the typical TCP phases observed in Ni-based superalloys and it is closely related to σ phase [134–136]. η and δ phases, which are often reported to precipitate in aged 718Plus [137–139], are not observed in the alloy prepared in the present study. The precipitates observed in Fe-opt and 718Plus are summarised in Table 5.4.

Table 5.3 TEM-EDS chemical composition analysis results for coarse precipitates observed in Fe-opt and 718Plus aged at 750 °C for 400 hours. The precipitates (a) to (e) in Fe-opt and (a) and (c) in 718Plus refer to Figure 5.9, and 5.10, respectively.

Element	Fe-opt			718Plus	
	(a)	(c)	(e)	(a)	(c)
Ni	7.8	29.5	6.1	26.1	28.8
Fe	44.8	32.8	46.4	9.0	8.3
Cr	44.5	15.3	21.8	18.7	18.1
Nb	-	3.2	5.3	13.2	13.5
Ti	-	4.7	1.3	-	-
W	2.9	14.6	19.1	1.5	1.5
Mo	-	-	-	16.4	17.6
Co	-	-	-	13.1	10.5
Si	-	-	-	2.2	1.6

Table 5.4 Summary of the phases precipitated in Fe-opt and 718Plus during ageing treatment.

Alloy	precipitate	site
Fe-opt	γ'	matrix
	Laves	grain boundaries
	σ	grain boundaries
718Plus	γ'	matrix
	P phase	grain boundaries

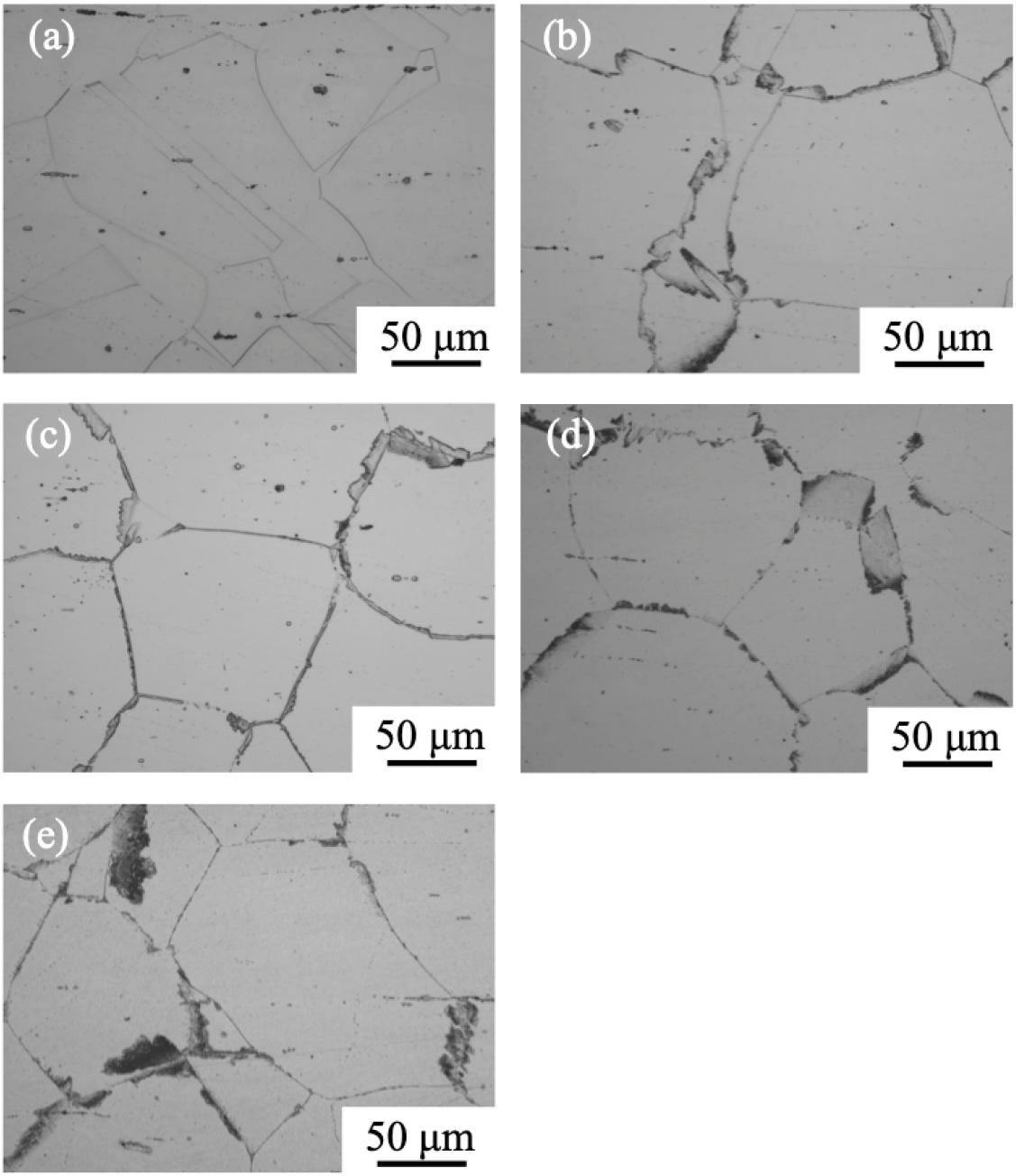

Fig. 5.3 Optical micrographs of the cross-section perpendicular to the rolling direction of Fe-opt. The specimens were (a) solutionised at 1100 °C for 0.5 hour and subsequently aged at 750 °C for (b) 4, (c) 20, (d) 100 and (e) 400 hours.

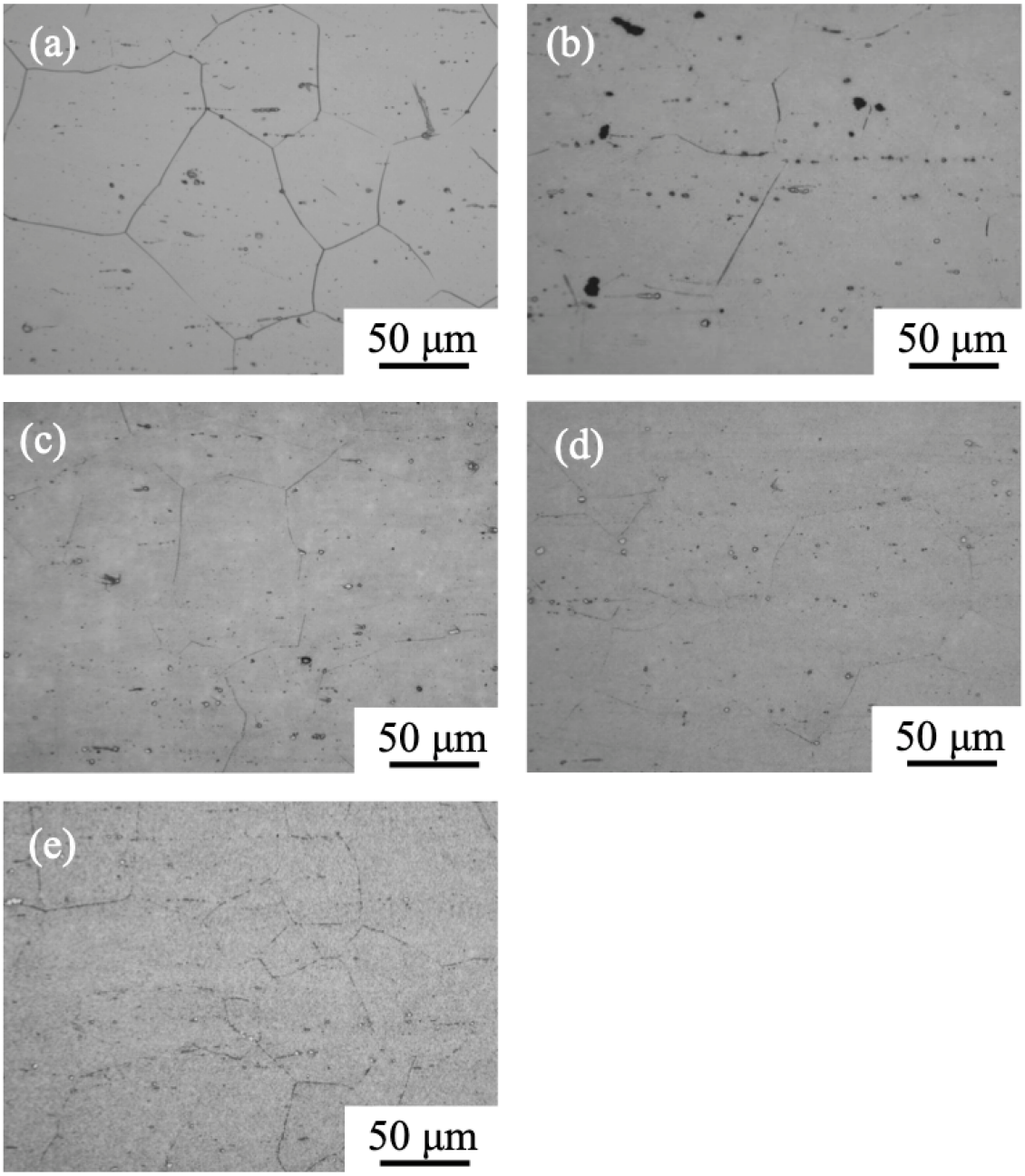

Fig. 5.4 Optical micrographs of the cross-section perpendicular to the rolling direction of 718Plus. The specimens were (a) solutionised at 1100 °C for 0.5 hour and subsequently aged at 750 °C for (b) 4, (c) 20, (d) 100 and (e) 400 hours.

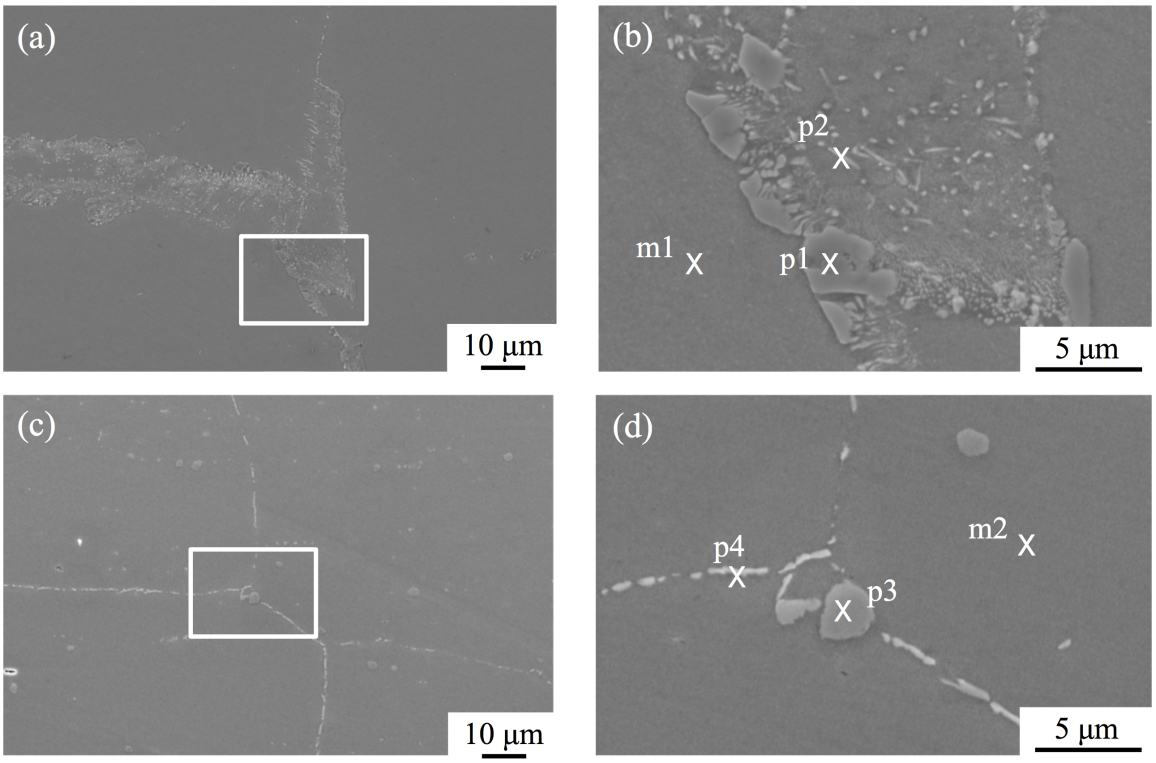

Fig. 5.5 SEM images of the cross-section perpendicular to the rolling direction of Fe-opt (a, b) and 718Plus (c,d) aged at 750 °C for 400 hours.

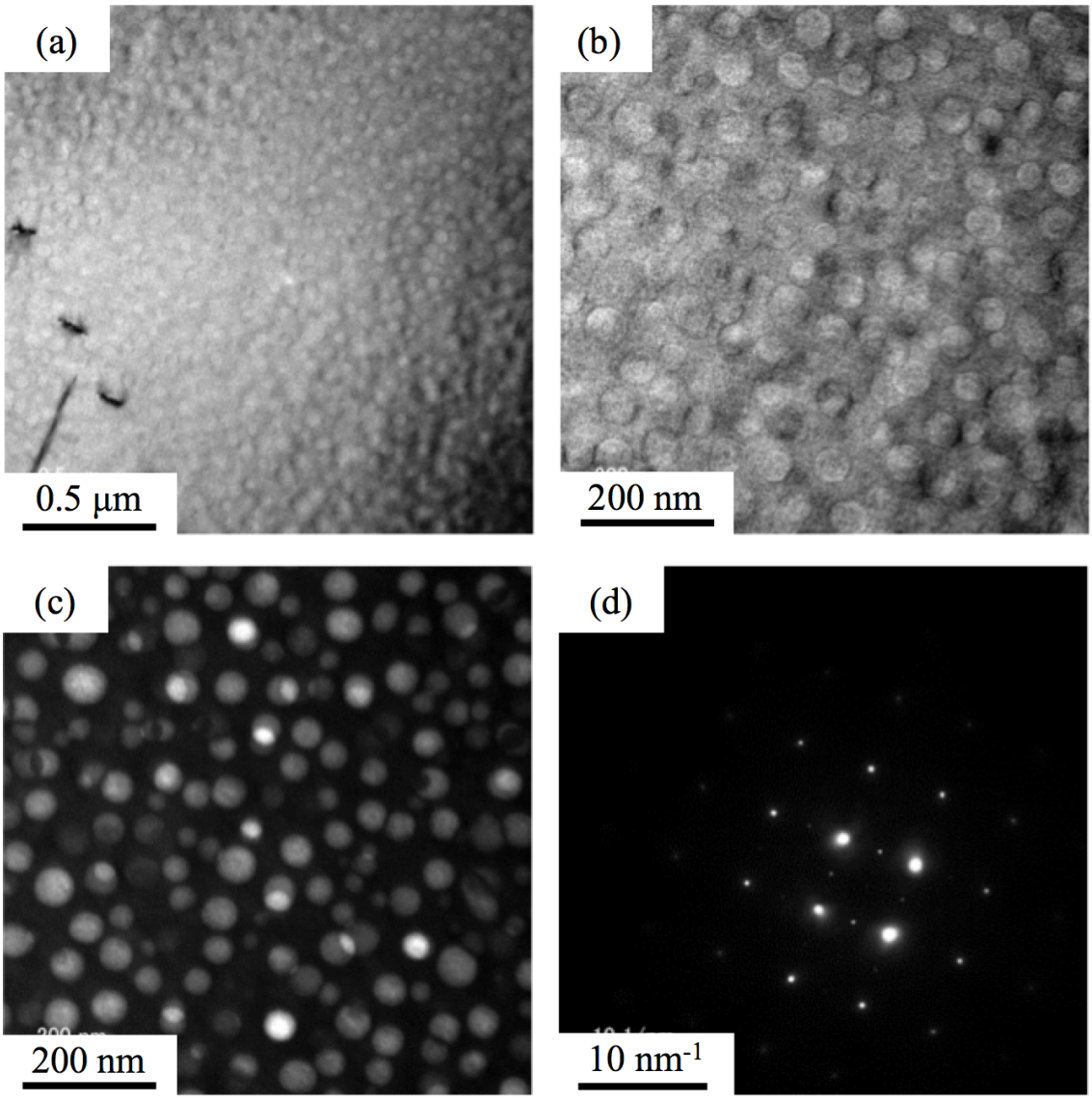

Fig. 5.6 TEM images of fine precipitates in Fe-opt. Pictures (a) and (b): bright field images, (c): dark field image and (d): diffraction pattern.

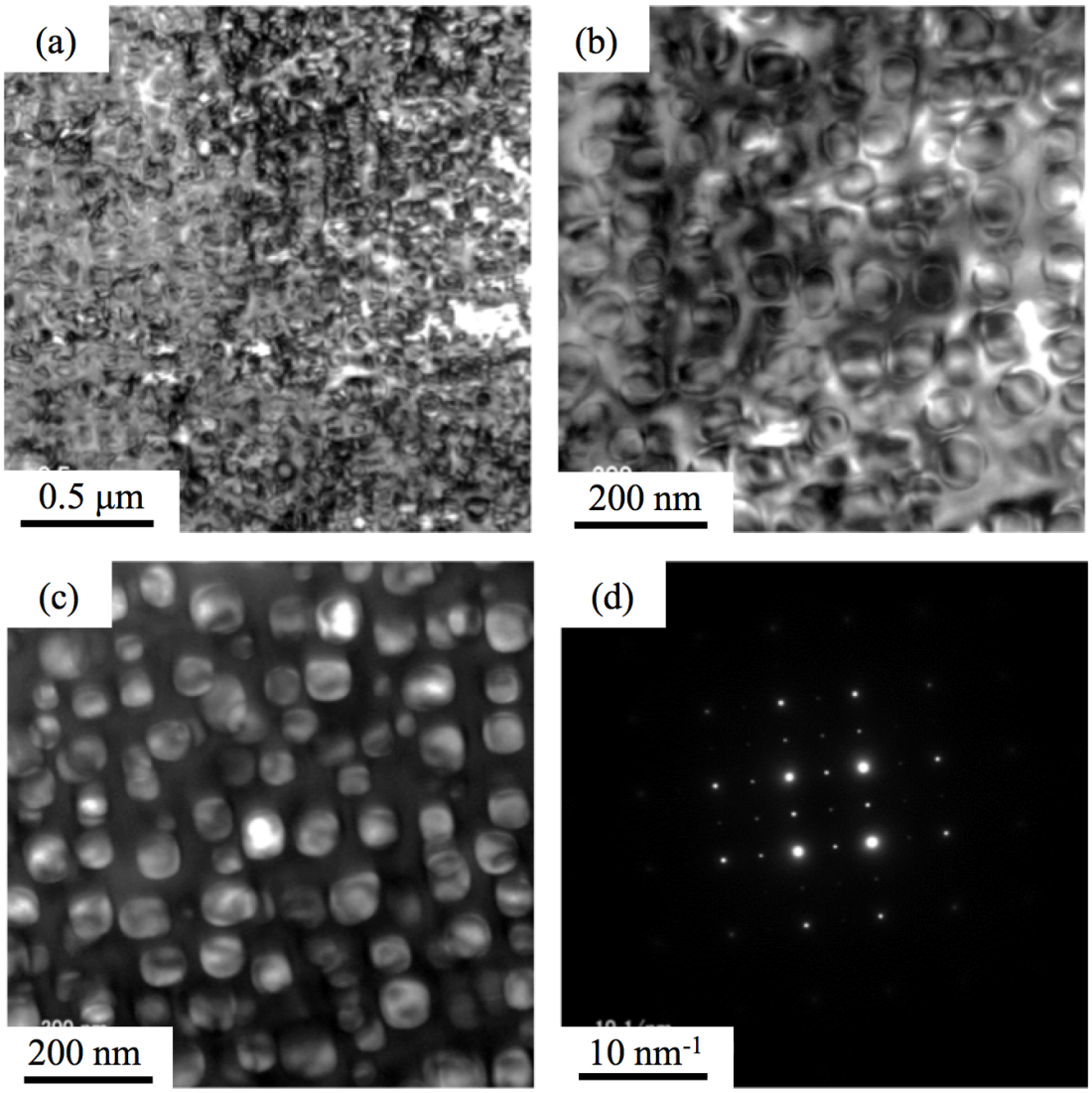

Fig. 5.7 TEM images of fine precipitates in 718Plus. Pictures (a) and (b): bright field images, (c): dark field image and (d): diffraction pattern.

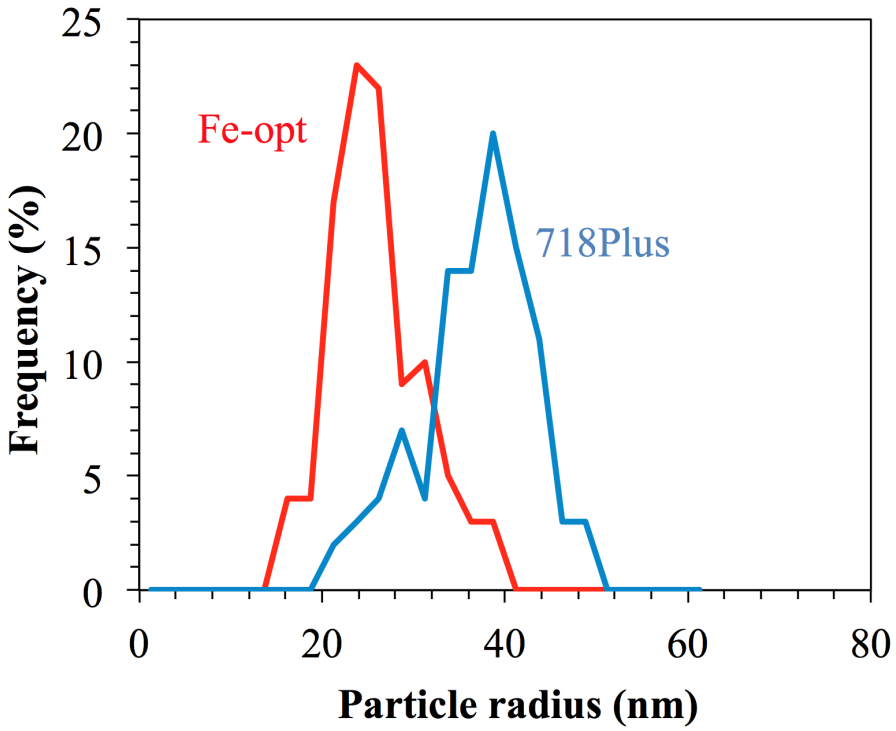

Fig. 5.8 γ' size distributions in Fe-opt and 718Plus measured from TEM images.

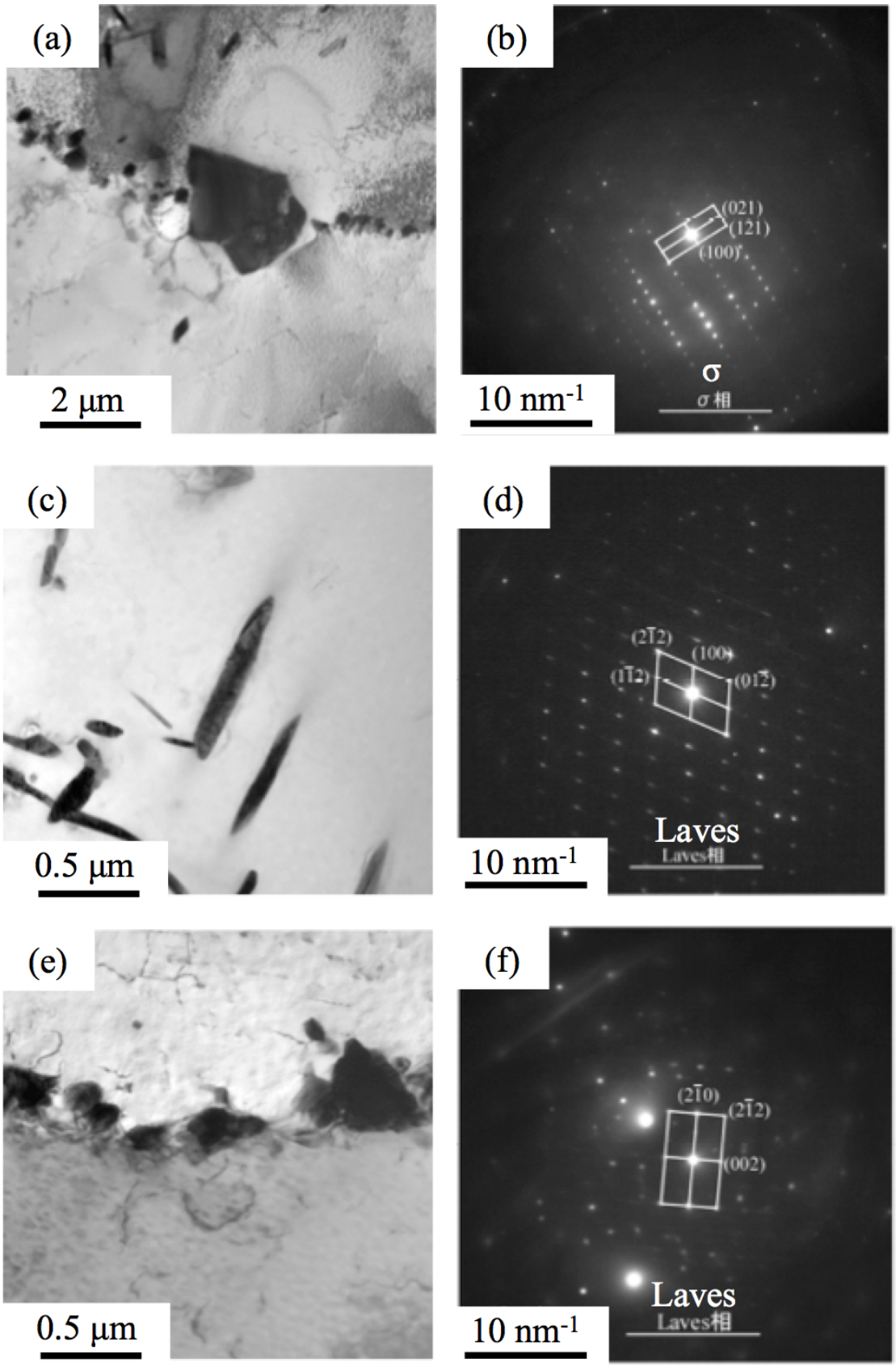

Fig. 5.9 TEM images of coarse precipitates in Fe-opt aged at 750 °C for 400 hours. Pictures (a), (c) and (e): bright field images and (b), (d) and (f): diffraction patterns.

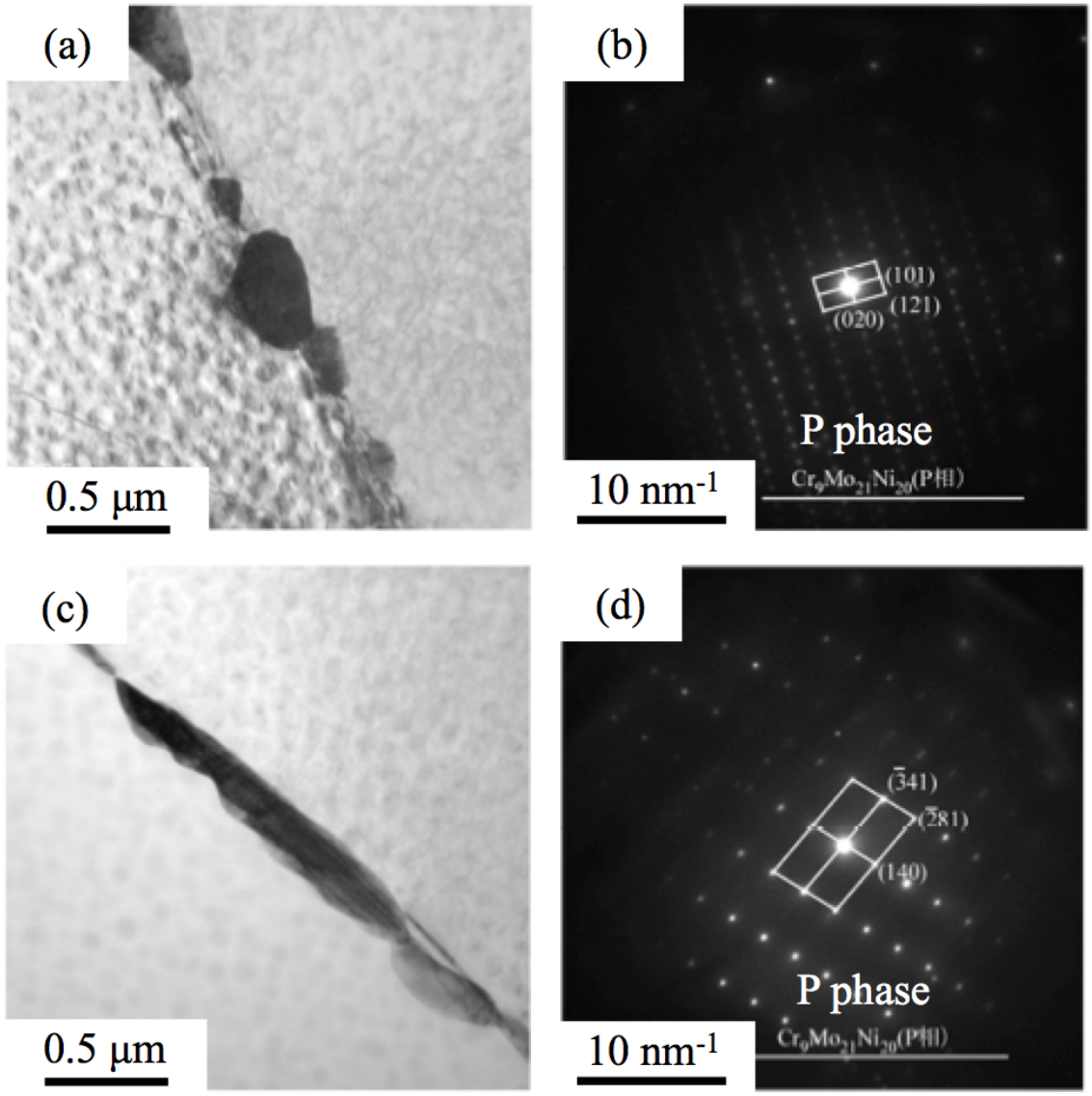

Fig. 5.10 TEM images of coarse precipitates in 718Plus aged at 750 °C for 400 hours. Pictures (a) and (c): bright field images and (b) and (d): diffraction patterns.

5.2.2 Mechanical properties

Figure 5.11 (a) shows the hardness of the designed and reference alloys before/after ageing treatment at 750 °C for 4, 20, 100 and 400 hours. The hardness of both alloys increases substantially by the short-time ageing treatment and decreases by a long-time ageing. In both alloys, the highest hardness is achieved when they are aged for 100 hours. Although the hardness of 718Plus is higher than that of Fe-opt in any ageing time in the present experiment, the hardness of 400-hour aged samples of these alloys is similar to each other. Comparing the results between specimens aged for 100 hours and 400 hours, the hardness of Fe-opt decreases only slightly with the ageing time whereas that of 718Plus decreases rapidly.
Figures 5.11 (b), (c) and (d) show the 0.2% yield stress, tensile strength and total elongation, respectively, of Fe-opt and 718Plus as a function of ageing time at 750 °C. The values are also summarised in Table 5.5 with the hardness test results. The 0.2% yield stress shows a similar tendency with the hardness in the sense that they increase rapidly by the short-time ageing treatment. However, the difference is found that the highest yield stress in Fe-opt is achieved when it is aged for 400 hours (the maximum ageing time in the experiment) and it marginally exceeds that of 718Plus. As the alloy is designed for obtaining high yield stress after the ageing at 750 °C for 400 hours, the result indicates the excellent potential in Fe-opt for the material used for automobile sealing parts. The tensile strength of 718Plus is higher than that of Fe-opt in all ageing conditions. The total elongation of Fe-opt and 718Plus are almost the same after the solutionising (without ageing) and it decreases with the ageing time. The decrease in the elongation by the ageing treatment is more substantial in Fe-opt, especially when the ageing time is 100 hours or longer. Although the total elongation is not aimed for in this alloy designing process, the lack of ductility might cause crack initiation during the service at high temperatures, which might become a potential disadvantage of the material. As shown in the previously described SEM and TEM microstructure images, Fe-opt contains a high fraction of coarse Laves and σ phases on grain boundaries when it is aged for a long period of time. The low elongation demonstrated in Fe-opt might have been caused by these coarse precipitates.

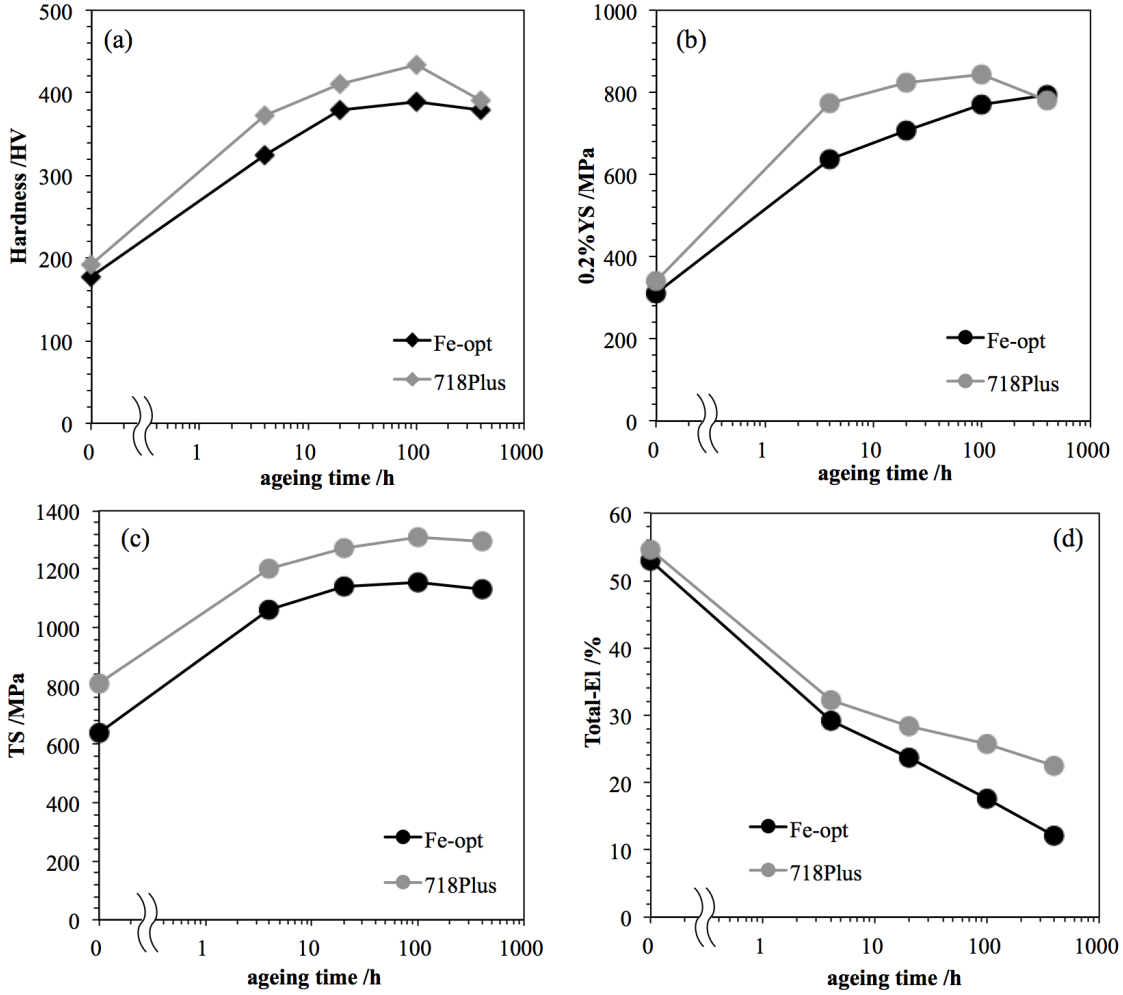

Fig. 5.11 Mechanical properties of Fe-opt and 718Plus. Figure (a): Vickers hardness, (b): 0.2% yield stress, (c): tensile strength and (d): total elongation.

Table 5.5 Mechanical properties of Fe-opt and 718Plus aged at 750 °C for up to 400 hours.

ageing	Fe-opt				718Plus			
/h	Hardness/HV	0.2% YS /MPa	TS /MPa	t-El /%	Hardness/HV	0.2% YS /MPa	TS /MPa	t-El /%
0	177	309	640	53	191	339	810	55
4	325	636	1060	29	373	773	1200	32
20	379	707	1142	24	410	824	1272	28
100	389	772	1154	18	433	843	1309	26
400	380	794	1130	12	390	779	1295	23

5.3 Discussion (comparison between calculation and experiment)

The experimental results described above are compared with the calculation by MatCalc. The heat treatment conditions in the experiment were slightly different from those employed in the optimisation procedures, the microstructural parameters and strengthening effects were re-calculated with the condition which simulated the actual experimental conditions. Table 5.6 and 5.7 show the calculated results for the microstructure and strengthening effect on Fe-opt and 718Plus aged at 750 °C for 400 hours, respectively. Figure 5.12 compares the experimental and calculated γ' size distributions of these alloys aged at 750 °C for 400 hours. The experimental results showing both Fe-opt and 718Plus contain a high amount of γ' (Figures 5.6 and 5.7) are supported by the calculation, which indicates that the volume fraction of γ' in these alloys is nearly 20%. The TEM images, which show that γ' in Fe-opt is smaller than that in 718Plus are also equivalent to the calculation although there is a small difference in the absolute values. The experimental fact that the size range of γ' in Fe-opt is slightly narrower than that of 718Plus is also indicated in the calculation.

In the experiment, γ'' is not observed in both alloys, which is in accordance with the calculation. By comparing the experimental investigation and the calculation for Fe-opt, the difference lies in the existence of coarse precipitates (Laves phase) that are observed in the actual observation and are not considered in the calculation. Interestingly, the δ phase, which is predicted in the calculation for 718Plus, is hardly observed in any experimental microstructure analysis in this study.

As for strengthening effects, the calculation indicates that the precipitation strengthening by the APB effect is the primary strengthening mechanism in both Fe-opt and 718Plus. The calculation suggested that the strengthening by the APB effect in Fe-opt exceeded that in the reference material, which is supposed to stem from the high APB energy of γ'. Due to the large quantity of the precipitation strengthening, the designed alloy is predicted to have a higher yield stress than 718Plus. However, the experimental tensile test indicates that the yield stress of Fe-opt after 400-hour ageing is almost the same as that of 718Plus after the same ageing condition. Furthermore, the experimental yield stress of Fe-opt is much smaller than the calculated value.

According to Figures 5.3, the mean grain diameter of Fe-opt is roughly 120 μm, whereas 20 μm was input as the mean grain size in the strength estimation. The difference is supposed to influence on the accuracy of the yield strength. The grain size strengthening is estimated as

Table 5.6 Microstructural parameters calculated for Fe-opt and 718Plus aged at 750 °C for 400 hours.

	γ'			γ''		η		δ		$M_{23}C_6$	
	$f_{\gamma'}$ /%	$r_{\gamma'}$ /nm	E_{apb} /J·m^{-2}	$f_{\gamma''}$ /%	$l_{\gamma''}$ /nm	f_η /%	r_η /nm	f_δ /%	r_δ /nm	$f_{M_{23}C_6}$ /%	$r_{M_{23}C_6}$/nm /nm
Fe-opt	18.8	30.0	0.4	0	0.95	0.18	391	0	-	0.21	341
718Plus	19.3	43.4	0.29	0.12	1.01	0	-	6.3	1776	0.65	681

Table 5.7 Degree of strengthening effects calculated by MatCalc and both calculated and experimental yield stress for Fe-opt and 718Plus aged at 750 °C for 400 hours.

	σ_{ss}	σ_{gs}	σ_{gp}		σ_{dp}		σ_{pr}	Yield stress (Calc.)	Yield stress (Experim.)
			APB	Orowan	Coherency	Orowan			
Fe-opt	92	234	636	828	2	233	636	962	794
718Plus	112	234	447	555	33	3676	448	794	779

234 and 155 MPa, when the mean grain size is 20 and 120 μm, respectively. The yield stress of Fe-opt re-estimated with the grain size strengthening of 155 MPa is 883 MPa, which is closer to the experimental yield stress (794 MPa) than the initial estimation. Although the grain size explains the discrepancy between the calculation and the experimental results to some extent, there is still a gap (about 90 MPa) between the calculated and experimental yield stress.

Another substantial difference between the calculation and experiment laid in the Laves phase. The lower yield stress in the experiment might be caused by the coarse Laves phase, which has a negative influence in terms of the volume fraction of γ' because Nb and Ti, which are γ' formers, are consumed in the Laves phase. The Laves might have a negative effect on the precipitation strengthening by also lowering the APB energy, as the Laves phase contains a high amount of Nb, which usually increases the APB energy of γ'. In addition, W in the alloy might not have been as effective as expected for the solid solution strengthening, because the high amount of W is consumed in the Laves phase.

Based on the discussion above, W, which promotes the Laves phase during ageing in the designed alloy, does not work as expected and might have the negative influence on the strength after the long-time ageing, although the alloy is still expected to have a high potential for its elemental costs. For understanding the effect of W in the alloy, an alloy with the same chemical composition of Fe-opt except that it does not contain any W is produced and investigated. Reducing W would also be expected to be beneficial by increasing the ductility of the alloy. The results will be presented in the next chapter.

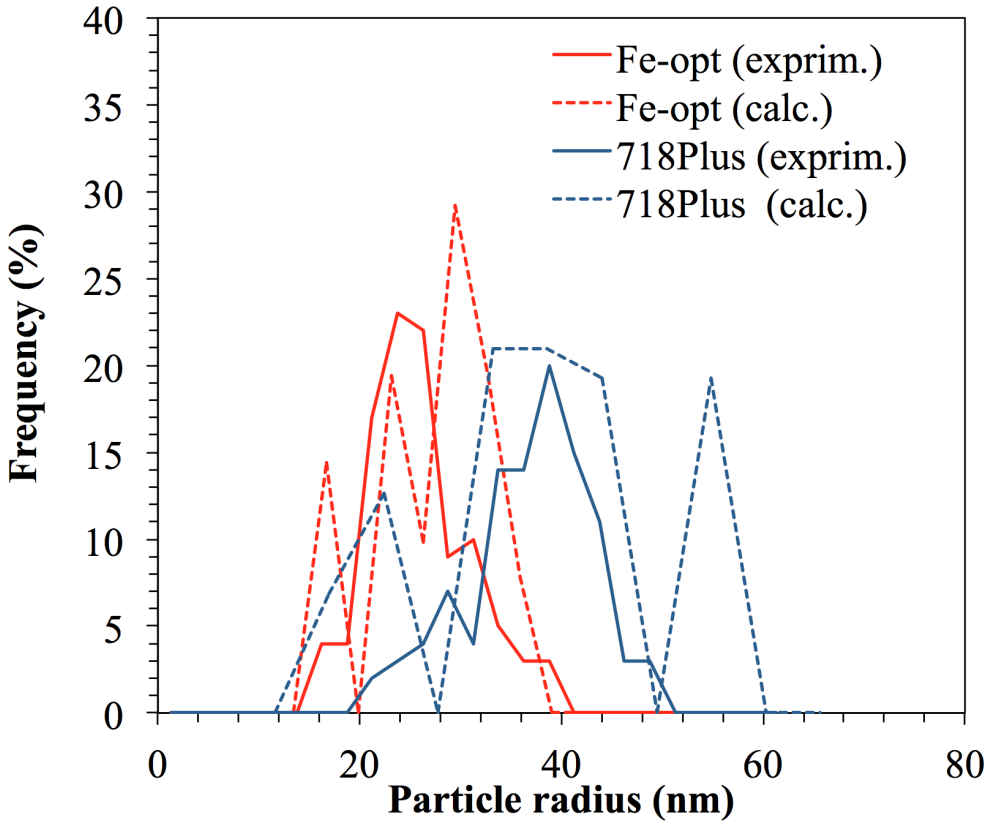

Fig. 5.12 Experimental and calculated γ' size distributions in Fe-opt and 718Plus aged at 750 °C for 400 hours.

5.4 Summary

The alloy sheet sample with the optimised chemical composition (Fe-opt) was produced by the middle-size ingot and compared with Alloy 718Plus, which was a newly developed high-temperature alloy strengthened by γ' particles. Experimental microstructure characterisation and mechanical tests were conducted for both alloy sheets after ageing treatment, which simulated the service as car sealing parts.

Fe-opt shows high yield stress after the ageing at 750 °C for 400 hours, which even slightly exceeds 718Plus. According to the microstructural characterisation, the large amount of fine γ' seems to be the primary strengthening media in both Fe-opt and 718Plus. However, the yield stress of Fe-opt is not as high as estimated by the combination of MatCalc calculation and classical strengthening theories. Based on the comparison between the experiment and calculation, it is concluded that a large amount of Laves phase containing W and Nb, which is not considered in the calculation, might have the negative influence of the alloy by reducing the volume fraction and the APB energy of the strengthening precipitates (γ'). In the next chapter, the experimental validation for the designed alloy without W is presented so that the influence of W is clarified.

Chapter 6

Experimental validation (2nd round)

In the previous chapter, the microstructure and mechanical properties of the designed alloy (Fe-opt) was validated using a sheet sample prepared by a process similar to the mass production for alloy sheets (casting - hot forging - hot rolling - cold rolling - solutionising). The alloy is experimentally confirmed to have finely dispersed γ' particles precipitated in the matrix and the high yield stress after a long-time high-temperature exposure. Yet, the alloy contains a large quantity of Laves phase on the grain boundaries, which was not considered in the alloy design calculations. Moreover, the yield stress is not as high as it is designed to be. Although the difference in grain size between the calculation and experiment explains the discrepancy to some extent, the Laves phase containing high amounts of W and Nb has a large influence on the yield stress by retarding the formation of γ', primary strengthening precipitate. So, it is suggested that the strength of the alloy after ageing might improve by reducing the W content.
Based on the results described in the last chapter, the alloy with the same chemical composition of Fe-opt (except that it did not contain any W) was cast and processed into an alloy sheet. This chapter explains how the microstructure and properties of the alloy are changed by reducing W. The alloy whose chemical composition was the same as Alloy 718Plus with the exception that the W content was reduced from 1 mass% to 0, was also prepared and used as reference material for understanding the influence of W.

6.1 Experimental procedures

Table 6.1 shows the chemical composition of the designed and reference alloys: Fe-opt and 718Plus, and those without W (hereinafter, they are called Fe-opt2 and 718Plus2, respec-

tively). The alloy sheet of 0.4 mm in thickness was prepared through the same process as described in the previous chapter. First, 25 kg ingots were cast by a vacuum induction melting furnace. The ingots were ground and soaked at 1100 °C for 2 hours and hot forged into slabs of 45 x 100 x 400 mm^3 in thickness, width and length, respectively. The slabs were reheated at 1150 °C for 1 hour and hot rolled by 3 rolling passes to 4 mm in thickness. The hot rolled sheets were repeatedly heat treated and cold rolled to obtain cold rolled sheets whose thickness was 0.4 mm. The sheets were solutionised at 1100 °C for 30 minutes subsequently water quenched to the room temperature and aged at 750 °C for 4, 20, 100 and 400 hours. It is worth mentioning that there were no cracks on the edge of both hot-rolled and cold-rolled sheets of Fe-opt2 and 718Plus2.

The microstructure analysis (OM, SEM, TEM) and mechanical testing (Vickers hardness test, tensile test at room temperature) were conducted by the same procedure written in the previous chapter.

For understanding the microstructure of these alloys, equilibrium and kinetic calculations were performed. As for the equilibrium calculation, MatCalc and Thermo-calc were used. For the kinetic calculation, MatCalc was used with thermodynamic and diffusion databases. The calculation details are shown in the discussion section later.

Table 6.1 Chemical composition of the designed and reference alloys (mass%).

	C	Si	Mn	P	S	Cu	Ni	Cr	Mo	V	Nb	Al	Ti	B	W	Co	N
Fe-opt	0.010	0.08	0.10	0.016	0.001	0.01	32.8	15.5	0.01	0.01	0.32	1.59	2.84	0.0020	3.74	0.89	0.0013
Fe-opt2	0.010	0.11	0.11	0.017	0.001	0.01	33.1	15.5	0.05	0.02	0.37	1.60	2.88	0.0019	-	0.86	0.0032
718Plus	0.021	0.09	0.10	0.015	0.001	0.01	52.2	18.1	2.75	0.01	5.34	1.48	0.73	0.0020	1.06	9.03	0.0035
718Plus2	0.020	0.12	0.11	0.014	0.001	0.01	51.9	18.0	2.81	0.01	5.31	1.48	0.71	0.0016	-	9.02	0.0043

6.2 Experimental result

6.2.1 Microstructure characteristics

Figures 6.1 and 6.2 show the OM images of Fe-opt2 and 718Plus2 (solutionised at 1100 °C for 0.5 hour, aged at 750 °C for 4, 20, 100 and 400 hours), respectively. Contrary to the microstructure of Fe-opt (with W), that of Fe-opt2 (without W) contains a smaller amount of large precipitates on the grain boundaries, although there are some after the ageing for 400 hours. On the other hand, any large difference is not confirmed between 718Plus and 718Plus2 (with and without W) and both alloys rarely contain large precipitates, as far as observed by the OM. It is worth noting that the mean grain size of Fe-opt2 and 718Plus2 are smaller than those of Fe-opt and 718Plus. Considering the volume fraction of precipitates on the grain boundaries in Fe-opt2 is smaller than that of Fe-opt, the grain boundary pinning effect from the precipitates is supposed to be small in these alloys. The experimental error in the heating temperature may be one of the causes of the difference in the mean grain size between the first and second validation samples, although further investigation is required.
Figures 6.3 and 6.4 show the SEM images of Fe-opt2 and 718Plus2, respectively. The results of the chemical composition analysis by SEM-EDS are summarised in Table 6.2. The appearance is very similar to those observed by the OM and some large precipitates are confirmed on the grain boundary when the alloys are aged for a long time. It is difficult to identify the precipitates on the grain boundary as the chemical composition of the matrix and the precipitate measured by the SEM-EDS are nearly the same, which is probably due to the spatial resolution of the EDS attached to the SEM.

Table 6.2 SEM-EDS chemical composition analysis results for coarse precipitates observed in Fe-opt2 and 718Plus2 aged at 750 °C for 400 hours (the location signs, such as "m1" refer to Figures 6.3 and 6.4).

Element	Fe-opt2		718Plus2	
	m1	p1	m1	p1
Al	3.63	4.35	3.75	3.81
Si	0.43	0.6	0.64	0.64
Nb	-	-	3.25	5.01
Mo	-	-	1.62	1.73
Ti	3.62	4.43	0.93	1.12
Cr	16.06	14.02	18.76	17.25
Mn	-	-	0.09	0.17
Fe	44.63	40.78	11.04	10.07
Co	-	-	9.47	8.74
Ni	31.48	35.69	50.45	51.45

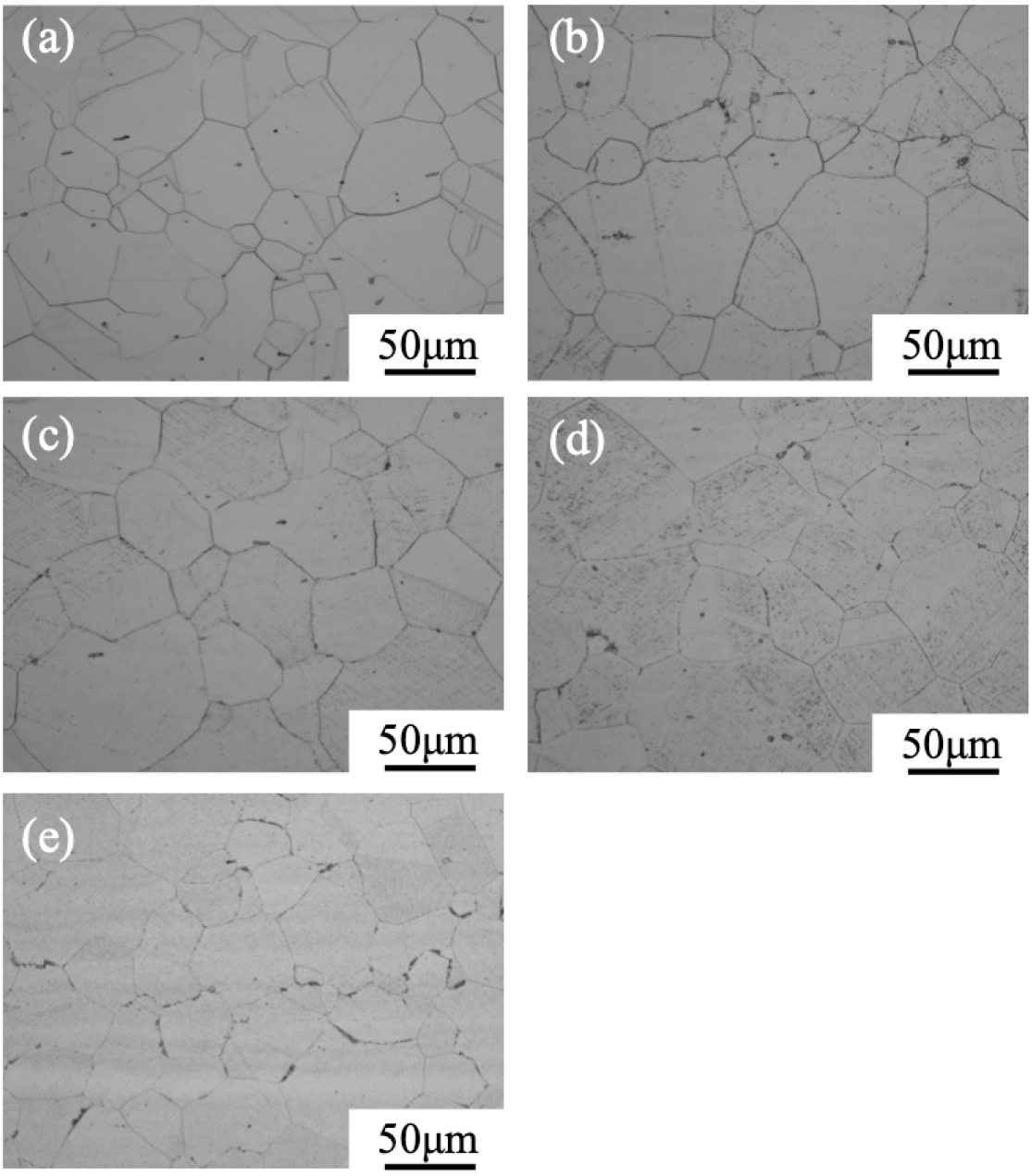

Fig. 6.1 Optical micrographs of the cross-section perpendicular to the rolling direction of Fe-opt2. The specimens were (a) solutionised at 1100 °C for 0.5 hour, aged at 750 °C for (b) 4, (c) 20, (d) 100, and (e) 400 hours.

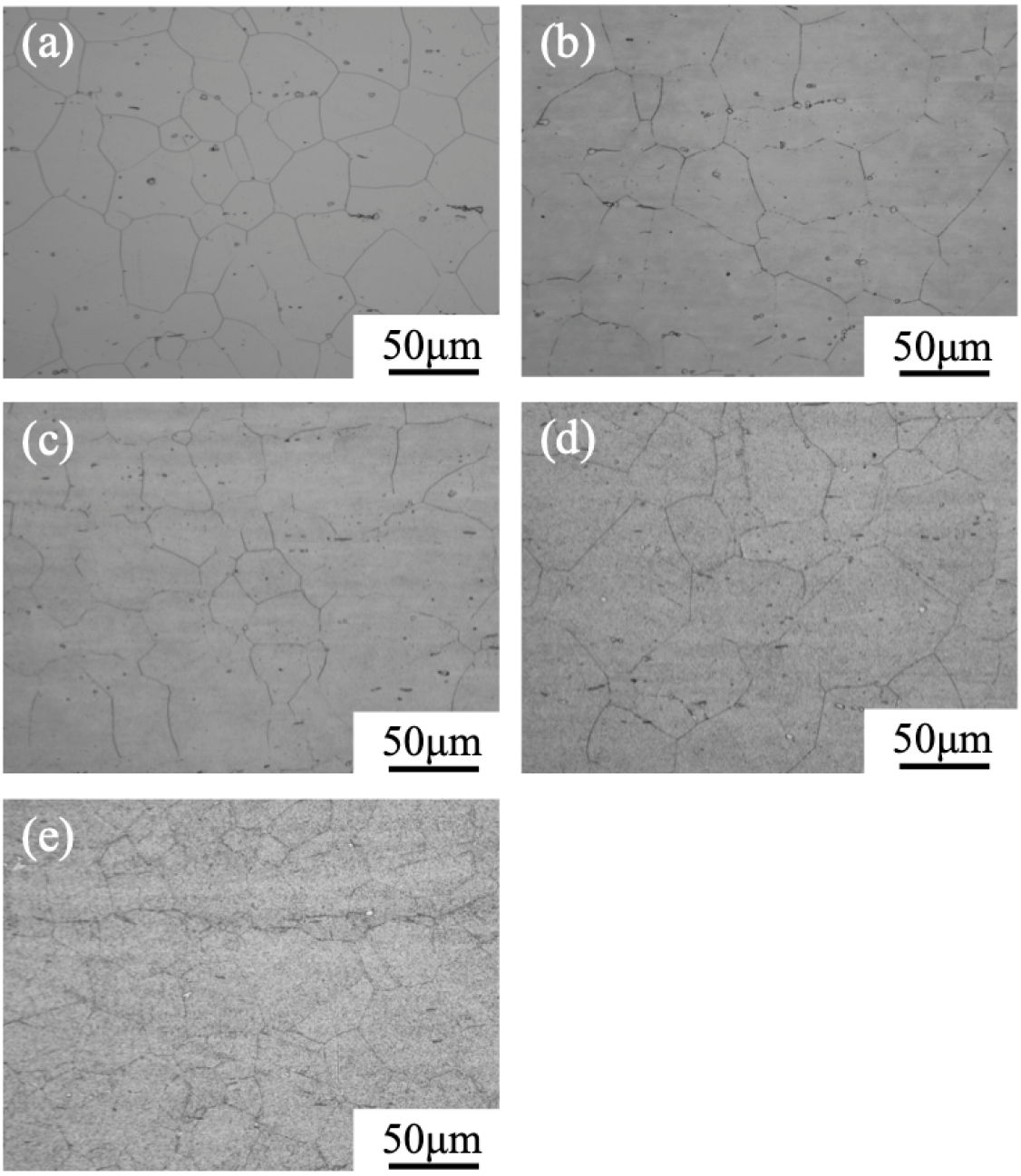

Fig. 6.2 Optical micrographs of the cross-section perpendicular to the rolling direction of 718Plus2. The specimens were (a) solutionised at 1100 °C for 0.5 hour, aged at 750 °C for (b) 4, (c) 20, (d) 100, and (e) 400 hours.

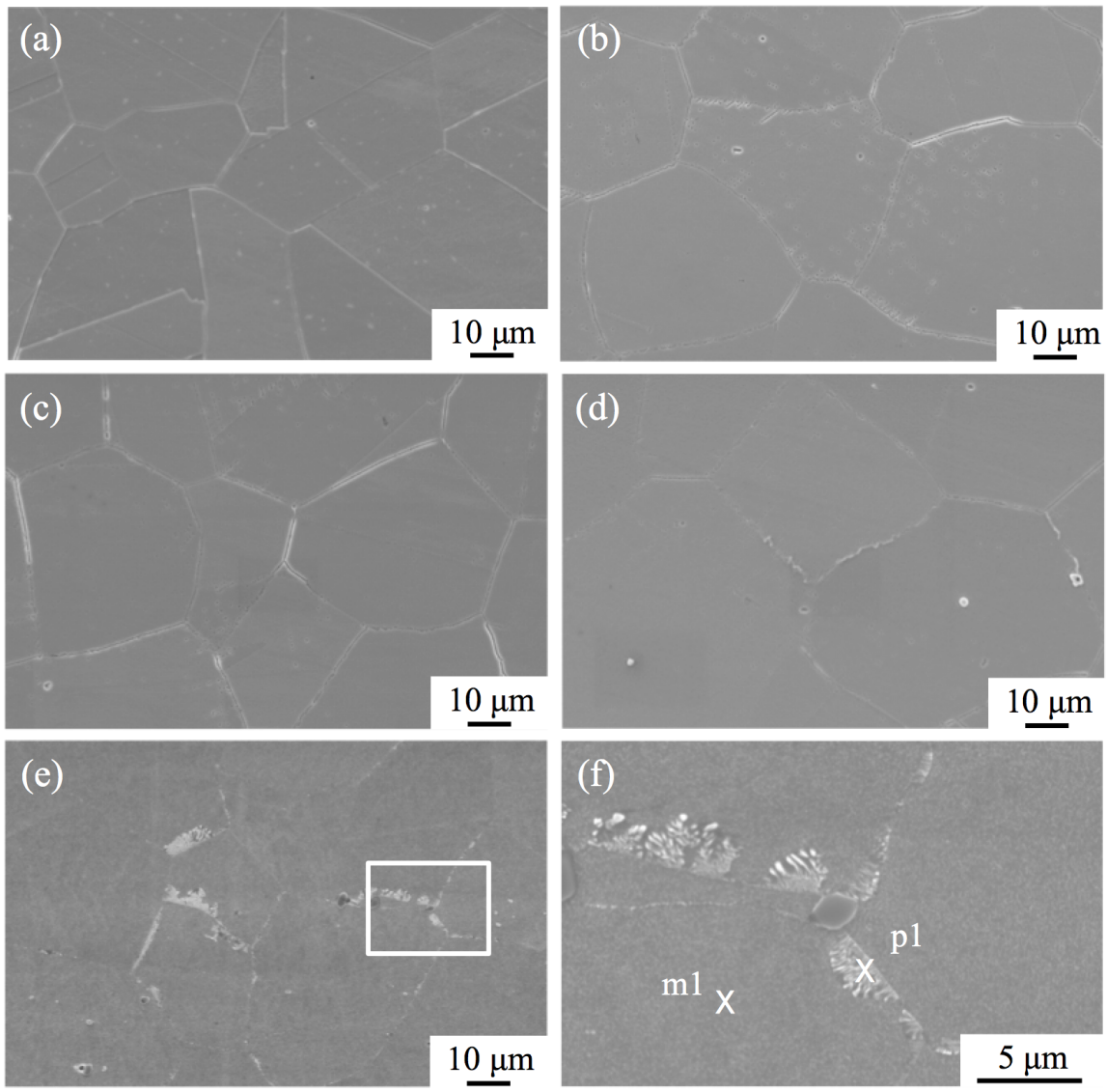

Fig. 6.3 SEM images of the cross-section perpendicular to the rolling direction of Fe-opt2. The specimens were solutionised at 1100 °C for 0.5 hour (a), aged at 750 °C for 4 (b), 20 (c), 100 (d) and 400 hours (e and f).

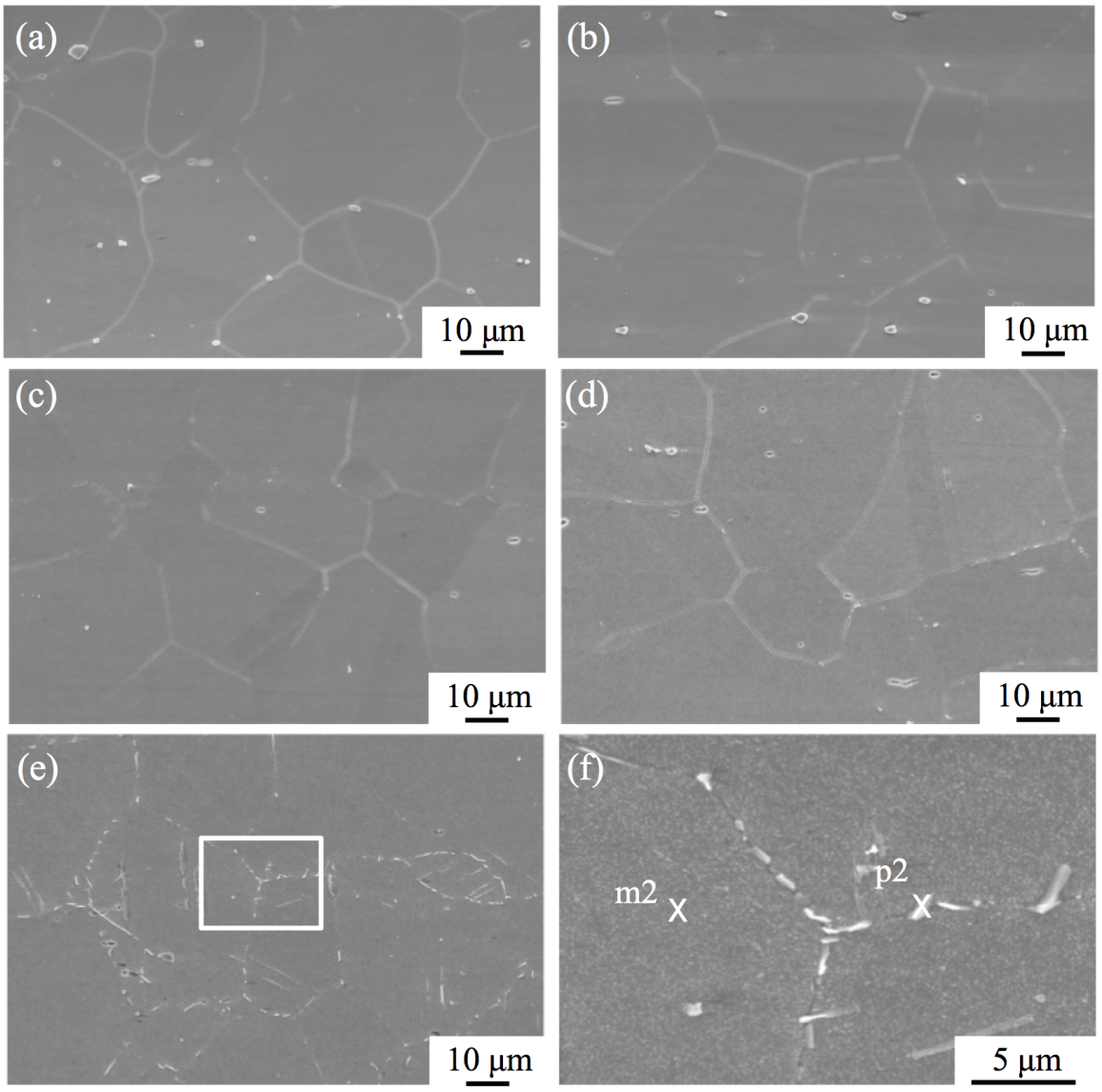

Fig. 6.4 SEM images of the cross-section perpendicular to the rolling direction of 718Plus2. The specimens were solutionised at 1100 °C for 0.5 hour (a), aged at 750 °C for 4 (b), 20 (c), 100 (d) and 400 hours (e and f).

As the resolution of the SEM used in this study was not high enough to observe fine precipitates in these alloys, the TEM analysis was conducted. Figures 6.5 and 6.6 show the transmission electron micrographs of the fine precipitates observed in Fe-opt2 and 718Plus2 aged at 750 °C for 400 hours. Both materials contain fine precipitates dispersed in the matrix and they are identified as γ' by the diffraction patterns, which are the same as the fine precipitates observed in Fe-opt and 718Plus (both contained W). The average radii of γ' in Fe-opt2 and 718Plus2 are 23 and 36 nm, respectively. As shown in Figure 6.7, the distributions of γ' are uni-modal, which is the same as those of Fe-opt and 718Plus. The shape of γ' in Fe-opt2 is spherical whereas that of 718Plus2 is the intermediate shape between spherical and cuboidal. The size and morphology of γ' in these alloys are nearly the same as their counterparts without W (the radius of γ' in Fe-opt and 718Plus are 24 and 35 nm, respectively), which indicates that W in these alloys does not have a significant influence on the size and morphology of γ'.

The coarse precipitates observed on the grain boundaries of Fe-opt2 and 718Plus2 were also analysed by the TEM-EDS. Figures 6.5 and 6.6 show the bright field images and the diffraction patterns of the coarse precipitates in these alloys. The chemical compositions of the precipitates measured by the EDS attached to the TEM are summarised in Table 6.3. The coarse precipitates in Fe-opt2 are identified as FeTiP. The Laves phases, which precipitates in Fe-opt, are not observed. As shown in the OM and SEM images, the total fraction of the coarse precipitates is substantially decreased by reducing the amount of W added in the alloy. This is mainly due to the suppression of the Laves phase formation. Contrary to the designed alloys (Fe-opt and Fe-opt2), the coarse precipitates in 718Plus2 are identified as P phase, which is also observed in 718Plus.

Table 6.4 is a summary of the precipitates observed in Fe-opt, Fe-opt2, 718Plus and 718Plus2. γ' is the primary second phase precipitated in the matrix of both Fe-opt and Fe-opt2. On the grain boundaries, the Laves and σ phase precipitate in Fe-opt, whereas FeTiP is observed in Fe-opt2. On the other hand, in 718Plus and 718Plus2, γ' and P phase are the precipitates formed in the matrix and the grain boundaries, respectively, regardless of the presence of W in the alloys.

Table 6.3 TEM-EDS chemical composition in atomic percent of coarse precipitates observed in Fe-opt2 and 718Plus2 aged at 750 °C for 400 hours (the precipitates (a) and (c) in Fe-opt2 and 718Plus2 refer to Figures 6.8 and 6.9 , respectively).

Element	Fe-opt2		718Plus2	
	(a)	(c)	(e)	(g)
Ni	11.73	14.02	25.36	22.41
Co	-	-	11.47	9.24
Fe	22.91	27.44	8.78	7.93
Cr	-	5.11	16.98	13.46
Si	-	-	1.76	1.62
V	0.54	-	-	-
Nb	10.97	8.48	15.9	26.46
Mo	-	-	17.75	16.01
Ti	27.67	24.14	-	0.97
P	26.18	20.81	2.01	1.91

Table 6.4 Summary of the phases precipitated in Fe-opt, 718Plus, Fe-opt2 and 718Plus2 during ageing treatment at 750 °C for 400 hours.

Alloy	precipitate	site
Fe-opt (with W)	γ'	matrix
	Laves	grain boundaries
	σ	grain boundaries
Fe-opt2 (without W)	γ'	matrix
	FeTiP	grain boundaries
718Plus (with W)	γ'	matrix
	P phase	grain boundaries
718Plus2 (without W)	γ'	matrix
	P phase	grain boundaries

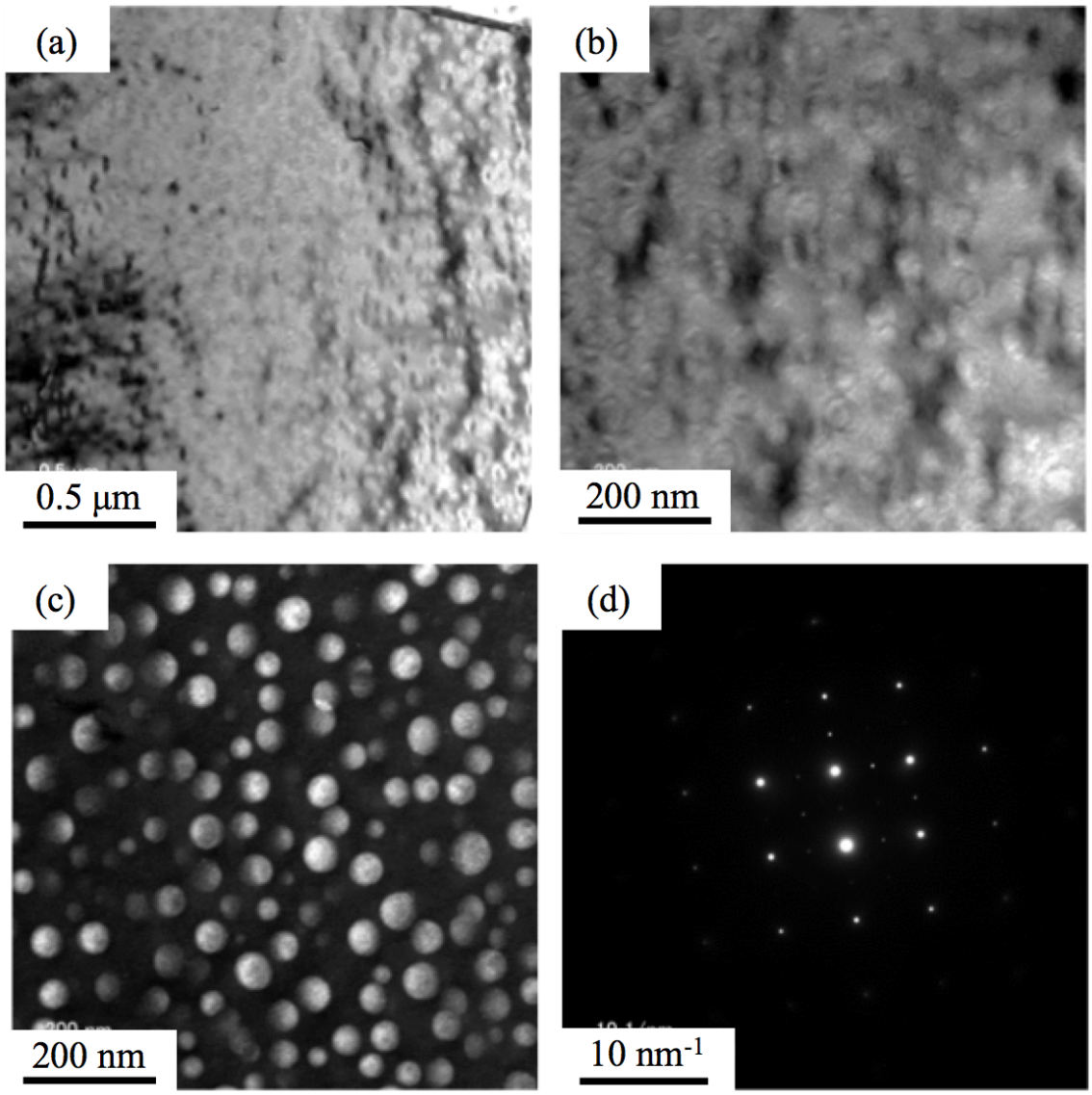

Fig. 6.5 TEM images of fine precipitates in Fe-opt2. Pictures (a) and (b): bright field images, (c): dark field image and (d): diffraction pattern.

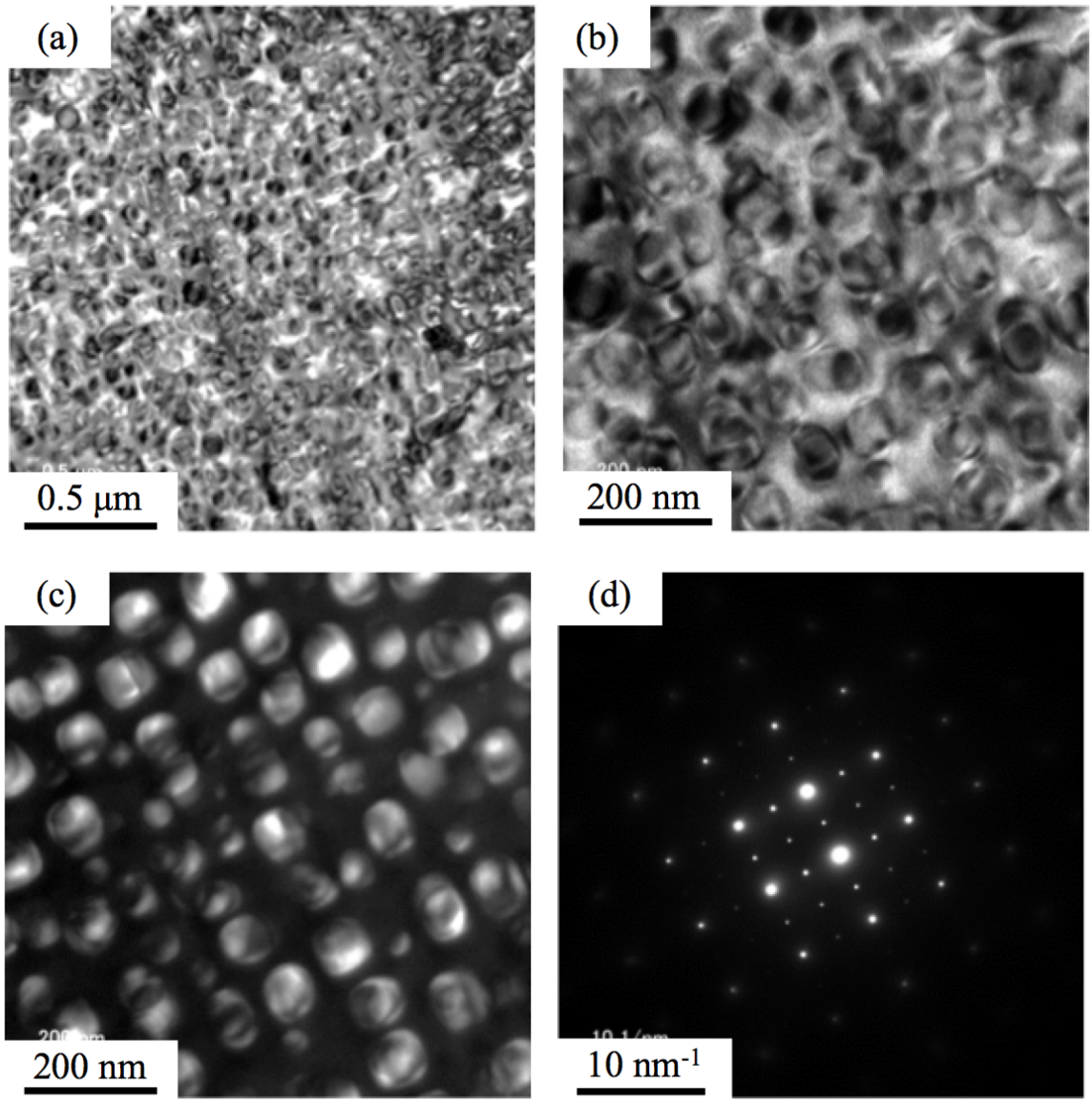

Fig. 6.6 TEM images of fine precipitates in 718Plus2. Pictures (a) and (b): bright field images, (c): dark field image and (d): diffraction pattern.

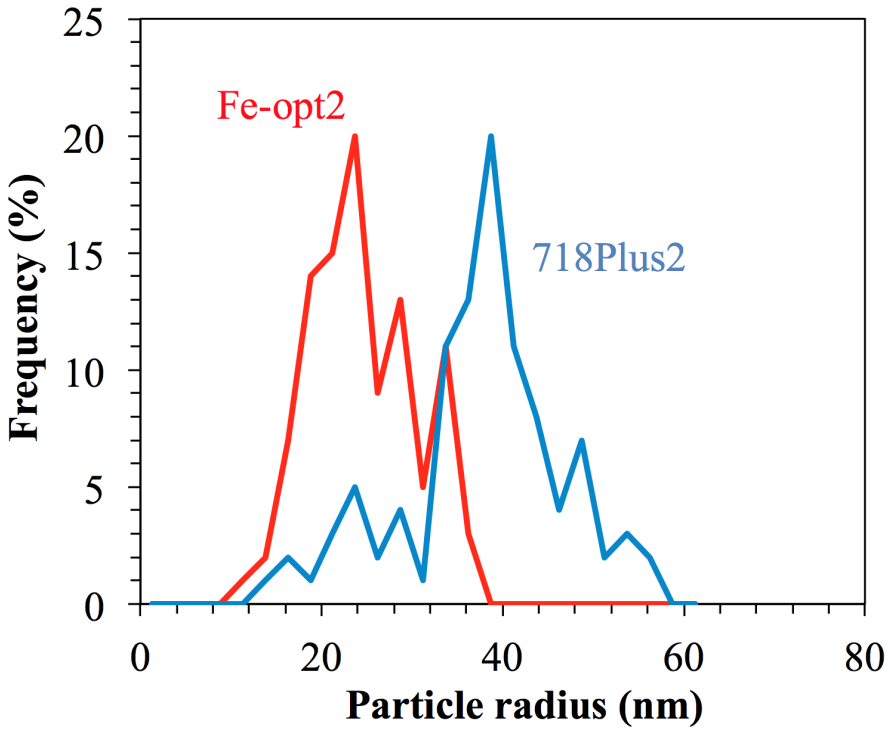

Fig. 6.7 γ' size distributions in Fe-opt2 and 718Plus2 aged at 750 °C for 400 hours measured from TEM images.

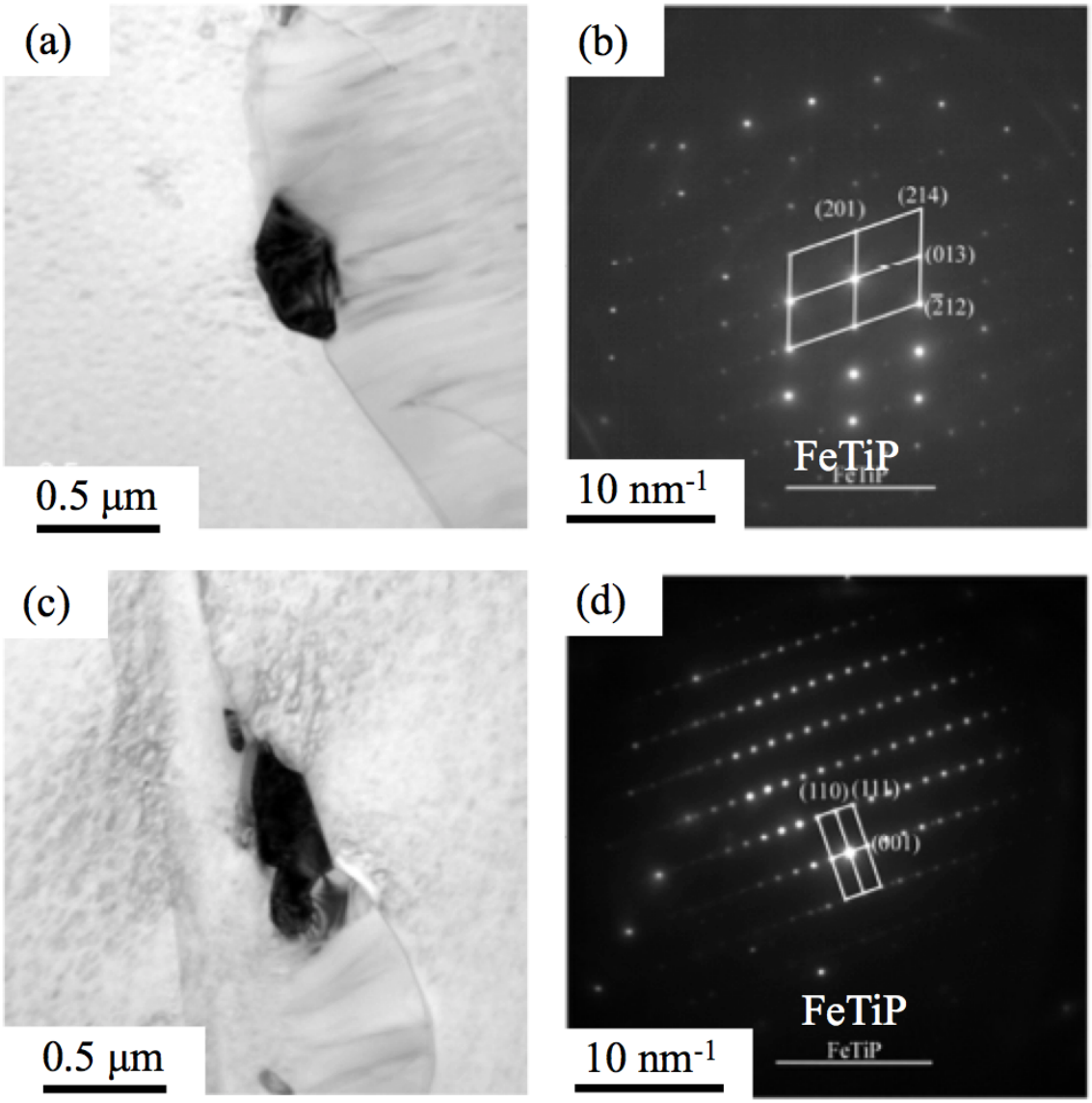

Fig. 6.8 TEM images of coarse precipitates in Fe-opt2 aged at 750 °C for 400 hours. Pictures (a) and (c): bright field images and (b) and (d): diffraction patterns.

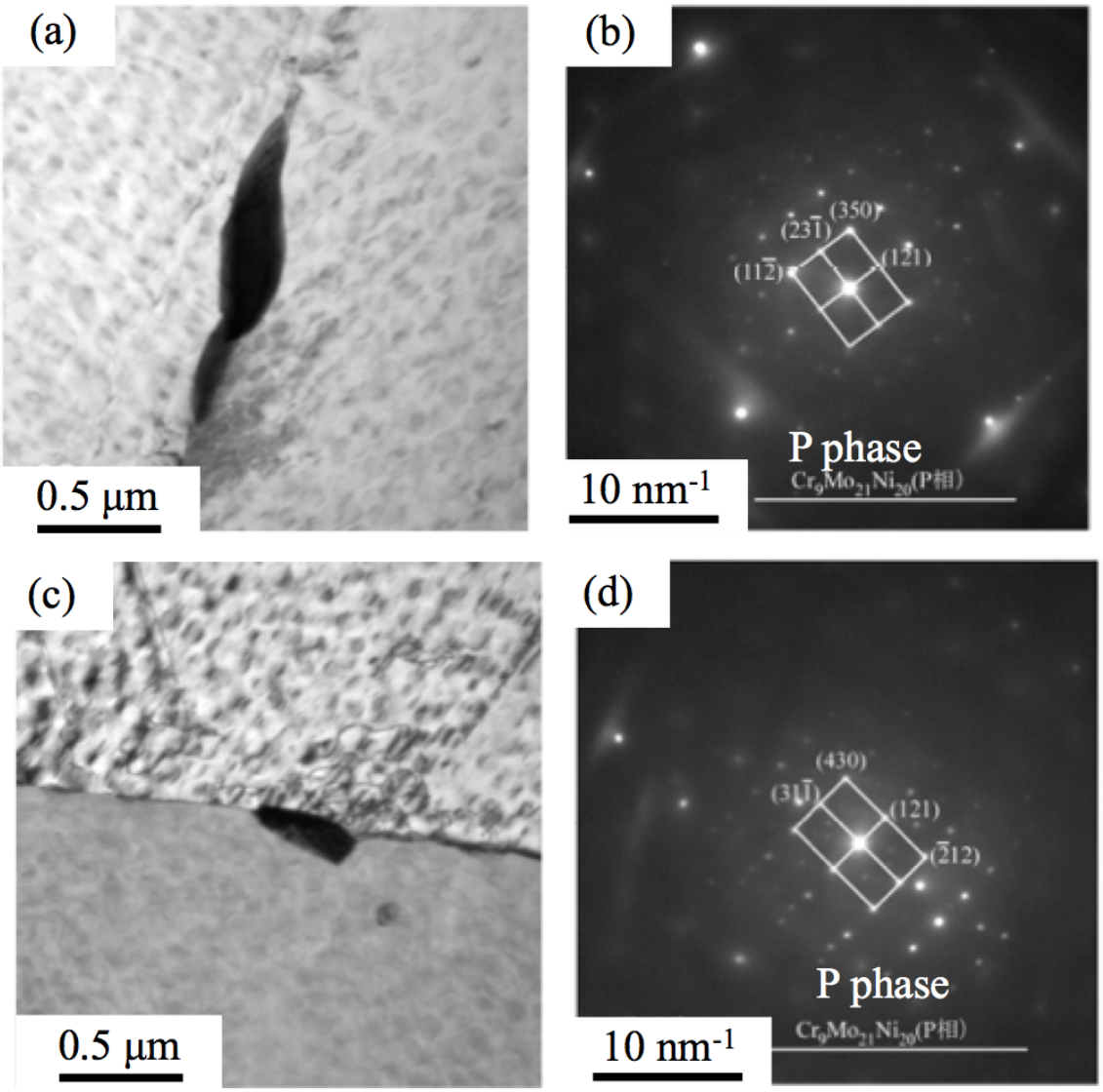

Fig. 6.9 TEM images of coarse precipitates in 718Plus2 aged at 750 °C for 400 hours. Pictures (a) and (c): bright field images and (b) and (d): diffraction patterns.

6.2.2 Mechanical properties

Figure 6.10 (a) shows the hardness of Fe-opt (3.0%W) and Fe-opt2 (without W) before/after ageing treatment at 750 °C for up to 400 hours. The initial hardness (as solutionised) of Fe-opt2 is slightly lower than that of the counterpart with W. This can be understood by the decrease in solid solution strengthening by W. The hardness of both alloys substantially increases by ageing for 4 hours and the hardness of Fe-opt2 is higher than Fe-opt when they are aged. As can be seen in Figure 6.10 (b), the yield stress of these alloys shows a similar tendency with the hardness and the difference in these two alloys after ageing is even larger. The tensile strength of Fe-opt2 (Figure 6.10 (c)) is also higher than that of Fe-opt after the ageing. The total elongation of these alloys (Figure 6.10 (d)) is nearly the same as long as the ageing time is 10 hours or less. As described in the last chapter, the elongation of Fe-opt decreases to a very low value when it is aged for 100 hours or longer. On the other hand, the elongation of Fe-opt2 after 100 or 400 hour ageing is higher than Fe-opt despite the fact that the strength of Fe-opt2 is higher than that of Fe-opt. By comparing the microstructure of Fe-opt and Fe-opt2, the high elongation of Fe-opt2 is supposed to stem from the absence of the coarse Laves phases on the grain boundaries, which is observed only in Fe-opt. Although the elongation after long duration ageing is not the principal property required in this study, the better ductility is generally beneficial for suppressing crack formation during service.
Considering that the original purpose of the present study was to develop an alloy with high yield strength after a long-time high-temperature exposure, Fe-opt2 has a higher potential for future use than Fe-opt. As W is a costly element, Fe-opt2 should be superior to Fe-opt also in terms of the material costs. It should be noted that the superiority of Fe-opt2 in the elemental cost can be more obvious if the cost is compared with that of Alloy 718 or 718Plus.
Figures 6.11 (a) to (d) respectively show the hardness, 0.2% yield stress, tensile strength and total elongation of 718Plus (1.0%W) and 718Plus2 (without W) as a function of ageing time at 750 °C for up to 400 hours. The values are also summarised in Table 6.5. The difference between the mechanical properties of these two alloys is not very large compared to the difference between Fe-opt and Fe-opt2, indicating that the influence of W in 718Plus and 718Plus2 on the mechanical properties is not substantial.

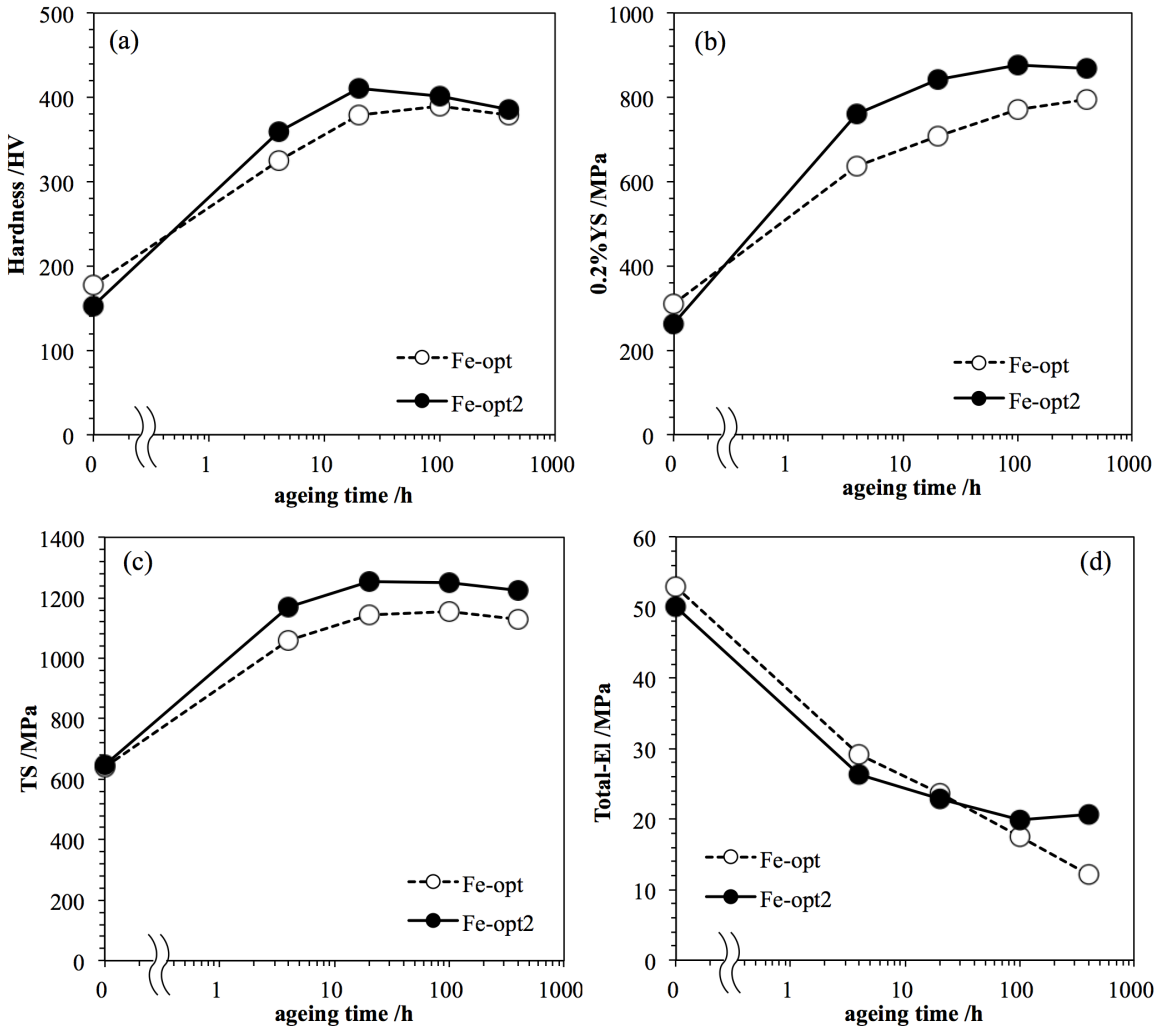

Fig. 6.10 Mechanical properties of Fe-opt (3.7%W) and Fe-opt2 (without W). (a): Vickers hardness, (b): 0.2% yield stress, (c): tensile strength and (d): total elongation.

Table 6.5 Mechanical properties of Fe-opt2 and 718Plus2 aged at 750 °C for up to 400 hours. YS, TS, t-El stand for the yield stress, tensile strength and total elongation at room temperature, respectively.

ageing	Fe-opt2				718Plus2			
/h	Hardness/HV	0.2% YS /MPa	TS /MPa	t-El /%	Hardness/HV	0.2% YS /MPa	TS /MPa	t-El /%
0	153	263	647	50	209	383	844	55
4	360	760	1169	26	407	852	1262	30
20	411	842	1254	23	415	877	1325	29
100	402	877	1251	20	415	839	1329	28
400	386	869	1224	21	404	835	1331	25

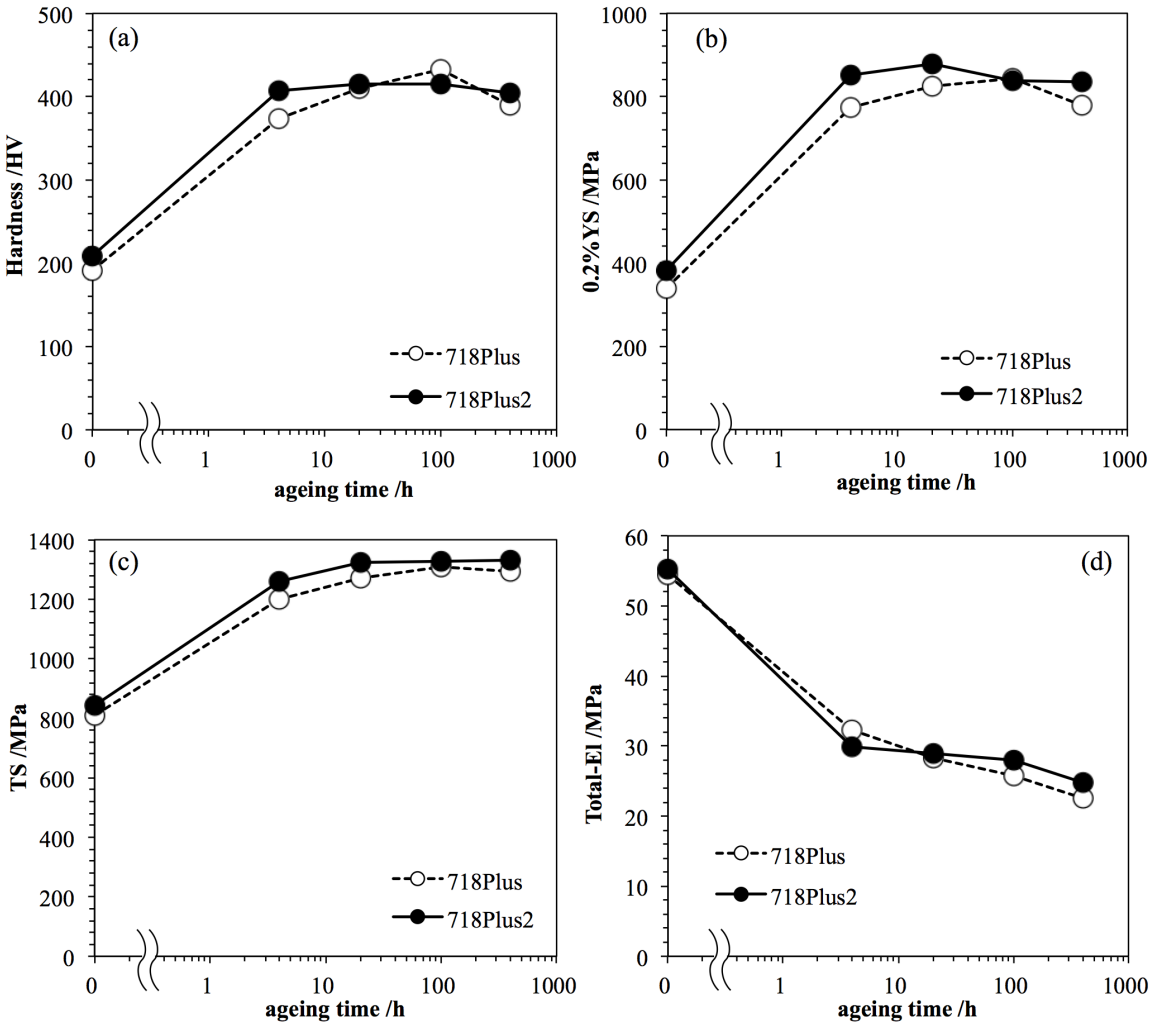

Fig. 6.11 Mechanical properties of 718Plus (1.0%W) and 718Plus2 (without W). (a): Vickers hardness, (b): 0.2% yield stress, (c): tensile strength and (d): total elongation.

6.3 Discussion

6.3.1 Relationship between microstructure and mechanical properties

As shown in Figure 6.10, the hardness and 0.2% yield stress of the solutionised Fe-opt2 is slightly lower than that of Fe-opt. On the other hand, the experiment results show that Fe-opt2 has the higher strength than Fe-opt after the ageing at 750 °C. The difference between aged Fe-opt and Fe-opt2 is the presence and absence of the coarse Laves phase on the grain boundaries. As these Laves phases contain W, Nb and Ti, it is suggested that the presence of Laves phase suppresses the formation of the strengthening precipitates: γ'. Hence, the lack of W in the chemistries leads to an increase in the strength after the ageing by maintaining a high fraction of γ'. It is also suggested that the amount of Nb and Ti in γ' is higher in Fe-opt2 than Fe-opt, leading to an increase in the anti-phase boundary energy of the precipitate [72]. Although the Laves phase itself might have strengthened the alloy, the influence in the strength should have been small as the Laves is large and coarsely dispersed.
As described in the previous section, the elongation of Fe-opt2 after 100 or 400 hour ageing is higher than Fe-opt in spite of the fact that the strength of Fe-opt2 is higher than the other. The advantage of Fe-opt2 against Fe-opt in the elongation after the exposure at a high temperature can be explained by the decrease in the coarse detrimental precipitates, such as the Laves phase. Although Fe-opt2 contains some FeTiP phase, which is sometimes observed in Ti- and Nb-added interstitial free high strength steels and leads to the deterioration of the ductility and the decrease in the strength [140], the fraction of the FeTiP phase in Fe-opt2 is much smaller than the fraction of the Laves phase in Fe-opt. Therefore, the negative influence of FeTiP on the properties of Fe-opt2 should be smaller than the positive influence of the absence of the Laves phase.
The difference in mechanical properties between 718Plus and 718Plus2 is not substantial. This is supported by the experimental results that the microstructures of these alloys are very similar to each other. Cao *et al.* have reported that addition of W has a positive influence on stress rupture life at high temperatures by reducing bulk diffusivity, which is one of the reasons W is added in Alloy 718Plus [28]. However, as far as seeing Figures 6.11, 1 mass% of W does not have a significant effect on the room temperature strength.

Table 6.6 Microstructural parameters calculated by MatCalc for Fe-opt, Fe-opt2, 718Plus and 718Plus2 aged at 750 °C for 400 hours.

	γ'			γ''		η		δ		$M_{23}C_6$	
	$f_{\gamma'}$ /%	$r_{\gamma'}$ /nm	E_{apb} /Jm^{-2}	$f_{\gamma''}$ /%	$l_{\gamma''}$ /nm	f_η /%	r_η /nm	f_δ /%	r_δ /nm	$f_{M_{23}C_6}$ /%	$r_{M_{23}C_6}$/nm /nm
Fe-opt	18.8	30.0	0.40	0	0.95	0.18	391	0	-	0.21	341
Fe-opt2	18.8	31.4	0.38	0	0.95	0.14	355	0	-	0.19	833
718Plus	19.3	43.4	0.29	0.12	1.01	0	-	6.3	1776	0.65	681
718Plus2	18.6	43.6	0.35	0.14	1.02	0	-	6.5	1830	0.65	794

6.3.2 Agreement between experiment and calculation

Table 6.6 shows the microstructure parameters calculated by MatCalc for Fe-opt, Fe-opt2, 718Plus and 718Plus2 aged at 750 °C for 400 hours. As shown in Figures 5.6, 5.7 (in the previous chapter), 6.5 and 6.6, all these alloys are experimentally confirmed to contain fine γ' particles in the matrix, which are also predicted in the calculation. Figure 6.12 shows the distribution of γ' of these alloys measured from TEM images and calculated with MatCalc (the comparison of experimental and calculated γ' size distribution of Fe-opt and 718Plus is shown in Figure 5.12 in the previous chapter). The average γ' radius in Fe-opt, Fe-opt2, 718Plus and 718Plus2 after the ageing measured from TEM images are 24, 23, 35 and 36, respectively, whereas the calculated γ' size are 30, 31, 43 and 44 nm, respectively. The experimental and calculated γ' size distribution are not the same (calculated γ' size is slightly larger than the experimental value in every case), but the experimental results that the size of the precipitate in Fe-opt and Fe-opt2 is smaller than that in 718Plus and 718Plus, and the precipitate size is not influenced very much by the amount of W in the alloys, are supported by the calculation.
In the TEM observation, any γ'' is not observed in any alloys investigated in this study, which also agrees well with the microstructure calculation. For η phase, both experiment and calculation show that the precipitate does not appear in these alloys even after the long-time ageing. Regarding the δ phase, it is not observed in 718Plus and 718Plus2, whereas the phase is predicted to precipitate in the calculation. A small amount of $M_{23}C_6$ is predicted to precipitate in all these alloys, they are not observed in any experimental microstructural observations carried out in this study.

Although it has been confirmed that the kinetic calculation carried out for the alloy design agrees with the experimental microstructure analysis to some extent, the Laves phase, which plays an important role for understanding the effect of W was not incorporated in this

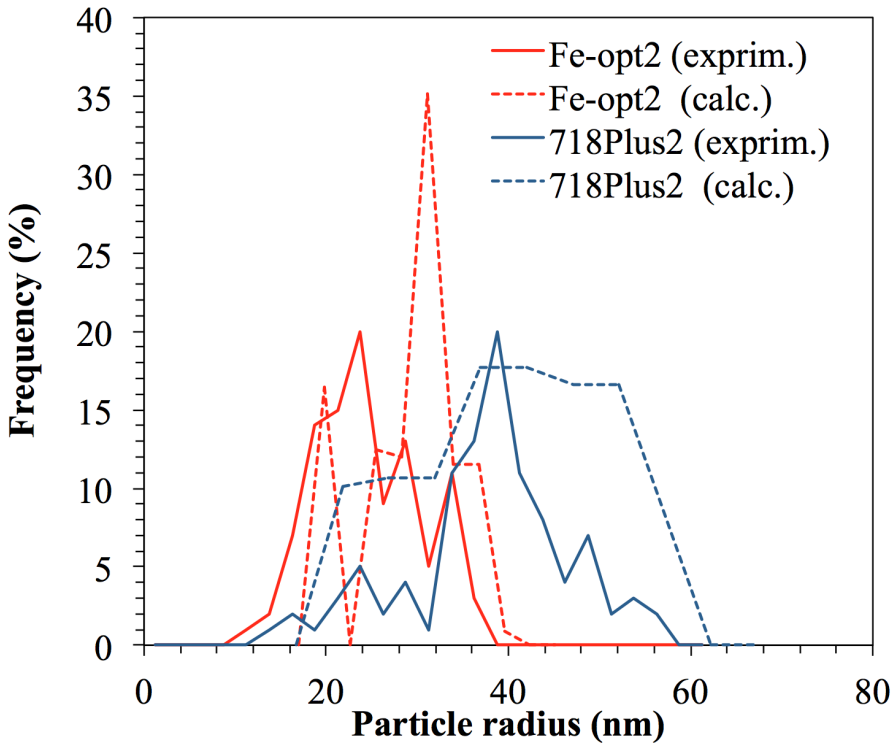

Fig. 6.12 Experimental and calculated γ' size distributions in Fe-opt2 and 718Plus2 aged at 750 °C for 400 hours.

alloy design. Therefore, calculations considering the Laves phase were conducted. Some equilibrium calculations were carried out using MatCalc and Thermo-calc before conducting the kinetic calculations. Figures 6.13 show the equilibrium phase fraction as a function of temperature in Fe-opt, Fe-opt2, 718Plus and 718Plus2 calculated by MatCalc. The thermodynamics database mc_ni_2.034 was used and γ', γ'', δ, η, δ, σ, Laves phase, P phase, MC and $M_{23}C_6$ were incorporated in the calculation. In Fe-opt (with W), γ', η and Laves phase are stable phases at the temperature around 750 °C. On the other hand, in Fe-opt2 (without W) γ' and η are the stable phases and the Laves phase does not appear. In the experimental microstructure analysis, the η phase is not observed in both Fe-opt and Fe-opt2 even after ageing at 750 °C for 400 hours, which indicates that it takes a very long time for η to form in these alloys. The equilibrium calculation and experimental microstructure analysis agree well at least qualitatively, except for the η phase.

The 718Plus's calculated equilibrium microstructure, shown in Figures 6.13 (c) and (d), is more complex. At 750 °C, γ', δ and η are stable and P phase also appears at the lower temperature. γ', δ and η are also stable in 718Plus2 (without W), whereas P phase does not appear. In the experiment, neither η and δ are observed even after 400 hour ageing, which is

reasonable as 718Plus is designed to have a small amount of these phases [28, 133].
The equilibrium calculations were carried out also by using Thermo-calc (TC) with Ni8 database. Figures 6.14 show the phase fraction of the four alloys. In TC calculation, γ', Laves phase and σ phase are stable in Fe-opt at 750 °C, which is consistent with the experimental result. It is confirmed that in the equilibrium calculations by both MatCalc and Thermo-calc, Laves phase appears at the temperature around 750 °C as a stable phase. However, the Laves phase was not incorporated in the kinetic microstructure parameter calculation, which was a part of the alloy design process in this study. So, a kinetic calculation was carried out again but the Laves phase was incorporated this time.
Figure 6.15 shows the fraction of phases in Fe-opt and Fe-opt2 calculated by MatCalc as the function of heating time. The databases mc_ni_2.034.tdb and mc_ni_2.007.ddb were used as thermodynamics and diffusion databases, respectively. The heat treatment incorporated in the calculation was twofold: the solutionising (1100 °C for 0.5 hour) and the following ageing (750 °C for 400 hours). The Laves phase was assumed to nucleate at the grain boundaries in the calculation. As shown in the Figure, the Laves phase does not appear in the kinetic calculation even after the 400 hour ageing, although several volume percent of the Laves phase is experimentally confirmed on the grain boundary of Fe-opt. The disagreement between the calculation and the experiment regarding the formation of Laves phase indicates that there must be a margin for improvement in the thermokinetic calculation model and databases for achieving more accurate prediction and more effective and efficient alloy design. However, it has been demonstrated, by combining the calculation and the experimental data obtained according to logical inference, the alloy can be designed more effectively than by conventional experiment-oriented alloy design approaches. The newly designed alloy, Fe-opt2, can be nominated as one of the alloys designed by the integrated approach described above.

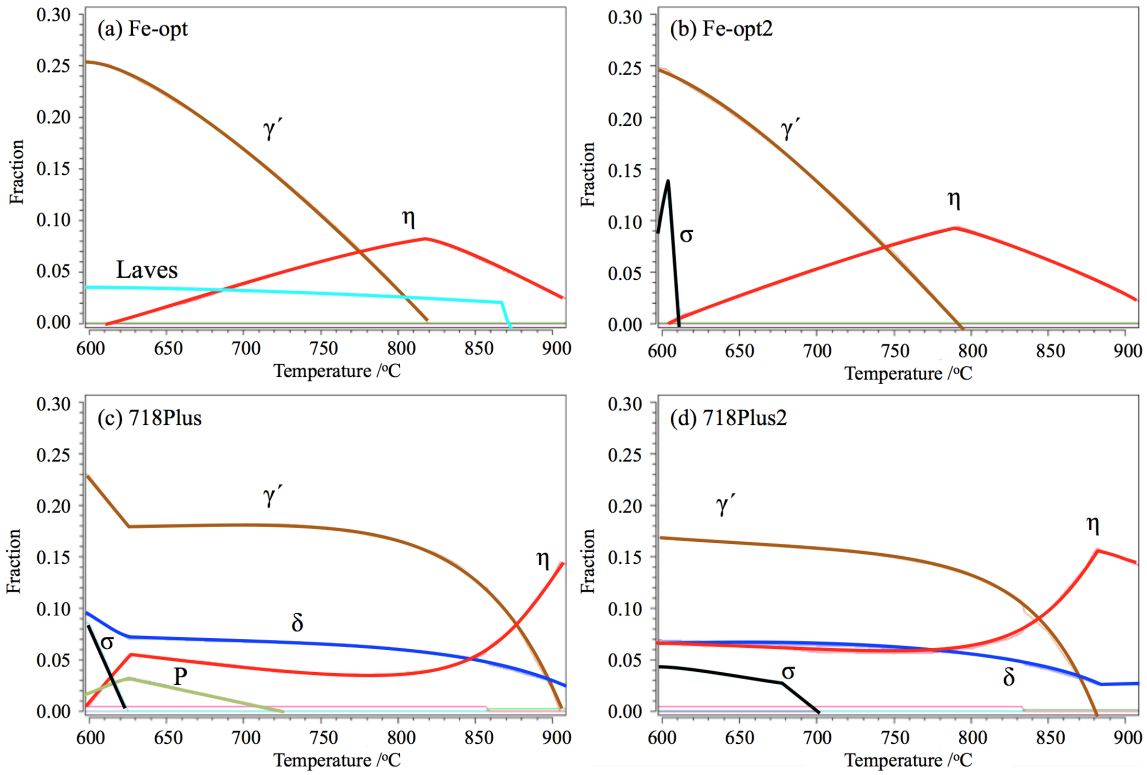

Fig. 6.13 Equilibrium phase fraction of (a) Fe-opt (with W), (b) Fe-opt2 (without W), (c) 718Plus (with W) and (d) 718Plus2 (without W) calculated by MatCalc (database: mc_ni_2.034.tdb).

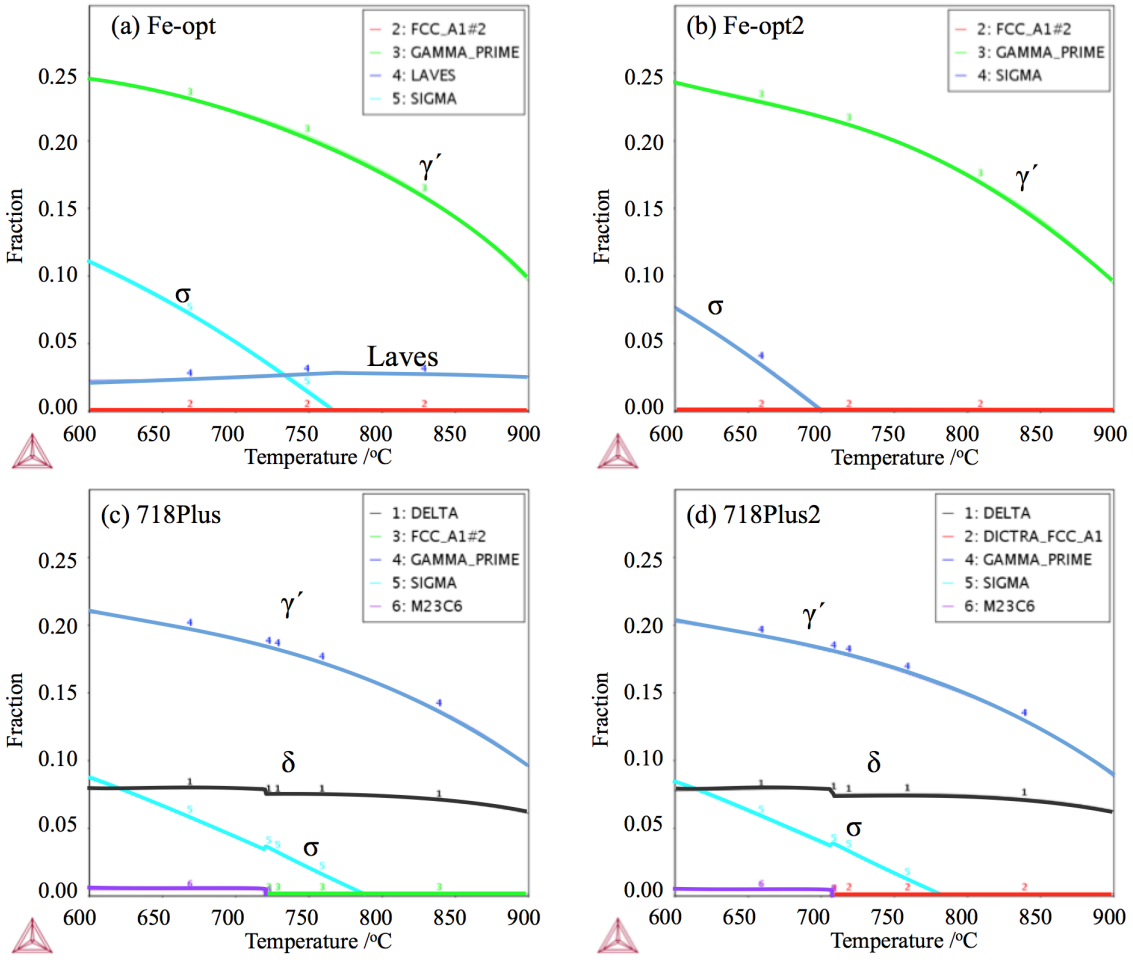

Fig. 6.14 Equilibrium phase fraction of (a) Fe-opt (with W), (b) Fe-opt2 (without W), (c) 718Plus (with W) and (d) 718Plus2 (without W) calculated by Thermo-calc (database: Ni8).

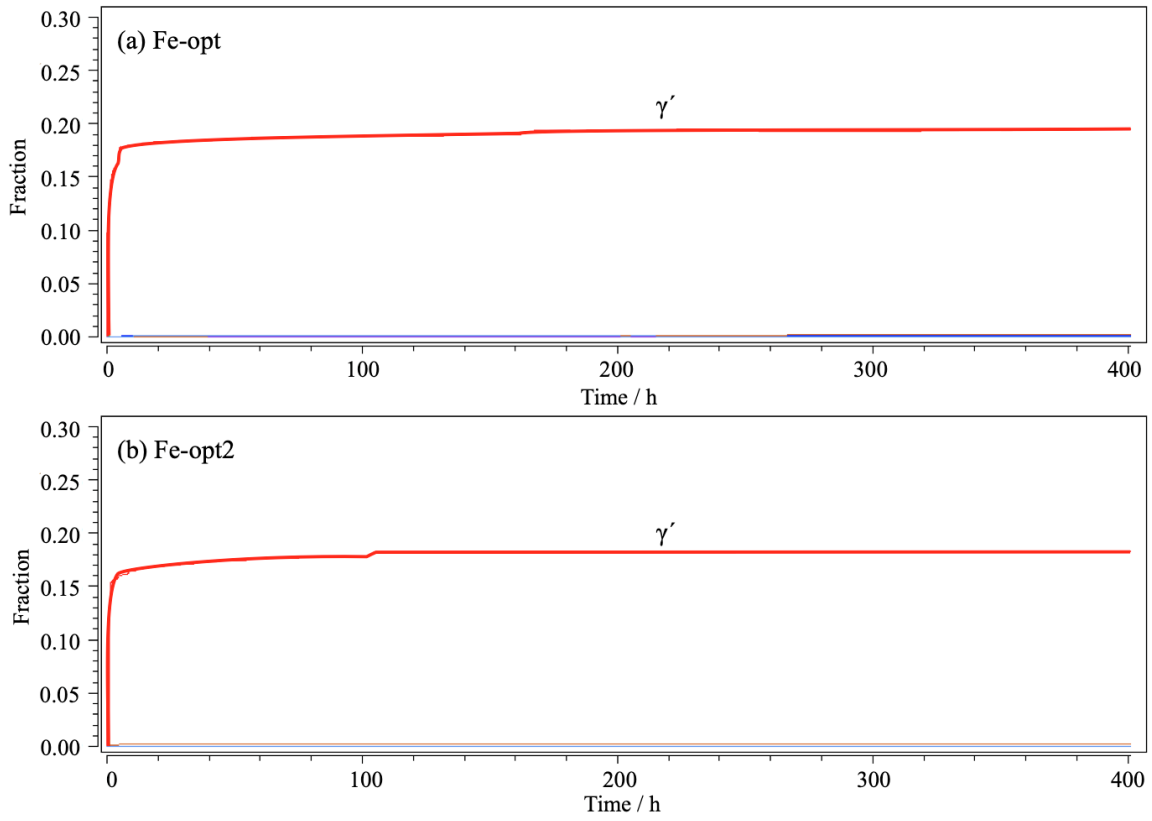

Fig. 6.15 Kinetically calculated phase fraction of (a) Fe-opt (with W) and (b) Fe-opt2 (without W) as a function of heat treatment time.

6.4 Cost-properties comparison

Table 6.7 shows the degree of strengthening estimated from microstructural parameters and both calculated and experimental yield stress of Fe-opt, Fe-opt2, Alloy 718Plus and Alloy 718Plus2 aged at 750 °C for 400 hours. The experimental yield stress of Fe-opt is much lower than the calculated value. It is concluded that the main cause of the discrepancy is the grain size difference between the calculation and the experiment and the presence of the Laves phases. On the other hand, the measured and calculated yield stress of Fe-opt2 shows a reasonable agreement. Assuming that the mean grain size of Fe-opt2 is 50 μm, the grain size strengthening and the yield strength are estimated as 185 and 868 MPa, respectively. The latter shows an excellent agreement with the experimental value of 869 MPa.
Table 6.8 summarises the elemental cost and experimentally measured mechanical properties of the alloys studied in this work. As can be seen in the table, Fe-opt2 has a higher strength after the ageing than any other alloy including Alloy 718Plus. The elemental cost of Fe-opt2 is half of the 718Plus and 2/3 of Alloy 718, which is another advantage in Fe-opt2. It is concluded that the integrated alloy design conducted in this study has successfully found a potential candidate according to the intended properties.
Although, in alloy design, required properties and constraints depend on many factors, *e.g.* the final application, customer, production process, employing the approach endeavoured in this study should be beneficial to develop the alloy efficiently and effectively. Further advancement in microstructure and property estimation models and progress of the database accuracy would even enhance the potential of the design approach by using calculations, which was exemplified by this work.

Table 6.7 Degree of strengthening estimated from microstructural parameters and calculated and experimental yield stress of Fe-opt, Fe-opt2, 718Plus and 718Plus2 aged at 750 °C for 400 hours. σ_{ss}, σ_{gb}, σ_{gp}, σ_{dp} and σ_{pr} represent solid solution, grain boundary and precipitation strengthening (effect of γ', γ'' and total), respectively.

	σ_{ss}	σ_{gb}	σ_{gp}		σ_{dp}		σ_{pr}	Yield stress (Calc.)	0.2%YS (Experim.)
			APB	Orowan	Coherency	Orowan			
Fe-opt	92	234	636	828	2	233	636	962	794
Fe-opt2	71	234	612	790	2	281	612	917	869
718Plus	112	234	447	555	33	3676	448	794	779
718Plus2	107	234	450	567	36	4017	451	792	835

Table 6.8 Elemental cost and mechanical properties of alloys studied in this work.

	Elemental cost /$kg^{-1}	Solutionised				Aged (750 °C, 400 h)[2]			
		Hardness /HV	0.2%YS /Nmm^{-2}	TS /Nmm^{-2}	t-El /%	Hardness /HV	0.2%YS /Nmm^{-2}	TS /Nmm^{-2}	t-El /%
Fe-opt	8.9	177	309	1060	53	380	794	1130	12
Fe-opt2	8.2	153	263	1169	50	386	869	1224	21
Alloy 718Plus	18.3	191	339	1200	55	390	779	1295	23
718Plus2 (without W)	18.1	209	383	1262	55	404	835	1331	25
Alloy 718 [1]	14.8	186				311			
Alloy 660 [1]	5.8	116				265			

[1] Alloy 718 and Alloy 660 were prepared from small ingots (details are in Chapter 4).

[2] Alloy 718 and Alloy 660 were aged at 720 °C for 16 hours before the ageing at 750 °C for 400 hours.

6.5 Summary

In this chapter, the microstructure and mechanical properties of the modified alloy (Fe-opt2), which was the same composition with the designed alloy except that it did not contain any W, was investigated. Fe-opt2 has a higher yield stress than the designed alloy with W (Fe-opt) and 718Plus after the ageing, which simulates the service in use. The Laves phase, which is observed on the grain boundaries of Fe-opt, does not precipitate in Fe-opt2, which leads to the increase in the strength by maintaining the higher fraction of fine γ' and keeping its anti-phase boundary energy. It should be mentioned that the elemental cost of Fe-opt2 is smaller than that of conventional Ni-based alloys including Alloy 718 and Alloy 718Plus as Fe-opt2 contained smaller amount costly elements, such as Ni, Nb, Co and W, than the conventional alloys.

Although this study has revealed that the accuracy of the microstructure prediction needs to be improved for more precise prediction, by combining the calculation and the logical inference from the experimental data, it is shown that the alloy can be designed more effectively than by stereotypical experiment-oriented alloy design approaches. Moreover, with the advancement of strengthening modelling and the accuracy of thermodynamic and diffusion databases, a calculation-aided alloy design would take over the conventional time- and cost- consuming alloy development approaches.

Chapter 7

Conclusions and future work

7.1 Conclusions

In this thesis, a challenging alloy design approach was endeavoured for the development of high-temperature alloy sheet that is applicable to a sealing part in car exhaust systems. For designing alloys, especially high-temperature alloys containing many elements and consisting of complex microstructure, conventional experiment-oriented approaches have often ended up without a fruitful outcome due to the innate difficulties. The alloy design approach investigated in this study consists of properties prediction and chemical composition optimisation. For properties prediction, microstructural parameters, such as the volume fraction and size of precipitates, after a certain heat treatment simulating a service as the sealing parts, were thermokinetically calculated by using a phase transformation calculator, MatCalc. The associated yield stress of alloys was then predicted from these microstructural parameters using classical strengthening theories: solid solution, grain boundary and precipitation strengthening. The precipitation strengthening was especially carefully incorporated into the strength prediction model by considering several effects depending on the size and species of the precipitates. For example, an anti-phase boundary effect (cutting mechanism) and Orowan effect (bowing mechanism) were both considered for strengthening by γ'. The change in anti-phase boundary energy by the chemistry of γ' was also incorporated in the model. The calculated microstructure parameters, such as the average radius of γ', and strength of several conventional high-temperature alloys were compared to the experimental values taken from literature. The overall agreement between the calculation and experimental measurement results was reasonable and confirmed that the prediction process employed in this study can be adopted to the new alloy design approach.

As for the optimisation process, a nature-inspired genetic algorithm (GA) was adopted. The

heuristic was employed to find an optimal or at least nearly optimal solution effectively from a large solution space (combination of the amount of added elements). The prediction process and optimisation were unified by a computer programming language, Python. In the overall designing approach, costs and processability of the alloy were considered and incorporated by setting several constraints as the alloy design was intended for a future commercial production. For cost constraints, the total elemental costs were calculated and those with high elemental costs were omitted from a group of candidate alloys. For guaranteeing the producibility, constraints regarding the volume fraction of liquid and other secondary phases estimated by equilibrium calculation were implemented in the calculation procedure. Before designing an alloy with the GA, processing parameters for the heuristic, such as the population size (a number of chromosomes in a generation) and mutation ratio (a probability of partial change when a chromosome is passed down to the next generation), were also optimised by simplified trial calculations.

The alloy was designed to have high yield stress after ageing at 750 °C for 400 hours, which simulated the service. The calculation combined the strength prediction with optimisation by the GA was carried out and the alloy chemistries were obtained. The chemical composition of the designed alloy (Fe-opt) is 0.01C-33Ni-15.5Cr-0.3Nb-1.6Al-2.8Ti-3.7W-0.9Co. After a simple experimental confirmation of the microstructure and hardness of the designed and conventional Ni-based and Fe-based alloys, the designed alloy was prepared as a sheet sample of 0.4 mm in thickness from 25 kg cast ingot and its microstructure and mechanical properties were experimentally validated and compared to a conventional high-temperature alloy. Fe-opt is confirmed to be strengthened by finely dispersed γ' and shows the high yield strength for its elemental costs after the ageing at 750 °C for 400 hours. However, the strength of Fe-opt is not as high as it was designed to be. On the grain boundary of Fe-opt, many coarse precipitates are observed and they are identified as Laves phases with a high amount of W and Nb. It is suggested that the coarse Laves phase, which is not incorporated into the design process, suppresses the formation of γ' as well as decreases the anti-phase boundary energy of the precipitate. The coarse Laves phase is also regarded as a cause of low ductility of Fe-opt.

Based on the experimental analysis for Fe-opt, the alloy whose chemistries was the same as Fe-opt except that W was excluded, was cast and made into a sheet specimen to be examined. The modified alloy without W (Fe-opt2) has many fine γ' in the matrix and the Laves phase is not observed after the ageing. The alloy shows the even higher yield strength than Fe-opt and 718Plus (the yield stress of Fe-opt, Fe-opt2 and 718Plus after the ageing at 750 °C for 400 hours are 794, 869 and 779 MPa, respectively). The elongation of Fe-opt2 after the long-time

ageing is also better than that of Fe-opt. These experimental results show that Fe-opt2 can be a strong potential candidate for the alloy used in the car sealing parts. It is also found that the agreement between the calculation and experimental investigation on the microstructural parameters and strength is reasonably well.

It is also suggested that alloy design can be achieved more effectively by combining the calculation and the experimental data obtained according to logical inference, than by conventional experiment-oriented alloy design approaches, although this study has clarified that the accuracy of the microstructure prediction should be further improved. This approach can be widely adopted for in many fields beyond high-temperature alloys by adopting suitable thermokinetic databases and strengthening modelling approaches.

7.2 Future work

Several experimental validations have been left for the future in addition to applying the alloy design approach demonstrated in this study to other materials. In order to obtain a deeper understanding of the microstructure and its influence on the strength, further microstructural analysis is required. For example, the chemical composition of γ' is of great interest as it affects the APB energy of the precipitate and the strength of the alloy. In this study, a calculated value was used as the chemical composition of the precipitate to estimate the APB energy. However, the experimental approaches, such as an atom probe tomography will provide more accurate comprehension of the relation between the APB energy and its strengthening effect. The influence of Laves phase on the strength of the alloy will be also clearer if the amount of Nb and Ti in γ' in Fe-opt and Fe-opt2 is measured and compared because the lack of Nb and Ti in γ' is supposed to lead to a decrease in precipitation strengthening from the change in APB energy.

Another important work to be conducted is to confirm the oxidation resistance at service temperature and creep properties of the designed alloy. As described in the thesis, the alloy is supposed to be used at high-temperature as high as 750 °C. Although the alloy contains 15.5 mass% Cr and 1.6 mass% Al, both of which improve high-temperature oxidation resistance, the experimental evaluation is required because the alloy is exposed to the high-temperature environment for a long period of time. Creep strength may be also important for guaranteeing the property of the product as the material is set between two flanges and stressed by them during the service when it is used as a sealing part in cars.

In this study, some constraints for production have been implemented in the alloy design process. For example, the alloy expected to contain liquid phase at 1200 °C was omitted from the candidate alloys to obtain a wide processing window for hot rolling. However, there are some other factors to be considered in terms of the processability, such as the formation resistance during hot rolling. Macro and micro elemental segregation in the ingot is also an important feature because it can be more difficult to control the segregation as the sample size is larger. After validating the oxidation resistance and the creep properties, large-scale production will be planned to prove that the designed alloy can be commercially manufactured.

References

[1] R.C. Reed. *The superalloys: fundamentals and applications*. Cambridge University Press, Cambridge, UK, 2006.

[2] C.T. Sims. A history of superalloy metallurgy for superalloy metallurgists. In *Superalloys 1984*, pages 399–419, 1984.

[3] B. Geddes, H. Leon, and X. Huang. *Superalloys: Alloying and Performance*. ASM International, 2010.

[4] G.F. Vander Voort, G.M. Lucas, and E.P. Manillova. Metallography and microstructures of heat-resistant alloys. In *ASM Handb.*, volume 9, pages 820–859. ASM International, 2004.

[5] G.F. Vander Voort, G.M. Lucas, and E.P. Manillova. Metallography and microstructures of stainless steels and maraging steels. In *ASM Handb.*, volume 9, pages 670–700. ASM International, 2004.

[6] K. Shaver and M. Mockenhaupt. Exhaust manifold gasket with spring steel embossed metal and graphite insulator (US 20110233875 A1), 2011.

[7] Aperam Alloys Imphy. Nickel iron and cobalt iron cold rolled strips. 2013.

[8] M.M. Morra, R.G. Ballinger, and I.S. Hwang. INCOLOY 908, a low coefficient of expansion alloy for high-strength cryogenic applications: Part I. Physical metallurgy. *Metall. Trans. A*, 23(12):3177–3192, Dec 1992.

[9] W.D. Cao and R.L. Kennedy. New developments in wrought 718-type superalloys. *Acta Metall. Sin.*, 18(1):39–46, Oct 2005.

[10] K. Kusabiraki, Z. Xiao-min, and T. Ooka. The growth of γ' precipitates in a 53Ni-20Co-15Cr superalloy. *ISIJ Int.*, 35(9):1115–1120, Sep 1995.

[11] C. Loier, C. Leymonie, and M.C. Ottmann. Structural transformation and mechanical properties of two non-magnetic alloys (Inconel 718 and ASTM A286). *Mater. Sci. Eng.*, 63:91–100, 1984.

[12] H. Long, S. Mao, Y. Liu, Z. Zhang, and X. Han. Microstructural and compositional design of Ni-based single crystalline superalloys — A review. *J. Alloys Compd.*, 743:203–220, 2018.

[13] S.S.M. Tavares, V. Moura, V.C. da Costa, M.L.R. Ferreira, and J.M. Pardal. Microstructural changes and corrosion resistance of AISI 310S steel exposed to 600 - 800 °C. *Mater. Charact.*, 60(6):573–578, Jun 2009.

[14] H. Sieurin, J. Zander, and R. Sandström. Modelling solid solution hardening in stainless steels. *Mater. Sci. Eng. A*, 415(1–2):66–71, Jan 2006.

[15] R.A. Ricks, A.J. Porter, and R.C. Ecob. The growth of γ' precipitates in nickel-base superalloys. *Acta Metall.*, 31(1):43–53, Jan 1983.

[16] P.H. Thornton and R.G. Davies. The temperature dependence of the flow stress of gamma prime phases having the $L1_2$ structure. *Metall. Mater. Trans. B*, 1(2):549–550, Feb 1970.

[17] P.H. Thornton, R.G. Davies, and T.L. Johnston. The temperature dependence of the flow stress of the γ' phase based upon Ni_3Al. *Metall. Trans.*, 1:207–218, 1970.

[18] S. Takeuchi and E. Kuramoto. Temperature and orientation dependence of the yield stress in Ni_3Ga single crystals. *Acta Metall.*, 21(4):415–425, Apr 1973.

[19] H. Sugimura, Y. Kaneno, and T. Takasugi. Alloying behavior of Ni_3Nb. *Mater. Trans.*, 51(1):72–77, 2010.

[20] K. Kusabiraki, L. Wang, T. Ooka, and K. Yamada. The growth of γ' and γ'' precipitates in Nickel-base superalloys. *Tetsu- to- Hagane*, 76(8):1341–1348, Aug 1990.

[21] A. Devaux, L. Nazé, R. Molins, A. Pineau, A. Organista, J. Y. Guédou, J. F. Uginet, and P. Héritier. Gamma double prime precipitation kinetic in Alloy 718. *Mater. Sci. Eng. A*, 486(1-2):117–122, Jul 2008.

[22] M.R. Ahmadi, B. Sonderegger, E. Povoden-Karadeniz, A. Falahati, and E. Kozeschnik. Precipitate strengthening of non-spherical precipitates extended in $\langle$ 100 $\rangle$ or { 100 } direction in fcc crystals. *Mater. Sci. Eng. A*, 590:262–266, Jan 2014.

[23] Y. Han, P. Deb, and M.C. Chaturvedi. Coarsening behaviour of γ''- and γ'-particles in Inconel alloy 718. *Met. Sci.*, 16(12):555–562, Dec 1982.

[24] J. Belan. GCP and TCP phases presented in nickel-base superalloys. *Mater. Today Proc.*, 3(4):936–941, 2016.

[25] M. Seifollahi, S.H. Razavi, Sh. Kheirandish, and S.M. Abbasi. The mechanism of η phase precipitation in A286 superalloy during heat treatment. *J. Mater. Eng. Perform.*, 22(10):3063–3069, Oct 2013.

[26] M. Dehmas, J. Lacaze, A. Niang, and B. Viguier. TEM Study of high-temperature precipitation of delta phase in Inconel 718 alloy. *Adv. Mater. Sci. Eng.*, 2011:1–9, 2011.

[27] S. Ghosh, S. Yadav, and G. Das. Study of standard heat treatment on mechanical properties of Inconel 718 using ball indentation technique. *Mater. Lett.*, 62(17–18):2619–2622, Jun 2008.

[28] W.D. Cao and R. Kennedy. Role of chemistry in 718-type alloys - Allvac® 718Plus™ alloy development. *Superalloys*, 3:91–99, 2004.

[29] F. Long, Y.S. Yoo, C.Y. Y. Jo, S.M. Seo, Y.S. Song, T. Jin, and Z.Q. Hu. Formation of η and σ phase in three polycrystalline superalloys and their impact on tensile properties. *Mater. Sci. Eng. A*, 527(1-2):361–369, Dec 2009.

[30] M. Segawa, A. Taniyama, and D. Shindo. HREM observation of the interface between Laves-phases and matrix phases in Inconel 718 by using a high-voltage electron microscope. *ISIJ Int.*, 38:1375 – 1378, 1998.

[31] M.G. Burke and M.K. Miller. Grain boundary intermetallic phases in alloy 718. In G.M. Stocks, S.P. Pope, and A.F. Giamei, editors, *Proc. Alloy Phase Stab. Des.*, volume 186, pages 215–218, San Francisco, CA, 1990.

[32] S.S.K. Balam, H.Q. Dong, T. Laurila, V. Vuorinen, and A. Paul. Diffusion and growth of the μ phase (Ni_6Nb_7) in the Ni-Nb system. *Metall. Mater. Trans. A*, 42(7):1727–1731, Jul 2011.

[33] F. Sun, J. Zhang, P. Liu, Q. Feng, X. Han, and S. Mao. High resolution transmission electron microscopy studies of σ phase in Ni-based single crystal superalloys. *J. Alloys Compd.*, 536:80–84, Sep 2012.

[34] W. Chen, M.C. Chaturvedi, N.L. Richards, and G. McMahon. Grain boundary segregation of boron in Inconel 718. *Metall. Mater. Trans. A*, 29(7):1947–1954, Jul 1998.

[35] Y. Huang and P. L. Blackwell. Microstructure development and superplasticity in Inconel 718 sheet. *Mater. Sci. Technol.*, 19(4):461–466, Apr 2003.

[36] X.K. Meng, H. Shen, and H. Vehoff. Fractography, elastic modulus, and oxidation resistance of novel metal–intermetallic Ni/Ni_3Al multilayer films. *J. Mater. Res.*, 17(4):790–796, 2002.

[37] P.V.M. Rao, K.S. Murthy, and S.V. Suryanarayana. Effect of third elements on the microhardness of Ni_3Al. *Mater. Lett.*, 14(5–6):281–284, Sep 1992.

[38] C. Slama and M. Abdellaoui. Structural characterization of the aged Inconel 718. *J. Alloys Compd.*, 306(1–2):277–284, Jun 2000.

[39] D. Connétable, M. Mathon, and J. Lacaze. First principle energies of binary and ternary phases of the Fe–Nb–Ni–Cr system. *Calphad*, 35(4):588–593, Dec 2011.

[40] I.I. Kornilov and E.N. Pylaeva. An investigation of the equilibrium of the ternary system of metallides Ni_3Nb-Ni_3Ti-Ni_3Ta. *Bull. Acad. Sci. USSR, Div. Chem. Sci.*, 10(2):178–181, Feb 1961.

[41] G.R. Evers, H.H. Smith, and D.J. Michel. An investigation of second phases in alloy 718 using electrolytic extraction techniques. *Metallography*, 11(4):441–457, Oct 1978.

[42] K. Zhao, Y.H. Ma, L.H. Lou, and Z.Q. Hu. μ phase in a nickel base directionally solidified alloy. *Mater. Trans.*, 46(01):54–58, 2005.

[43] H. Brandis, E. Haberling, and H.H. Weigand. Metallurgical aspects of carbides in high speed steels. In *Process. Prop. High-Speed Tool Steels*, pages 1–18, Las Vegas, Nevada, 1980.

[44] X. Dong, X. Zhang, K. Du, Y. Zhou, T. Jin, and H. Ye. Microstructure of carbides at grain boundaries in nickel based superalloys. *J. Mater. Sci. Technol.*, 28(11):1031–1038, 2012.

[45] S.T. Oyama. *The chemistry of transition metal carbides and nitrides*. Blackie Academic & Professional, Glasgow, 1st edition, 1996.

[46] X. Z. Qin, J. T. Guo, C. Yuan, J. S. Hou, and H. Q. Ye. Precipitation and thermal instability of $M_{23}C_6$ carbide in cast Ni-base superalloy K452. *Mater. Lett.*, 62(2):258–261, Jan 2008.

[47] C. Kral, W. Lengauer, D. Rafaja, and P. Ettmayer. Critical review on the elastic properties of transition metal carbides, nitrides and carbonitrides. *J. Alloys Compd.*, 265(1–2):215–233, Jan 1998.

[48] L. Karlsson and H. Horden. Grain boundary segregation of boron. An exprerimental and theoretical study. *J. Phys. Colloq.*, 47(C7):257–262, 1986.

[49] X. Xie, C. Xu, G. Wang, Ji. Dong, W.D. Cao, and R. Kennedy. TTT Diagram of a newly developed nickel-base superalloy - Allvac® 718Plus™. In E.A. Loria, editor, *Superalloys 718, 625, 706 Deriv.*, pages 193–202. TMS (The Minerals, Metals & Materials Society), 2005.

[50] D.A. Porter, K.E. Easterling, and M.Y. Sherif. *Phase transformations in metals and alloys*. CRC Press, Boca Raton, FL, 3rd edition, 2009.

[51] K.C. Russell. Nucleation in solids: The induction and steady state effects. *Adv. Colloid Interface Sci.*, 13(3–4):205–318, Sep 1980.

[52] D. Turnbull and J.C. Fisher. Rate of nucleation in condensed systems. *J. Chem. Phys.*, 17:71, 1949.

[53] E. Kozeschnik. *Modeling solid-state precipitation*. Momentum Press, 1st edition, Dec 2012.

[54] X.P. Tan, D. Mangelinck, C. Perrin-Pellegrino, L. Rougier, CH.-A. Gandin, A. Jacot, D. Ponsen, and V. Jaquet. Spinodal decomposition mechanism of γ' precipitation in a single crystal Ni-based superalloy. *Metall. Mater. Trans. A*, 45:4725–4730, 2014.

[55] H. Wendt and P. Haasen. Nucleation and growth of γ-Precipitates in Ni-14 at.% Al. *Acta Metall.*, 31(10):1649–1659, 1983.

[56] C. Zener. Theory of growth of spherical precipitates from solid solution. *J. Appl. Phys.*, 20(10):950–953, Oct 1949.

[57] L. Onsager. Reciprocal relations in irreversible processes. I. *Phys. Rev.*, 37(4):405–426, Feb 1931.

[58] J. Svoboda, F.D. Fischer, P. Fratzl, and E. Kozeschnik. Modelling of kinetics in multi-component multi-phase systems with spherical precipitates: I: Theory. *Mater. Sci. Eng. A*, 385(1-2):166–174, 2004.

[59] E. Kozeschnik, J. Svoboda, P. Fratzl, and F.D. Fischer. Modelling of kinetics in multi-component multi-phase systems with spherical precipitates: II: Numerical solution and application. *Mater. Sci. Eng. A*, 385(1–2):166–174, Nov 2004.

[60] L. Ratke and P.W. Voorhees. *Growth and coarsening: ostwald ripening in material processing*. Springer Science and Business Media, 2002.

[61] I.M. Lifshitz and V.V. Slyozov. The kinetics of precipitation from supersaturated solid solutions. *J. Phys. Chem. Solids*, 19(1–2):35–50, Apr 1961.

[62] M. Kahlweit. Ostwald ripening of precipitates. *Adv. Colloid Interface Sci.*, 5(1):1–35, Aug 1975.

[63] R. Kampmann and R. Wagner. Kinetics of precipitation in metastable binary alloys - theory and application to Cu-1.9 at % Ti and Ni-14 at % Al. In P. Haasen, V. Gerold, R. Wagner, and M.F. Ashby, editors, *Decompos. Alloy. Early Stages*, pages 91–103. Pergamon, 1984.

[64] W.A. Johnson and R.F. Mehl. Reaction kinetics in process of nucleation and growth. *Trans. Am. Inst. Min. Metall. Eng.*, 135:416–442, 1939.

[65] M. Avrami. Kinetics of phase change. I general theory. *J. Chem. Phys.*, 7(12):1103–1112, Dec 1939.

[66] J.S. Langer and A.J. Schwartz. Kinetics of nucleation in near-critical fluids. *Phys. Rev. A*, 21(3):948–958, Mar 1980.

[67] R.K. Ham and L.M. Brown. *Strengthening Methods in Crystals*. Appl. Sci. Ltd., London, 1971.

[68] B. Reppich. Some new aspects concerning particle hardening mechanisms in γ' precipitating Ni-base alloys—I. Theoretical concept. *Acta Metall.*, 30(1):87–94, Jan 1982.

[69] M.R. Ahmadi, E. Povoden-Karadeniz, K.I. Öksüz, A. Falahati, and E. Kozeschnik. A model for precipitation strengthening in multi-particle systems. *Comput. Mater. Sci.*, 91:173–186, Aug 2014.

[70] E. Nembach and G. Neite. Precipitation hardening of superalloys by ordered γ'-particles. *Prog. Mater. Sci.*, 29(3):177–319, Jan 1985.

[71] E.I. Galindo-Nava, L.D. Connor, and C.M.F. Rae. On the prediction of the yield stress of unimodal and multimodal γ' Nickel-base superalloys. *Acta Mater.*, 98:377–390, Oct 2015.

[72] D.J. Crudden, A. Mottura, N. Warnken, B. Raeisinia, and R.C. Reed. Modelling of the influence of alloy composition on flow stress in high-strength nickel-based superalloys. *Acta Mater.*, 75:356–370, Aug 2014.

[73] J. M. Oblak, D. F. Paulonis, and D. S. Duvall. Coherency strengthening in Ni base alloys hardened by $D0_{22}$ γ'' precipitates. *Metall. Trans.*, 5(1):143–153, Jan 1974.

[74] A.J. Ardell. Precipitation hardening. *Metall. Trans. A*, 16A:2131–2165, 1985.

[75] T. J. Koppenaal. The effect of prestressing on the strength of neutron-irradiated copper single crystals. *Appl. Phys. Lett.*, 4:59, 1964.

[76] A.J.E. Foreman and M.J. Makin. Dislocation movement through random arrays of obstacles. *Can. J. Phys.*, 45(2):511–517, 1967.

[77] R.L. Fleischer. Substitutional solution hardening. *Acta Metall.*, 11(3):203–209, Mar 1963.

[78] R. Labusch. A Statistical theory of solid solution hardening. *Phys. status solidi*, 41(2):659–669, 1970.

[79] L.A. Gypen and A. Deruyttere. Multi-component solid solution hardening Part1. *J. Mater. Sci.*, 12(5):1028–1033, May 1977.

[80] L.A. Gypen and A. Deruyttere. Multi-component solid solution hardening Part2. *J. Mater. Sci.*, 12(5):1034–1038, May 1977.

[81] H.A. Roth, C.L. Davis, and R.C. Thomson. Modeling solid solution strengthening in nickel alloys. *Metall. Mater. Trans. A*, 28(6):1329–1335, Jun 1997.

[82] E.O. Hall. The deformation and ageing of mild steel: III discussion of results. *Proc. Phys. Soc. Sect. B*, 64(9):747, Sep 1951.

[83] N.J. Petch. The cleavage strength of polycrystals. *J. Iron Steel Inst.*, 174:25–28, 1953.

[84] J.D. Eshelby, F.C. Frank, and F.R.N. Nabarro. XLI. The equilibrium of linear arrays of dislocations. *London, Edinburgh, Dublin Philos. Mag. J. Sci.*, 42(327):351–364, 1951.

[85] J.C.M. Li and Y.T. Chou. The role of dislocations in the flow stress grain size relationships. *Metall. Mater. Trans.*, 1(5):1145–1159, May 1970.

[86] T. Tsuchiyama, Y. Fujii, Y. Terazawa, K. Nakashima, T. Ando, and S. Takaki. Factors inducing intergranular fracture in nickel-free high nitrogen austenitic stainless steel produced by solution nitriding. *ISIJ Int.*, 48(6):861–867, 2008.

[87] S. Floreen and J.H. Westbrook. Grain boundary segregation and the grain size dependence of strength of nickel-sulfur alloys. *Acta Metall.*, 17(9):1175–1181, Sep 1969.

[88] J.S.C. Jang and C.C. Koch. The hall-petch relationship in nanocrystalline iron produced by ball milling. *Scr. Metall. Mater.*, 24(8):1599–1604, Aug 1990.

[89] K. Kato, E. Kawakami, J. Ohta, and M. Mayuzumi. Effects of various alloying elements on tensile properties of high-purity Fe-18Cr-(14-16)Ni alloys at room temperature. *Mater. Trans.*, 43(2):155–162, 2002.

[90] R.W. Kozar, A. Suzuki, W.W. Milligan, J. J. Schirra, M.F. Savage, and T.M. Pollock. Strengthening mechanisms in polycrystalline multimodal Nickel-base superalloys. *Metall. Mater. Trans. A*, 40(7):1588–1603, Jul 2009.

[91] T. Parthasarathy, S. Rao, and D. Dimiduk. A fast spreadsheet model for the yield strength of superalloys. *Superalloys 2004*, pages 887–896, 2004.

[92] S. Takaki, K. Kawasaki, and Y. Kimura. Mechanical properties of ultra fine grained steels. *J. Mater. Process. Technol.*, 117(3):359–363, Nov 2001.

[93] A.A.W. Thompson. Yielding in nickel as a function of grain or cell size. *Acta Metall.*, 23(11):1337–1342, Nov 1975.

[94] F. Wallow and E. Nembach. Synergisms of grain boundary and γ' -particle strengthening in nickel-base superalloys. *Scr. Mater.*, 34(3):499–505, Feb 1996.

[95] J.E. Bailey and P.B. Hirsch. The dislocation distribution, flow stress, and stored energy in cold-worked polycrystalline silver. *Philos. Mag.*, 5(53):485–497, May 1960.

[96] B.D. Conduit, N.G. Jones, H.J. Stone, and G.J. Conduit. Design of a nickel-base superalloy using a neural network. *Mater. Des.*, 131:358–365, 2017.

[97] S. Dey, N. Sultana, M.S. Kaiser, P. Dey, and S. Datta. Computational intelligence based design of age-hardenable aluminium alloys for different temperature regimes. *Mater. Des.*, 92:522–534, Feb 2016.

[98] S. Dey, P. Dey, and S. Datta. Design of novel age-hardenable aluminium alloy using evolutionary computation. *J. Alloys Compd.*, 704:373–381, May 2017.

[99] S. Ganguly, S. Datta, and N. Chakraborti. Genetic algorithms in optimization of strength and ductility of low-carbon steels. *Mater. Manuf. Process.*, 22(5):650–658, Jun 2007.

[100] A.J. Kulkarni, K. Krishnamurthy, S.P. Deshmukh, and R.S. Mishra. Microstructural optimization of alloys using a genetic algorithm. *Mater. Sci. Eng. A*, 372(1-2):213–220, May 2004.

[101] M. Mahfouf, M. Jamei, and D. a. Linkens. Optimal design of alloy steels using multiobjective genetic algorithms. *Mater. Manuf. Process.*, 20(3):553–567, 2005.

[102] I. Mohanty, D. Bhattacharjee, and S. Datta. Designing cold rolled IF steel sheets with optimized tensile properties using ANN and GA. *Comput. Mater. Sci.*, 50(8):2331–2337, Jun 2011.

[103] W. Sitek and L.A. Dobrzański. Application of genetic methods in materials' design. *J. Mater. Process. Technol.*, 164-165:1607–1611, May 2005.

[104] W. Xu, P.E.J. Rivera-Díaz-del Castillo, and S. van der Zwaag. Genetic alloy design based on thermodynamics and kinetics. *Philos. Mag.*, 88(12):1825–1833, Apr 2008.

[105] W. Xu, P.E.J. Rivera-Díaz-del Castillo, W. Yan, K. Yang, D. San Martín, L.A.I. Kestens, and S. van der Zwaag. A new ultrahigh-strength stainless steel strengthened by various coexisting nanoprecipitates. *Acta Mater.*, 58(11):4067–4075, Jun 2010.

[106] W. Xu, P.E.J. Rivera-Díaz-del Castillo, and S. van der Zwaag. Computational design of UHS maraging stainless steels incorporating composition as well as austenitisation and ageing temperatures as optimisation parameters. *Philos. Mag.*, 89(20):1647–1661, Jul 2009.

[107] H.K.D.H. Bhadeshia. Neural networks in Materials Science. *ISIJ Int.*, 39(10):966–979, 1999.

[108] P. Das, S. Mukherjee, S. Ganguly, B.K. Bhattacharyay, and S. Datta. Genetic algorithm based optimization for multi-physical properties of HSLA steel through hybridization of neural network and desirability function. *Comput. Mater. Sci.*, 45(1):104–110, Mar 2009.

[109] E. Menou, G. Ramstein, E. Bertrand, and F. Tancret. Multi-objective constrained design of nickel-base superalloys using data mining- and thermodynamics-driven genetic algorithms. *Model. Simul. Mater. Sci. Eng.*, 24(5):055001, 2016.

[110] D.E. Goldberg and J.H. Holland. Genetic algorithms and machine learning. *Mach. Learn.*, 3(2-3):95–99, 1988.

[111] D.E. Goldberg. *Genetic algorithms in search, optimization, and machine learning*. Addison-Wesley Longman Publishing Co., Boston, 1989.

[112] D. Whitley, T. Starkweather, and C. Bogart. Genetic algorithms and neural networks: optimizing connections and connectivity. *Parallel Comput.*, 14(3):347–361, Aug 1990.

[113] S.M. Kimball. Mineral Commodity Summaries 2015. Technical report, U.S. Department of the Interior, 2015.

[114] D.E. Camus, R.A. Jaramillo, J.A. Plybum, and F.S. Suarez. Evolution of microstructure during hot rolling of Inconel@ Alloys 625 and 7 18. In E.A. Loria, editor, *Superalloys 718, 625, 706 Deriv.*, pages 291–302. TMS (The Minerals, Metals & Materials Society), 1997.

[115] B. Sonderegger and E. Kozeschnik. Generalized nearest-neighbor broken-bond analysis of randomly oriented coherent interfaces in multicomponent fcc and bcc structures. *Metall. Mater. Trans. A*, 40(3):499–510, Mar 2009.

[116] K. Kusabiraki, S. Araie, and T. Ooka. Precipitation and growth of γ''-phase in Ni-15Cr-8Fe-6Nb alloy. *Tetsu-to-Hagane*, 78(4):650–657, 1992.

[117] K. Kusabiraki and T. Maekawa. Precipitation and growth of γ'' phase in a Ni-22Cr-9Mo-5Fe-4Nb superalloy. *Tetsu-to-Hagane*, 85(3):241–248, 1999.

[118] M. Sundararaman and P. Mukhopadhyay. Overlapping of γ'' precipitate variants in Inconel 718. *Mater. Charact.*, 31(4):191–196, 1993.

[119] M. Mantina, R. Valero, C.J. Cramer, and D.G. Truhlar. Atomic radii of the elements. In W.M. Haynes, editor, *Handb. Chem. Phys. Sect.*, pages 49–50. Taylor & Francis Group, 94th edition, 2013.

[120] I. Toda-Caraballo and P.E.J. Rivera-Díaz-del Castillo. Modelling solid solution hardening in high entropy alloys. *Acta Mater.*, 85:14–23, Feb 2015.

[121] Y. Mishima, S. Ochiai, N. Hamao, M. Yodogawa, and T. Suzuki. Solid solution hardening of nickel -role of transition metal and B-subgroup solutes. *Trans. Japan Inst. Met.*, 27(9):656–664, 1986.

[122] M.R. Ahmadi, E. Povoden-Karadeniz, L. Whitmore, M. Stockinger, A. Falahati, and E. Kozeschnik. Yield strength prediction in Ni-base alloy 718Plus based on thermo-kinetic precipitation simulation. *Mater. Sci. Eng. A*, 608:114–122, Jul 2014.

[123] S. Mannan, E. Hibner, and B. Puckett. Physical metallurgy of alloys 718, 725, 725HS, 925 for service in aggresive corrosive environments. In *Corros. 2003*, pages NACE–03126. NACE International, 2003.

[124] S. Mannan, S. Patel, and J. DeBarbadillo. Long term thermal stability of Inconel alloys 718, 706, 909, and Waspaloy at 593 °C and 704 °C. In T.M. Pollock, R.D. Kissinger, R.R Bowman, K.A. Green, M. McLean, S. Olson, and J.J. Schirra, editors, *Superalloys 2000*, pages 449–458. TMS, 2000.

[125] Z. Miskovic, M. Jovanovic, M. Gligic, and B. Lukic. Microstructural investigation of IN 939. *Vacuum*, 43(5-7):709–711, 1992.

[126] Y. Nakao and K. Mitsuhata. Behavior of precipitates in Ni-base superalloy, Waspaloy. *Q. J. Japan Weld. Soc.*, 3(4):815–822, 1985.

[127] X. Xie, G. Wang, J. Dong, C. Xu, W.D. Cao, and R. Kennedy. Structure stability study on a newly developed nickel-base superalloy—Allvac® 718Plus™. In E.A. Loria, editor, *Superalloys 718, 625, 706 Deriv. 2005*, pages 179–191. TMS (The Minerals, Metals & Materials Society), 2005.

[128] K. Hayashi and K. Kakehi. Effect of heat treatment on mechanical properties of Inconel 718. *J. Japan Inst. Met.*, 74(08):501–507, 2010.

[129] T. Katsurai, T. Nishiyama, and S. Hamano. Development of high-heat-resistant high-nitrogen containing austenitic stainless steel for exhaust gasket. *Honda R&D Tech. Rev.*, 15(2):167–174, 2003.

[130] N. Saunders, Z. Guo, A.P. Miodownik, and J-Ph. Schille. Modelling the material properties and behaviour of Ni-based superalloys. In K.A. Green, T.M. Pollock, H. Harada, T.E. Howson, R.C. Reed, J.J. Schirra, and S. Walston, editors, *Superalloy 2004*, pages 849–858. TMS (The Minerals, Metals & Materials Society), 2004.

[131] A.W. Thompson and J.A. Brooks. The mechanism of precipitation strengthening in an iron-base superalloy. *Acta Metall.*, 30:2197–2203, 1982.

[132] M. Savoie, C. Esnouf, L. Fournier, and D. Delafosse. Influence of ageing heat treatment on alloy A-286 microstructure and stress corrosion cracking behaviour in PWR primary water. *J. Nucl. Mater.*, 360(3):222–230, Mar 2007.

[133] R.L. Kennedy. Allvac® 718Plus™, superalloy for the next forty years. In E.A. Loria, editor, *Superalloys 718, 625, 706 Deriv.*, pages 1–14. TMS (The Minerals, Metals & Materials Society), 2005.

[134] R. Darolia, D.F. Lahrman, R.D. Field, and R. Sisson. Formation of topologically closed packed phases in nickle base single crystal superalloys. In S. Reichman, D.N. Duhl, G Maurer, S. Antolovich, and C. Lund, editors, *Superalloys 1988*, pages 255–264. The Metallurgical Society, 1988.

[135] C.M.F. Rae and R.C. Reed. The precipitation of topologically close-packed phases in rhenium-containing superalloys. *Acta Mater.*, 49(19):4113–4125, Nov 2001.

[136] J.N. DuPont, J.C. Lippold, and S.D. Kiser. *Welding Metallurgy and Weldability of Nickel-Base Alloys*. John Wiley & Sons, New Jersey, 2011.

[137] G.A. Zickler, R. Radis, R. Schnitzer, E. Kozeschnik, M. Stockinger, and H. Leitner. The precipitation behavior of superalloy ATI Allvac 718Plus. *Adv. Eng. Mater.*, 12(3):176–183, Apr 2010.

[138] E.J. Pickering, H. Mathur, A. Bhowmik, O.M.D.M. Messé, J.S. Barnard, M.C. Hardy, R. Krakow, K. Loehnert, H.J. Stone, and C.M.F. Rae. Grain-boundary precipitation in Allvac 718Plus. *Acta Mater.*, 60(6–7):2757–2769, Apr 2012.

[139] O.M. Messé, J.S. Barnard, E.J. Pickering, P.A. Midgley, and C.M.F. Rae. On the precipitation of delta phase in ALLVAC® 718Plus. *Philos. Mag.*, 94(10):1132–1152, Mar 2014.

[140] P. Ghosh, B. Bhattacharya, and R.K. Ray. Comparative study of precipitation behavior and texture formation in cold rolled-batch annealed and cold rolled-continuous annealed interstitial free high strength steels. *Scr. Mater.*, 56(8):657–660, Apr 2007.

Appendix A

Code for alloy design

```
# ************************************************************
# ABOUT THIS SCRIPT
# ************************************************************
# Script author: Masayoshi Sawada
# This is a script to optimise chemical composition of Fe-Ni-based alloy with
    a GA method.

# ************************************************************
# How to execute the program
# ************************************************************
# >python
# >import ga_fe
# >ga_fe.genetic(ga_fe.strengthcalc)

# ************************************************************
# Preparation
# ************************************************************
import xlrd, csv, sys, random, math
#, matcalc_calc
from subprocess import Popen, PIPE
from os import getcwd, chdir, devnull
from platform import system
from xlrd import open_workbook, cellname

# ************************************************************
# strength calculation
# ************************************************************

def strengthcalc(s):
      # ************************************************************
      # Decode input parameter (chemical compositions)
      # ************************************************************
      # fe, cr. nb, mo, ti, al, co, w, c
      pmax=[60, 25, 5, 5, 5, 5, 10, 5, 0.01]
      pmin=[40, 10.0, 0.0001, 0.0001, 0.0001, 0.0001, 0.0001, 0.0001, 0.0001]
      decoded=[]
      for i in range(len(s)):
            paramax=pmax[i]
            paramin=pmin[i]
            j=(paramax-paramin)/30.0*s[i]+paramin
            decoded.append(j)

```

```
42        # ************************************************************
43        # Setup directory
44        # ************************************************************
45        # Set directories and files
              POINTERS_____________________________________________
46        working_dir = str(getcwd())+"/"
47        MatCalc_dir = '/Users/***/' # set directory where MatCalc locates
48        script_pointer1 = working_dir + 'script_file_initial_1200.mcs'
49        script_pointer2 = working_dir + 'script_file_initial_1000.mcs'
50        script_pointer3 = working_dir + 'script_file_initial_750.mcs'
51        parameter_list = []
52        stringslist = decoded
53        cost = (stringslist[0]*0.4+stringslist[1]*2.4+stringslist[2]*64.2+
              stringslist[3]*29.4+stringslist[4]*10.9+stringslist[5]*2.3+
              stringslist[6]*35.3+stringslist[7]*37.8+(100-sum(stringslist))*18.8)
              *0.01
54        print "************************************************************"
55        print "Fe,␣Cr,␣Nb,␣Mo,␣Ti,␣Al,␣Co,␣W,␣C␣(coded):␣" + "%4d␣" * 9 % tuple
              (s)
56        print "Fe,␣Cr,␣Nb,␣Mo,␣Ti,␣Al,␣Co,␣W,␣C␣in␣(wp):␣" + "%4.2f␣" * 9 %
              tuple(stringslist)
57        print "Elemental␣cost:␣%(cost)4.2f,␣Ni␣concentration:␣%(Ni)4.2f␣/wp" %
               {"cost":cost, "Ni":100-sum(stringslist)}
58        inp = open('calc_result_fe.txt', 'a')
59        inp.write("************************************************************" +
               '\n')
60        inp.write("Fe,␣Cr,␣Nb,␣Mo,␣Ti,␣Al,␣Co,␣W,␣C␣(coded):␣" + "%4d␣" * 9 %
              tuple(s) + '\n')
61        inp.write("Fe,␣Cr,␣Nb,␣Mo,␣Ti,␣Al,␣Co,␣W,␣C␣in␣(wp):␣" + "%4.2f␣" * 9 %
               tuple(stringslist) + '\n')
62        inp.write("Elemental␣cost:␣%(cost)4.2f,␣Ni␣concentration:␣%(Ni)4.2f␣/
              wp␣\n" % {"cost":cost, "Ni":100-sum(stringslist)})
63        inp.close()
64
65        # If the cost is above a criterion or wt%(Ni) is less than 20%,
              strength is 0
66        if float(cost) > 10.0:
67              strength = 0
68              print "Cost␣is␣too␣high"
69              f = open('calc_result_fe.txt', 'a')
70              f.write("Cost␣is␣too␣high" + '\n')
71              f.close()
72        elif sum(stringslist) > 80:
73              strength = 0
74              print "Ni␣content␣is␣too␣low␣(less␣than␣20␣wt%)"
75              f = open('calc_result_fe.txt', 'a')
76              f.write("Ni␣content␣is␣too␣low␣(less␣than␣20␣wt%)" + '\n')
77              f.close()
78        else:
79
80        # ************************************************************
81        # MatCalc script
82        # ************************************************************
83              with open(script_pointer1, 'w') as scr:
84                    scr.write("""use-module core
85        new-workspace
86        open-thermodyn-database mc_ni2.011.tdb
87
88        $ select elements and phases
89        select-elements al co cr nb ni c fe mo ti w
```

```
90          select-phases fcc_a1 gamma_prime gamma_dp eta delta mu_phase sigma liq
                M23C6
91          set-reference-element ni
92          read-thermodyn-database
93          $ chemical composition
94          enter-composition wp fe={0} cr={1} nb={2} mo={3} ti={4} al={5} co={6}
                w={7} c={8}
95
96          set-automatic-startvalues
97          set-temperature-celsius 1200      $ Temperature
98          calculate-equilibrium        $ Initial equilibrium
99          set-variable-value liq_frac1 f$liquid
100
101         $ ************************************************************
102         $ Output the result for Calc (1200 oC)
103         $ ************************************************************
104         set-working-directory /Users/***/
105         export-open-file initial_result_1200.csv
106         export-clear-file
107         export-file-variables "%5.3f" liq_frac1
108         export-close-file
109         """.format(*stringslist))
110
111         # ************************************************************
112         # MatCalc script
113         # ************************************************************
114               with open(script_pointer2, 'w') as scr:
115                     scr.write("""use-module core
116
117         new-workspace
118         open-thermodyn-database mc_ni2.011.tdb
119
120         $ select elements and phases
121         select-elements al co cr nb ni c fe mo ti w
122         select-phases fcc_a1 gamma_prime gamma_dp eta delta mu_phase sigma liq
                M23C6
123
124         set-reference-element ni
125         read-thermodyn-database
126
127         $ chemical composition
128         enter-composition wp fe={0} cr={1} nb={2} mo={3} ti={4} al={5} co={6}
                w={7} c={8}
129
130         set-automatic-startvalues
131         set-temperature-celsius 1000      $ Temperature
132         calculate-equilibrium        $ Initial equilibrium
133         set-variable-value mu_frac2 f$mu_phase
134         set-variable-value sigma_frac2 f$sigma
135         set-variable-value gp_frac2 f$gamma_prime
136         set-variable-value dp_frac2 f$gamma_dp
137         set-variable-value eta_frac2 f$eta
138         set-variable-value delta_frac2 f$delta
139         set-variable-value m23c6_frac2 f$m23c6
140
141         $ ************************************************************
142         $ Output the result for Calc (1000 oC)
143         $ ************************************************************
144         set-working-directory /Users/***/ $put a set-working-directory on ***
145         export-open-file initial_result_1000.csv
```

```
146         export-clear-file
147         export-file-variables "%5.3f, %5.3f, %5.3f, %5.3f, %5.3f, %5.3f, %5.3f
                " mu_frac2 sigma_frac2 gp_frac2 dp_frac2 eta_frac2 delta_frac2
                m23c6_frac2
148         export-close-file
149         """.format(*stringslist))
150 
151                 # ********************************************************
152                 # Execute the script in MatCalc
153                 # ********************************************************
154                 # Save the original directory location
155                 orig_dir = getcwd()
156                 chdir(MatCalc_dir)
157 
158                 # Open MatCalc app and execute the script above
159                 devnull_object = open(devnull, "w")
160                 run_files = Popen("./mcc␣"+script_pointer1, stdin=PIPE, stdout=
                        devnull_object, shell=True)
161                 run_files.communicate(input='exit')
162                 run_files2 = Popen("./mcc␣"+script_pointer2, stdin=PIPE, stdout=
                        devnull_object, shell=True)
163                 run_files2.communicate(input='exit')
164                 run_files3 = Popen("./mcc␣"+script_pointer3, stdin=PIPE, stdout=
                        devnull_object, shell=True)
165                 run_files3.communicate(input='exit')
166 
167                 # ********************************************************
168                 # Constraints calclulation
169                 # ********************************************************
170                 chdir(orig_dir) # Go back to the original directory
171 
172                 g = open('initial_result_1200.csv', 'rb')
173                 list1 = []
174                 reader = csv.reader(g)
175                 for row in reader:
176                         list1.append(row)
177                 list1 = list1[0]
178                 print "Liquid␣at␣1200␣oC:␣" + str(list1[0])
179                 liq_frac_1200 = float(list1[0])
180                 g.close()
181 
182                 g = open('initial_result_1000.csv', 'rb')
183                 list2 = []
184                 reader = csv.reader(g)
185                 for row in reader:
186                         list2.append(row)
187                 list2 = list2[0]
188                 print "mu␣and␣sigma␣at␣1000␣oC:␣" + str(list2[0]) + ",␣" + str(
                        list2[1])
189                 print "gamma␣prime␣and␣gamma␣double␣prime␣at␣1000␣oC:␣" + str(
                        list2[2]) + ",␣" + str(list2[3])
190                 print "eta␣and␣delta␣at␣1000␣oC:␣" + str(list2[4]) + ",␣" + str(
                        list2[5])
191                 print "M23C6␣at␣1000␣oC:␣" + str(list2[6])
192 
193                 mu_frac_1000 = float(list2[0])
194                 sigma_frac_1000 = float(list2[1])
195                 gp_frac_1000 = float(list2[2])
196                 dp_frac_1000 = float(list2[3])
197                 eta_frac_1000 = float(list2[4])
198                 delta_frac_1000 = float(list2[5])
```

```
199             m23c6_frac_1000 = float(list2[6])
200             g.close()
201
202             if liq_frac_1200 > 0:
203                    strength = 0
204                    print "liquid␣exists␣at␣1200␣oC"
205                    f = open('calc_result_fe.txt', 'a')
206                    f.write("liquid␣at␣1200␣oC" + '\n')
207                    f.close()
208                    return strength
209             elif mu_frac_1000 > 0.01:
210                    strength = 1
211                    print "Too␣much␣Mu␣phase␣at␣1000␣oC"
212                    f = open('calc_result_fe.txt', 'a')
213                    f.write("Too␣much␣Mu␣phase␣at␣1000␣oC" + '\n')
214                    f.close()
215                    return strength
216             elif sigma_frac_1000 > 0.01:
217                    strength = 1
218                    print "Too␣much␣Sigma␣phase␣at␣1000␣oC"
219                    f = open('calc_result_fe.txt', 'a')
220                    f.write("Too␣much␣Sigma␣phase␣at␣1000␣oC" + '\n')
221                    f.close()
222                    return strength
223             elif eta_frac_1000 > 0.01:
224                    strength = 1
225                    print "Too␣much␣Eta␣phase␣at␣1000␣oC"
226                    f = open('calc_result_fe.txt', 'a')
227                    f.write("Too␣much␣eta␣phase␣at␣1000␣oC" + '\n')
228                    f.close()
229                    return strength
230             elif delta_frac_1000 > 0.01:
231                    strength = 1
232                    print "Too␣much␣Delta␣phase␣at␣1000␣oC"
233                    f = open('calc_result_fe.txt', 'a')
234                    f.write("Too␣much␣delta␣phase␣at␣1000␣oC" + '\n')
235                    f.close()
236                    return strength
237             else:
238                    script_pointer = working_dir + 'script_file_ga.mcs'
239
240
241                    # ************************************************
242                    # MatCalc script for kinetic calculation
243                    # ************************************************
244                    with open(script_pointer, 'w') as scr:
245                           scr.write("""use-module core
246             close-workspace f
247             new-workspace
248
249             open-thermo-database mc_ni2.011.tdb  $ thermodynamic database
250             select-elements al co cr nb ni c fe mo ti w   $ select elements
251             select-phases fcc_a1 gamma_prime gamma_dp eta delta m23c6 $
                    select phases
252             set-reference-element ni
253
254             read-thermodyn-database
255
256             enter-composition wp fe={0} cr={1} nb={2} mo={3} ti={4} al={5}
                    co={6} w={7} c={8} $ chemical compositions
257             read-mobility-database mc_fe_2.010.ddb   $ read diffusion data
```

```
258
259         set-variable-value npc 10 $ number of precipitate classes
260
261         $ precipitate domains (ironmatrix)
262         create-precipitation-domain ironmatrix    $ ironmatrix as prec.
                domain = matrix
263         set-precipitation-parameter ironmatrix x fcc_a1  $ matrix phase
                of domain ironmatrix
264         set-precipitation-parameter ironmatrix t g 20e-6  $ grain
                diameter
265         set-precipitation-parameter ironmatrix s d s y 6.4e-2*exp
                (119000/(R*T)) $ pipe diffusion on dislocations (
                Kozeschnik2012 p322)
266         set-precipitation-parameter ironmatrix s g s y 7.9e-1*exp
                (141000/(R*T)) $ diffusion on grainboundaries (
                Kozeschnik2012 p322)
267
268         $ Create precipitate phases
269         create-new-phase gamma_prime p
270         set-precipitation-parameter gamma_prime_p0 c npc       $
                particle classes
271         set-precipitation-parameter gamma_prime_p0 d ironmatrix     $
                domain
272         set-precipitation-parameter gamma_prime_p0 n s b       $
                nucleation site=bulk
273         set-precipitation-parameter gamma_prime_p0 n c o       $ nucleus
                 comp: ortho equilibrium
274         set-precipitation-parameter gamma_prime_p0 i y        $ auto
                interfacial energy
275         set-precipitation-parameter gamma_prime_P0 n u 100      $
                nucleation constant
276         set-precipitation-parameter gamma_prime_P0 T P N      $ use the
                same value as the matrix: No
277         set-precipitation-parameter gamma_prime_P0 z y       $
                interfacial energy size correction
278
279         create-new-phase gamma_dp p
280         set-precipitation-parameter gamma_dp_p0 c npc      $ particle
                classes
281         set-precipitation-parameter gamma_dp_p0 d ironmatrix    $ domain
282         set-precipitation-parameter gamma_dp_p0 n s b      $ nucleation
                site=bulk
283         set-precipitation-parameter gamma_dp_p0 i y      $ auto
                interfacial energy
284         set-precipitation-parameter gamma_dp_P0 n u 100      $
                nucleation constant
285         set-precipitation-parameter gamma_dp_p0 H Y 1.1755*(10^9*
                D_MEAN$gamma_dp_p0)^(-0.472) #shape factor
286         set-precipitation-parameter gamma_dp_P0 T P N       $ use the
                same value as the matrix: No
287         set-precipitation-parameter gamma_dp_P0 z y       $ interfacial
                 energy size correction
288
289         create-new-phase eta p
290         set-precipitation-parameter eta_p0 c npc        $ particle
                classes
291         set-precipitation-parameter eta_p0 d ironmatrix       $ domain
292         set-precipitation-parameter eta_p0 n s g        $ nucleation
                site=grain boundary
```

```
293 |             set-precipitation-parameter eta_p0 n c o        $ nucleus comp:
    |                 ortho equilibrium
294 |             set-precipitation-parameter eta_p0 i y          $ auto
    |                 interfacial energy
295 |
296 |             create-new-phase delta p
297 |             set-precipitation-parameter delta_p0 c npc         $ particle
    |                 classes
298 |             set-precipitation-parameter delta_p0 d ironmatrix        $
    |                 domain
299 |             set-precipitation-parameter delta_p0 n s g         $ nucleation
    |                 site=grain boundary
300 |             set-precipitation-parameter delta_p0 n c o         $ nucleus
    |                 comp: ortho equilibrium
301 |             set-precipitation-parameter delta_p0 i y        $ auto
    |                 interfacial energy
302 |
303 |             create-new-phase M23C6 p
304 |             set-precipitation-parameter M23C6_p0 c npc        $ particle
    |                 classes
305 |             set-precipitation-parameter M23C6_p0 d ironmatrix      $ domain
306 |             set-precipitation-parameter M23C6_p0 n s g        $ nucleation
    |                 site=grain boundary
307 |             set-precipitation-parameter M23C6_p0 n c o        $ nucleus comp
    |                 : ortho equilibrium
308 |             set-precipitation-parameter M23C6_p0 i y       $ auto
    |                 interfacial energy
309 |
310 |             $ ***********************************************
311 |             $ Heat treatment
312 |             $ ***********************************************
313 |             create-heat-treatment ageing
314 |             $1st ht segment (solutionising - heating)
315 |             append-ht-segment ageing      $ append segmment
316 |             edit-ht-segment ageing . d n ironmatrix $ define precipitation
    |                 domain
317 |             edit-ht-segment ageing . s 20     $ from 20oC
318 |             edit-ht-segment ageing . 1 1200 1   $ to 1200oC
319 |
320 |             $2nd ht segment (solutionising - holding)
321 |             append-ht-segment ageing      $ append segmment
322 |             edit-ht-segment ageing . d y     $ define inherit precipitation
    |                 domain
323 |             edit-ht-segment ageing . 2 0 24*3600 $ 24 hours
324 |
325 |             $3rd ht segment (solutionising - cooling)
326 |             append-ht-segment ageing      $ append segmment no.3
327 |             edit-ht-segment ageing . d y     $ define inherit precipitation
    |                 domain
328 |             edit-ht-segment ageing . 1 20 1000  $ assuming water cooling
329 |
330 |             $4th ht segment (ageing - heating)
331 |             append-ht-segment ageing      $ append segmment
332 |             edit-ht-segment ageing . d y     $ define inherit precipitation
    |                 domain
333 |             edit-ht-segment ageing . 1 720 1   $ 720oC ageing
334 |
335 |             $5th ht segment (ageing - holding)
336 |             append-ht-segment ageing      $ append segmment
```

```
edit-ht-segment ageing . d y     $ define inherit precipitation
    domain
edit-ht-segment ageing . 2 0 16*3600   $ 16 hours

$6th ht segment (ageing - cooling)
append-ht-segment ageing      $ append segmnent
edit-ht-segment ageing . d y     $ define inherit precipitation
    domain
edit-ht-segment ageing . 1 20 1000  $ assuming water cooling

$7th ht segment (ageing as service - heating)
append-ht-segment ageing      $ append segmnent
edit-ht-segment ageing . d y     $ define inherit precipitation
    domain
edit-ht-segment ageing . 1 750 1    $ 750oC

$8th ht segment (ageing as service - holding)
append-ht-segment ageing      $ append segmnent
edit-ht-segment ageing . d y     $ define inherit precipitation
    domain
edit-ht-segment ageing . 2 0 400*3600  $ 400 hours

$ ************************************************
$ Define parameters for precipitation simulation
$ ************************************************

set-simulation-parameter p y    $ temperature is given in C
set-simulation-parameter t h ageing 1 $ load heat treatment
    pattern
set-simulation-parameter s r    $ starting conditions: reset
    precipitates
set-simulation-parameter u 100   $ update display every 100
    iterations
set-simulation-parameter r g 1.02  $ store results in log
    intervals

start-precipitate-simulation

$ ************************************************
$ Yield Strength calculation
$ ************************************************

$ ************************************************
$ Solid-solution strengthening
$ ************************************************
$ Solid solution strengthening coefficient
set-variable-value K_SS_Co 90
set-variable-value K_SS_Cr 102
set-variable-value K_SS_Mo 637
set-variable-value K_SS_Al 43
set-variable-value K_SS_Ti 720
set-variable-value K_SS_W 826
set-variable-value K_SS_Ni 112
set-variable-value K_SS_Nb 1106
set-variable-value K_SS_C 1984
set-variable-value q 3/2
set-function-expression Sigma_ss (K_SS_Co^q*X$FCC_A1$Co+K_SS_Cr
    ^q*X$FCC_A1$Cr+K_SS_Mo^q*X$FCC_A1$Mo+K_SS_Al^q*X$FCC_A1$Al+
    K_SS_Ti^q*X$FCC_A1$Ti+K_SS_W^q*X$FCC_A1$W+K_SS_Ni^q*
    X$FCC_A1$Ni+K_SS_Nb^q*X$FCC_A1$Nb+K_SS_C^q*X$FCC_A1$C)^(1/q)
```

```
386
387             $ ************************************************
388             $ Hall-petch strenghtening
389             $ ************************************************
390
391             set-variable-value kY 600   $Hall-Petch constant [MPa micron
                    **(1/2)]
392             set-function-expression Sigma_D 100+kY*(GD$ironmatrix*1e6)
                    ^(-0.5)
393
394             $ ************************************************
395             $ Universal constants for precipitation strengthening
396             $ ************************************************
397             set-variable-value Ttest 293        $ test temperature [K]
398             set-variable-value Taylor 2.6       $ Taylor factor
399             set-variable-value b 2.5*1e-10        $ Burgers Vector [m]
400             set-function-expression Tdis 1/2*ESM$ironmatrix*b^2 $
                    Dislocation line tension [J/m]
401
402             $ ************************************************
403             $ Precip. strength. from APB effect by gamma prime
404             $ ************************************************
405             $ APB energy Calculation (Ref. Crudden)
406             set-variable-value aapb_Cr -0.0039
407             set-variable-value bapb_Cr -0.2468
408             set-variable-value capb_Cr -2.6911
409             set-variable-value aapb_Mo 0.0441
410             set-variable-value bapb_Mo -2.5065
411             set-variable-value capb_Mo 21.837
412             set-variable-value aapb_W 0.00552
413             set-variable-value bapb_W -2.2455
414             set-variable-value capb_W 13.69
415             set-variable-value aapb_Nb 0.0254
416             set-variable-value bapb_Nb -1.0747
417             set-variable-value capb_Nb 9.7279
418             set-variable-value aapb_Ti -0.0028
419             set-variable-value bapb_Ti 0.1695
420             set-variable-value capb_Ti 7.2324
421
422             set-function-expression APB_Cr aapb_Cr*(100*X$gamma_prime_P0$Cr)
                    ^3+bapb_Cr*(100*X$gamma_prime_P0$Cr)^2+capb_Cr*(100*
                    X$gamma_prime_P0$Cr)
423             set-function-expression APB_Mo aapb_Mo*(100*X$gamma_prime_P0$Mo)
                    ^3+bapb_Mo*(100*X$gamma_prime_P0$Mo)^2+capb_Mo*(100*
                    X$gamma_prime_P0$Mo)
424             set-function-expression APB_W aapb_W*(100*X$gamma_prime_P0$W)^3+
                    bapb_W*(100*X$gamma_prime_P0$W)^2+capb_W*(100*
                    X$gamma_prime_P0$W)
425             set-function-expression APB_Nb aapb_Nb*(100*X$gamma_prime_P0$Nb)
                    ^3+bapb_Nb*(100*X$gamma_prime_P0$Nb)^2+capb_Nb*(100*
                    X$gamma_prime_P0$Nb)
426             set-function-expression APB_Ti aapb_Ti*(100*X$gamma_prime_P0$Ti)
                    ^3+bapb_Ti*(100*X$gamma_prime_P0$Ti)^2+capb_Ti*(100*
                    X$gamma_prime_P0$Ti)
427             set-function-expression apb 0.240+0.001*(APB_Cr+APB_Mo+APB_W+
                    APB_Nb+APB_Ti)    $ anti phase boundary energy [J/m^2]
428
429             set-function-expression F 2*apb*R_MEAN$gamma_prime_P0         $
                    gamma' repulsion [J/m]
```

```
set-function-expression L (2*3.14/3/f$gamma_prime_p0)^(1/2)*
    R_MEAN$gamma_prime_P0   $ mean particle spacing on a slip
    plane [m]
set-function-expression rm ESM$ironmatrix*b^2/apb/2  $ Critical
    dislocation spacing [m]

if (R_MEAN$gamma_prime_P0-rm>=0)
       set-function-expression l1 2*(R_MEAN$gamma_prime_P0^2-(
           R_MEAN$gamma_prime_P0-rm)^2)^0.5  $ Strongly coupled
else
       set-function-expression l1 2*(R_MEAN$gamma_prime_P0)
           $Weakly coupled
endif

if ((Tdis/R_MEAN$gamma_prime_P0/apb)^(1/2)*L-(L-l1)>=0)
       set-function-expression lamb (Tdis/R_MEAN$gamma_prime_P0/
           apb)^(1/2)*L
else
       set-function-expression lamb L-l1
endif

set-function-expression Sigma_apb_prime Taylor*apb/b/2*l1/(lamb+
    R_MEAN$gamma_prime_P0)*1e-6

$ ************************************************************
$ Precip. strength. from coherent effect by gamma double prime
$ ************************************************************
set-function-expression Sigma_co_dp Taylor*1.7*ESM$ironmatrix
    *(0.0286*2/3)^1.5*((HEQ_MEAN$gamma_dp_p0/2)^2*f$gamma_dp_p0
    *0.7/2/b/(DEQ_MEAN$gamma_dp_p0/2))^0.5*1e-6

$ ************************************************
$ Precipitation strengthening from Orowan mechanism
$ ************************************************
set-function-expression Sigma_or_prime Taylor*3*ESM$ironmatrix*
    b/2/((2*3.14/3/f$gamma_prime_P0)^0.5*R_MEAN$gamma_prime_p0)
    *1e-6
set-function-expression Sigma_or_dp Taylor*3*ESM$ironmatrix*b
    /2/((2*3.14/3/f$gamma_dp_P0)^0.5*r_mean$gamma_dp_p0)*1e-6
set-function-expression Sigma_or_eta Taylor*3*ESM$ironmatrix*b
    /2/((2*3.14/3/f$etaP0)^0.5*r_mean$eta_p0)*1e-6
set-function-expression Sigma_or_delta Taylor*3*ESM$ironmatrix*
    b/2/((2*3.14/3/f$delta_P0)^0.5*r_mean$delta_p0)*1e-6
set-function-expression Sigma_or_M23C6 Taylor*3*ESM$ironmatrix*
    b/2/((2*3.14/3/f$M23C6_P0)^0.5*r_mean$M23C6_p0)*1e-6

$ ************************************************
$ Output the result
$ ************************************************
set-working-directory /Users/***/
export-open-file calc_result_fe.csv
export-clear-file
export-file-variables "%s, %s, %s, %s, %s, %s, %s, %s, %s, %s,
    %s, %s, %s, %s, %s, %s, %s, %s" time Temp f_gamma_prime
    R_gamma_prime apb_gamma_prime f_gamma_dp l_gamma_dp
    f_M23C6_P0 R_M23C6_P0 Sigma_SS Sigma_GS Sigma_apb_prime
    Sigma_or_prime Sigma_co_dp Sigma_or_d Sigma_eta Sigma_delta
    Sigma_or_M23C6
```

```
export-file-variables "%s, %s, %s, %s, %s, %s, %s, %s, %s, %s,
    %s, %s, %s, %s, %s, %s, %s, %s" h oC % nm J/m2 % nm % nm MPa
     MPa MPa MPa MPa MPa MPa MPa MPa
export-file-variables "%5.2f, %f, %5.2f, %5.2f, %5.2f, %5.2f,
    %5.2f, %5.2f, %5.2f, %5.2f, %5.2f, %5.2f, %5.2f, %5.2f, %5.2
    f, %5.2f, %5.2f, %5.2f" stepvalue/3600 t$c f$gamma_prime_P0
    *100 R_MEAN$gamma_prime_P0*10^9 apb f$gamma_dp_P0*100
    DEQ_MEAN$gamma_dp_p0*10^9 f$M23C6_P0*100 R_MEAN$M23C6_p0
    *10^9 Sigma_ss*F$FCC_A1 Sigma_D Sigma_apb_prime
    Sigma_or_prime Sigma_co_dp Sigma_or_dp Sigma_or_eta
    Sigma_or_delta Sigma_or_M23C6
export-close-file
""".format(*stringslist))

# ************************************************
# Execute the script in MatCalc
# ************************************************

# Save the original directory location
orig_dir = getcwd()
chdir(MatCalc_dir)

# Open MatCalc app and execute the script above
devnull_object = open(devnull, "w")
run_files3 = Popen("./mcc␣"+script_pointer, stdin=PIPE, stdout=
    devnull_object, shell=True)
# Exit MatCalc
run_files3.communicate(input='exit')

chdir(orig_dir) # Go back to the original directory

g = open('calc_result_fe.csv', 'r')
list=[]
reader = csv.reader(g)
for row in reader:
       list.append(row)
result = list[-1][2:]
g.close()

for n in range(1,9):
       if "nan" in result[-n] or "inf" in result[-n]:
              result[-n]="0"
       else:
              None
Sigma_apb_prime = float(result[-7])
Sigma_or_prime = float(result[-6])
Sigma_co_dp = float(result[-5])
Sigma_or_dp = float(result[-4])
Sigma_eta = float(result[-3])
Sigma_delta = float(result[-2])
Sigma_M23C6 = float(result[-1])

# Precipitation strengthening (cutting vs bypassing)
if Sigma_apb_prime >= Sigma_or_prime:
       Sigma_p_prime = Sigma_or_prime
else:
       Sigma_p_prime = Sigma_apb_prime

if Sigma_co_dp >= Sigma_or_dp:
       Sigma_p_dp = Sigma_or_dp
else:
```

```
519                     Sigma_p_dp = Sigma_co_dp
520
521             Sigma_p = (Sigma_p_prime**2.0+Sigma_p_dp**2.0+Sigma_eta**2.0+
                    Sigma_delta**2.0+Sigma_M23C6**2.0)**(1/2.0)
522             Sigma_ss = float(result[-9])
523             Sigma_gs = float(result[-8])
524             strength = int(Sigma_ss + Sigma_gs + Sigma_p)
525
526             raw_data = []
527             for item in result[0:9]:
528                     raw_data.append(float(item))
529             raw_data.extend([int(Sigma_ss), int(Sigma_gs), int(
                    Sigma_apb_prime), int(Sigma_or_prime), int(Sigma_p_prime),
                    int(Sigma_co_dp), int(Sigma_or_dp), int(Sigma_p_dp), int(
                    Sigma_eta), int(Sigma_delta), int(Sigma_M23C6), int(Sigma_p),
                     int(strength)])
530             print """f_g' R_g' apb_g' f_g" r_g" f_m23c6 r_m23c6 S_SS S_GS
                    S_apb_g' S_or_g' S_p_g' S_co_g" S_or_g" S_p_g" Sigma_eta
                    Sigma_delta Sigma_M23C6 S_p YS: """
531             print str(raw_data)
532             f = open('calc_result_fe.txt', 'a')
533             f.write("""f_g' R_g' apb_g' f_g" r_g" f_m23c6 r_m23c6 S_SS S_GS
                    S_apb_g' S_or_g' S_p_g' S_co_g" S_or_g" S_p_g" Sigma_eta
                    Sigma_delta Sigma_M23C6 S_p YS: """ + '\n')
534             f.write(str(raw_data) + '\n')
535             f.close()
536     return strength
537
538 def genetic(stren, popsize=100, mutprob=0.2, elite=0.1, maxiter=1000):
539     #The number of elites passed down to the next generation
540     topelite=int(elite*popsize)
541
542     #Mutation (3 elements changes)
543     def mutate(vec):
544             i=random.randint(0,len(domain)-1)
545             j=random.randint(0,domain[i][1])
546             m1 = vec[0:i]+[j]+vec[i+1:]
547             #return vec[0:i]+[j]+vec[i+1:]
548             k=random.randint(0,len(domain)-1)
549             l=random.randint(0,domain[k][1])
550             m2 = m1[0:k]+[l]+m1[k+1:]
551             m=random.randint(0,len(domain)-1)
552             n=random.randint(0,domain[m][1])
553             return m2[0:m]+[n]+m2[m+1:]
554
555     #Crossover
556     def crossover(r1,r2):
557             if random.random<0.5:
558                     i=random.randint(1,len(domain)-2)
559                     return r1[0:i]+r2[i:]
560             else:
561                     i=random.randint(1,len(domain)-2)
562                     return r2[0:i]+r1[i:]
563
564     #Initial population
565     domain=[(0,30)]*9
566     pop = []
567
568     for i in range(popsize):
569             vec=[random.randint(domain[i][0],domain[i][1]) for i in range(len
                    (domain))]
```

```
570             pop.append(vec)
571     passed_elite = pop[0:topelite]
572 
573     print "************************************************"
574     print "Initial␣population␣(created␣randomly)"
575     print pop
576     print "************************************************"
577     print ""
578     print ""
579 
580     f = open('calc_result_fe.txt', 'w')
581     f.write("************************************************" + '\n')
582     f.write("Initial␣population␣(created␣randomly)" + '\n')
583     f.write(str(pop) + '\n')
584     f.write("************************************************" + '\n')
585     f.write('\n')
586     f.write('\n')
587     f.close()
588 
589     f = open('elite_fe.txt', 'w')
590     f.write("popsize=100,␣mutprob=0.2,␣elite=0.1,␣maxiter=1000")
591     f.close()
592 
593     #main loop
594     for i in range(maxiter):
595             if i == 0:
596                     scores = [(stren(v),v) for v in pop]
597             else:
598                     scores = passed_elite
599                     scores.extend([(stren(v),v) for v in pop[topelite:]])
600             #sort strength from high to low
601             scores.sort(reverse=True)
602 
603             print ""
604             print "************************************************"
605             print "Results␣of␣the␣generation␣" + str(i)
606             print "------------------------------------------------------
                    "
607             print "scores:␣" + str(scores)
608             print "------------------------------------------------------
                    "
609             f = open('calc_result_fe.txt', 'a')
610             f.write('\n')
611             f.write("************************************************"+'\n')
612             f.write("RESULTS␣OF␣GENERATION␣"+ str(i) + '\n')
613             f.write("------------------------------------------------"+'\
                    n')
614             f.write("scores:" + str(scores) + '\n')
615             f.write("------------------------------------------------"+'\
                    n')
616             f.write("************************************************"+'\n')
617             f.close()
618 
619             ranked = [v for (s,v) in scores]
620             #i = 0
621             j = 1
622             passed_elite = [scores[0]]
623             for scores[j] in scores:
624                     if scores[j] not in passed_elite:
625                             passed_elite.append(scores[j])
626             passed_elite = passed_elite[0:topelite]
```

```
627             print "passed_elite"
628             print passed_elite
629
630             #keep topelites
631             pop = [v for (s,v) in passed_elite]
632             print "**********************************************"
633             print ""
634             print ""
635             f = open('elite_fe.txt', 'a')
636             f.write("pop(topelites) for generation" + str(i) + ": " + str(
                    scores[0]) + '\n')
637             f.close()
638
639             #add mutated and bred
640             while len(pop) < popsize*mutprob:
641                    ran = random.random()
642                    print "mutation"
643                    if 0.0 <= ran and ran < 5.0/15.0:
644                           c=random.randint(0, popsize*0.2-1)
645                           pop.append(mutate(ranked[c]))
646                    elif 5.0/15.0 <= ran and ran < 9.0/15.0:
647                           c=random.randint(popsize*0.2,popsize*0.4-1)
648                           pop.append(mutate(ranked[c]))
649                    elif 9.0/15.0 <= ran and ran < 12.0/15.0:
650                           c=random.randint(popsize*0.4,popsize*0.6-1)
651                           pop.append(mutate(ranked[c]))
652                    elif 12.0/15.0 <= ran and ran < 14.0/15.0:
653                           c=random.randint(popsize*0.6,popsize*0.8-1)
654                           pop.append(mutate(ranked[c]))
655                    else:
656                           c=random.randint(popsize*0.8,popsize-1)
657                           pop.append(mutate(ranked[c]))
658
659             while len(pop)<popsize:
660                    ran2 = random.random()
661                    ran3 = random.random()
662                    if 0.0 <= ran2 and ran2 < 5.0/15.0:
663                           if 0.0 <= ran3 and ran3 < 5.0/15.0:
664                                  c1=random.randint(0, popsize*0.2-1)
665                                  c2=random.randint(0, popsize*0.2-1)
666                           elif 5.0/15.0 <= ran3 and ran3 < 9.0/15.0:
667                                  c1=random.randint(0, popsize*0.2-1)
668                                  c2=random.randint(popsize*0.2,popsize*0.4-1)
669                           elif 9.0/15.0 <= ran3 and ran3 < 12.0/15.0:
670                                  c1=random.randint(0, popsize*0.2-1)
671                                  c2=random.randint(popsize*0.4,popsize*0.6-1)
672                           elif 12.0/15.0 <= ran3 and ran3 < 14.0/15.0:
673                                  c1=random.randint(0, popsize*0.2-1)
674                                  c2=random.randint(popsize*0.6,popsize*0.8-1)
675                           else:
676                                  c1=random.randint(0, popsize*0.2-1)
677                                  c2=random.randint(popsize*0.8,popsize-1)
678                    elif 5.0/15.0 <= ran2 and ran2 < 9.0/15.0:
679                           if 0.0 <= ran3 and ran3 < 5.0/15.0:
680                                  c1=random.randint(popsize*0.2,popsize*0.4-1)
681                                  c2=random.randint(0, popsize*0.2-1)
682                           elif 5.0/15.0 <= ran3 and ran3 < 9.0/15.0:
683                                  c1=random.randint(popsize*0.2,popsize*0.4-1)
684                                  c2=random.randint(popsize*0.2,popsize*0.4-1)
685                           elif 9.0/15.0 <= ran3 and ran3 < 12.0/15.0:
686                                  c1=random.randint(popsize*0.2,popsize*0.4-1)
```

```
687                                     c2=random.randint(popsize*0.4,popsize*0.6-1)
688                             elif 12.0/15.0 <= ran3 and ran3 < 14.0/15.0:
689                                     c1=random.randint(popsize*0.2,popsize*0.4-1)
690                                     c2=random.randint(popsize*0.6,popsize*0.8-1)
691                             else:
692                                     c1=random.randint(popsize*0.2,popsize*0.4-1)
693                                     c2=random.randint(popsize*0.8,popsize-1)
694                     elif 9.0/15.0 <= ran2 and ran2 < 12.0/15.0:
695                             if 0.0 <= ran3 and ran3 < 5.0/15.0:
696                                     c1=random.randint(popsize*0.4,popsize*0.6-1)
697                                     c2=random.randint(0, popsize*0.2-1)
698                             elif 5.0/15.0 <= ran3 and ran3 < 9.0/15.0:
699                                     c1=random.randint(popsize*0.4,popsize*0.6-1)
700                                     c2=random.randint(popsize*0.2,popsize*0.4-1)
701                             elif 9.0/15.0 <= ran3 and ran3 < 12.0/15.0:
702                                     c1=random.randint(popsize*0.4,popsize*0.6-1)
703                                     c2=random.randint(popsize*0.4,popsize*0.6-1)
704                             elif 12.0/15.0 <= ran3 and ran3 < 14.0/15.0:
705                                     c1=random.randint(popsize*0.4,popsize*0.6-1)
706                                     c2=random.randint(popsize*0.6,popsize*0.8-1)
707                             else:
708                                     c1=random.randint(popsize*0.4,popsize*0.6-1)
709                                     c2=random.randint(popsize*0.8,popsize-1)
710                     elif 12.0/15.0 <= ran2 and ran2 < 14.0/15.0:
711                             if 0.0 <= ran3 and ran3 < 5.0/15.0:
712                                     c1=random.randint(popsize*0.6,popsize*0.8-1)
713                                     c2=random.randint(0, popsize*0.2-1)
714                             elif 5.0/15.0 <= ran3 and ran3 < 9.0/15.0:
715                                     c1=random.randint(popsize*0.6,popsize*0.8-1)
716                                     c2=random.randint(popsize*0.2,popsize*0.4-1)
717                             elif 9.0/15.0 <= ran3 and ran3 < 12.0/15.0:
718                                     c1=random.randint(popsize*0.6,popsize*0.8-1)
719                                     c2=random.randint(popsize*0.4,popsize*0.6-1)
720                             elif 12.0/15.0 <= ran3 and ran3 < 14.0/15.0:
721                                     c1=random.randint(popsize*0.6,popsize*0.8-1)
722                                     c2=random.randint(popsize*0.6,popsize*0.8-1)
723                             else:
724                                     c1=random.randint(popsize*0.6,popsize*0.8-1)
725                                     c2=random.randint(popsize*0.8,popsize-1)
726                     else:
727                             if 0.0 <= ran3 and ran3 < 5.0/15.0:
728                                     c1=random.randint(popsize*0.8,popsize-1)
729                                     c2=random.randint(0, popsize*0.2-1)
730                             elif 5.0/15.0 <= ran3 and ran3 < 9.0/15.0:
731                                     c1=random.randint(popsize*0.8,popsize-1)
732                                     c2=random.randint(popsize*0.2,popsize*0.4-1)
733                             elif 9.0/15.0 <= ran3 and ran3 < 12.0/15.0:
734                                     c1=random.randint(popsize*0.8,popsize-1)
735                                     c2=random.randint(popsize*0.4,popsize*0.6-1)
736                             elif 12.0/15.0 <= ran3 and ran3 < 14.0/15.0:
737                                     c1=random.randint(popsize*0.8,popsize-1)
738                                     c2=random.randint(popsize*0.6,popsize*0.8-1)
739                             else:
740                                     c1=random.randint(popsize*0.8,popsize-1)
741                                     c2=random.randint(popsize*0.8,popsize-1)
742                     pop.append(crossover(ranked[c1],ranked[c2]))
743                     print "crossover"
744
745     return scores[0][1]
```